Heavy-light four-quark states in the charmonium region in a Bethe-Salpeter and Dyson-Schwinger approach

Dissertation

Paul C. Wallbott[*]

December 30, 2019

Supervised by Prof. Dr. Christian S. Fischer

[*]Institut für Theoretische Physik, Justus-Liebig-Universität Gießen, 35392 Gießen, Germany

Introduction

Meson spectrum and the Quark model   While the word "meson" often refers to quark-antiquark states, one can define the meson spectrum in a more general manner as all colorless QCD bound states with baryon number zero, which implies integer spin. The meson spectrum contains states built from one or multiple quark-antiquark pairs, as well as hybrids and glueballs. The former consist out of a quark-antiquark pair and a gluon, whereas the latter are bound states of gluons.

Many observed states in the meson spectrum can be identified with $q\bar{q}$ states calculated from the Quark model (QM), see [1] and references therein. It explains some important features of the spectrum, for example:

- The **nonet structure of the light meson multiplets** arises, because of the $SU(3)$ flavor symmetry for the light u, d and s quarks. Since the s quark has a higher constituent mass than u and d quark, the strange multiplet members have a higher mass. The $SU(3)$ flavor symmetry also introduces the isospin and hypercharge quantum numbers, which can explain many decay properties of the meson states.

- The **charmonium-and bottomonium spectrum** can be described accurately by the (relativistic) QM as we will see in section 1.1.

- The **appearance of distinct quantum numbers**, such as $J^{PC} = (0^{-+}, 1^{--})$ for s waves and $J^{PC} = (0^{++}, 1^{+\pm}, 2^{++})$ for p waves , whereas $J^{PC} = (0^{+-}, 1^{-+}, 2^{+-}, 3^{-+})$ for instance cannot be accessed by QM $q\bar{q}$ states. We will call them "QM exotic" quantum numbers, since they are in principle possible for $q\bar{q}$ structures in other approaches, such as the Dyson-Schwinger and Bethe-Salpeter approach. An example is the $\pi_1(1400)$ with $J^{PC} = 1^{-+}$; a candidate for a hybrid.

Other types of **exotic states** were found, that call for an extension of the QM $q\bar{q}$ picture: Type I exotic states could be $q\bar{q}$ QM states from their quantum numbers, but have different properties, such as their mass, width, or decays. Type II exotic states cannot be $q\bar{q}$ states, even outside the QM (where the "Quark model exotic" quantum numbers would be possible). Some of these states are likely to be of **four-quark nature**:

Exotics I: the light scalar nonet   One example are the light scalar nonet states, which are exotics of type I. As $q\bar{q}$ states, they should be p waves and therefore the QM predicts masses around 1-1.5 GeV. A multiplet exists in this mass range that could be assigned to the QM states, but what is then the light scalar multiplet? As $qq\bar{q}\bar{q}$ states, the nonet structure and many properties of the states can be explained. But even if the four-quark structure is assumed, it is an open question how the light quarks cluster inside the four-quark state and what binding mechanism occurs.

An old idea is the binding of a colored diquark and a colored antidiquark [2]. The word "tetraquark" is often reserved for this type of state in the literature, but we will use it synonymous to "four-quark state" throughout this thesis.

Calculations from Dyson-Schwinger equations (DSEs) and Bethe-Salpeter equations (BSEs) for the light scalar tetraquarks paint a different picture [3]. They also find a light nonet, but a different binding mechanism. By construction, the four quarks are bound by gluon exchange alone. The interaction leads to intermediate meson-meson and diquark-antidiquark components. The former however are solely responsible for the light mass of the resulting tetraquark states. We will come back to the light scalar states in chapter 2.

Exotics II: spectrum in the charmonium energy region Other highly interesting examples are exotic states in the **charmonium energy region** and chapter 1 will be dedicated to this topic. The first discovery of an exotic state in the charmonium energy region is that of the $X(3872)$ in 2003. It is neutral, has quantum numbers $I(J^{PC}) = 0(1^{++})$ and could therefore be a $c\bar{c}$ state. However, its decay properties are unexpected for a $c\bar{c}$ structure and one is tempted to identify it with a four-quark state with hidden charm (quark content $cq\bar{q}\bar{c}$). Other examples in the charmonium energy region are the Z **states**. Because of their charges, they are exotic states of type II and consequently their existence is a smoking gun argument for non-$c\bar{c}$ structures in the charmonium energy region. They are also prime candidates for tetraquarks. Many more exotics are discovered and will be discussed in section 1.1.

The structure of four-quark states, in particular the binding mechanisms and dominant sub-clusters for $cq\bar{q}\bar{c}$ tetraquarks are subject to current research. Three possible sub-clusters can emerge:

- $(c\bar{c})(q\bar{q})$: charmonium couples to a light meson, we will call this "hadro-charmonium" (HC).

- $(c\bar{q})(q\bar{c})$: a heavy-light meson couples to a heavy-light antimeson. We will call this "heavy-light meson meson" (HLM).

- $(cc)(\bar{q}\bar{q})$: a heavy diquark couples to a light antidiquark. We will call this "diquark-antidiquark" (DI).

As the word "tetraquark" is often reserved for a bound state of colored diquark and antidiquark, the word "molecule" is often reserved for a bound heavy-light meson and heavy-light antimeson pair with a small binding energy, see [4] for a rigorous definition in the effective field theory context. It is not to be confused with our HLM components of the four-quark amplitude.

Four-quark states are discussed in many different theoretical approaches that often assume a particular sub-cluster and binding mechanism is dominant, which leads to very different predictions for the spectrum of four-quark states. Therefore, it is important to answer the following questions, which are the **main motivation of this thesis**: Which of the many discovered exotics are four-quark states? If there is a dominant sub-cluster in the formation of four-quark states, which one is it? Are the observed states a mixture of different sub-clusters?

Chapter one: tetraquarks in the charmonium energy region We try to answer these questions for the hidden-charm tetraquarks in chapter 1. The theoretical tool we use is the DSE-BSE framework in the rainbow-ladder (RL) truncation. It is fully relativistic, non-perturbative and respects important QCD symmetries. It has been successful in describing various hadronic observables.

In the following we will solve a genuine four-body BSE where quarks and antiquarks interact via gluon exchange, as done in [3]. Although the binding mechanism is due to gluon exchange, we would like to identify sub-clusters in the tetraquark amplitude. We achieve this by expanding it in terms of the relevant physical components: HC, HLM, DI and call the amplitude expanded in that way the "physical" amplitude. While all components are potentially present in our approach, the four-body BSE will dynamically decide which components are dominant. That allows us not only to determine masses for a variety of states, but also to make a statement about the four-quark substructure of every state individually.

This method will be applied to ground states for scalar and axialvector $cu\bar{u}\bar{c}$ tetraquarks. We directly compare to experiment and make predictions for new states. Our framework can consistently describe open-charm tetraquarks as well, and we will calculate $cc\bar{q}\bar{q}$ and $cc\bar{s}\bar{s}$ states in the scalar-and axialvector channel. Parts of this work are already published, see [5] and [6].

For the curious reader it is possible to skip the technical parts of chapter 1 and focus only on sections 1.1, 1.5 and subsection 1.4.5.

Resonances in the DSE-BSE framework In the DSE-BSE framework, physical states show up as poles in the scattering matrix in the total momentum squared variable. While bound states appear on the real axes, resonances appear in the complex plane in higher Riemann sheets. Most physical states are resonances. A description and correct treatment of resonances in the BSE-DSE framework fulfills the following criteria: A decay channel needs to be present; a proper path deformation to respect the singularity structure of the system has to be applied and analytic continuation or direct calculation in the second Riemann sheet needs to be performed, as recently done in [7, 8].

The tetraquark four-body equation exhibits a decay channel. However, we have not applied a path deformation and analytic continuation due to the complexity of the four-body equation so far. In chapter 2 we investigate a DSE-BSE system where the steps above can be applied.

Chapter two: $q\bar{q}$ resonances and the light scalar states Chapter 2 is about the light scalar mesons and the technical tools for solving resonant BSE-DSE problems. We describe the scalar $q\bar{q}$ states with a two-body BSE in a truncation scheme beyond the simpler RL truncation that is used in chapter 1. A two-pion decay channel is thereby introduced into the two-body BSE's scattering kernel. We apply a path deformation and analytic continuation to find the pole position in the second Riemann sheet. The ρ meson will serve us as an example to investigate the method, before we turn to the scalar $q\bar{q}$ state.

Although this chapter is focused on the development of the method to de-

scribe resonances in the BSE-DSE framework, the technical section 2.2 can be left out if the reader is only interested in the physics parts.

Contents

Contents

8

1. Heavy-light tetraquarks

1.1. Physics overview

1.1.1. Experimental status

The experimental spectrum in the charmonium energy region is shown in figure 1.1. States with black solid lines are those that can be described very well as $c\bar{c}$ states by simple quark potential models with a Cornell like potential [9,10], which includes a Coulomb and a linear rising term. More advanced models including spin-spin interactions and relativistic corrections can reproduce the charmonium states (without exotics) quite accurately, see [11]. Another way to obtain these potentials is extraction via lattice QCD. The general form of Coulomb therm plus linear rising plus spin-spin interactions can be used to fit these potentials, see [12,13]. Also, direct lattice calculations for the spectrum have been done [14,15].

Despite the great success of describing the pure charmonium states, there is definitely more than charmonium in the spectrum shown in figure 1.1. Dashed lines with 3 dashes stand for exotics with $I = 0$, dashed lines with four dashes for exotics with $I = 1$, that are listed in the PDG. We will call these states exotics within this context and we listed the most promising ones in table 1.1.

From 2003 onwards, new states in the charmonium region were found, that had not been predicted by Quark models. There are a number of reasons why some may not be $q\bar{q}$ states: A lot of them are relatively narrow although they lie above open-charm decay thresholds. All of these states decay into charmonium and some light meson, some were found to decay into open-charm mesons as well, see table 1.1.

There are many exotic candidates found in the vector channel. This channel is naturally accessed in e^+e^- collisions, however, this "overpopulation" of states can also not be explained in a charmonium picture. Possible explanations will be discussed in subsection 1.1.2. While the "Y" states found so far are neutral states, a smoking gun for non-charmonium states is the appearance of the charged Z states, which is not possible for a $c\bar{c}$ object, because it is always neutral.

In this thesis we calculated the 0^{++} and $1^{+\pm}$ ground states, including two charm quarks. In contrast to the vector states, these states cannot be produced directly from e^+e^- collisions, which makes the experimental determination of their properties a bit trickier. Among those collected in table 1.1 we therefore focus on the $X(3872), X(3915), Z(3900)$ and the $X(4140)$, which contains strangeness in its decay to $J/\Psi\phi$. Therefore, it could be a separate ground state that we have access to in our framework. Let us take a closer look at them:

The $X(3872)$ is the first exotic state that was found in the charmonium region in 2003 by Belle in the $B^{\pm} \rightarrow K^{\pm}\pi^+\pi^- J/\Psi$ decay as a peak in the $J/\psi\pi^+\pi^-$ invariant mass spectrum [16] and later other experiments confirmed the state [17–20]. The quantum numbers were determined as $J^{PC} = 1^{++}$, which was later confirmed by LHCb [21]. The state has isospin zero but its
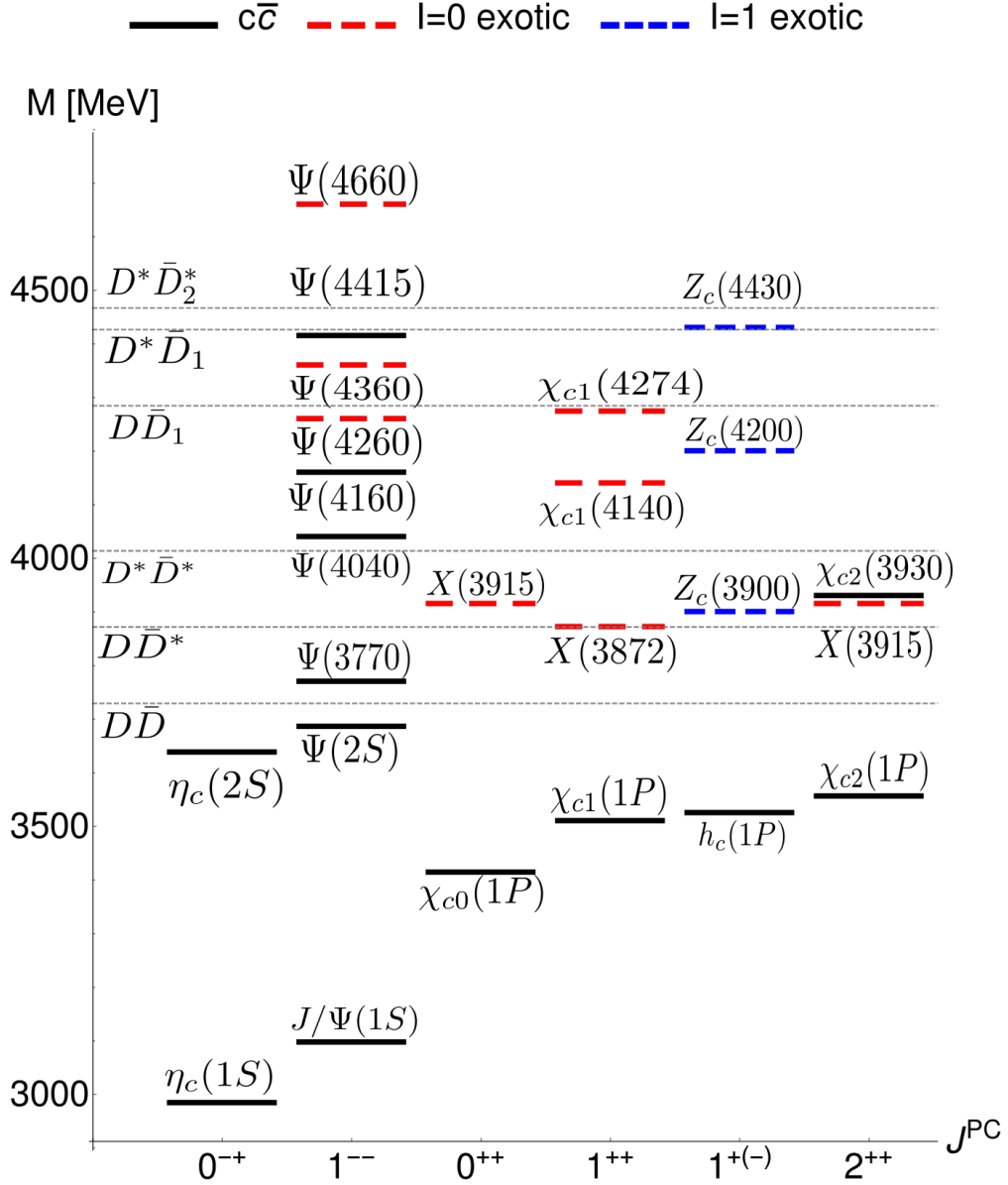
Figure 1.1.: Experimental spectrum in the charmonium energy region with Quark-model-like $c\bar{c}$ states (black solid lines), together with exotic states with $I = 0$ (red lines with 3 dashes) and $I = 1$ (blue lines with 4 dashes).

	$I(J^{PC})$	width [MeV]	seen hadronic decays (%)
$X(3872)$	$0(1^{++})$	<1.2	$\omega J/\Psi$ (> 2.3) $D^0 \bar{D}^{*0}$ (> 30) $D^0 \bar{D}^0 \pi^0$ (> 40) $\pi^+ \pi^- J/\Psi$ (> 3.2)
$X(4140)$	$0(1^{++})$	22	$\phi J/\Psi$
$X(3915)$	$0(0^{++}/2^{++})$	20	$\omega J/\Psi$
$Z_c(3900)$	$1(1^{+-})$	28.2	$\pi J/\Psi$ $D\bar{D}^*$
$Z_c(4430)$	$1(1^{+-})$	181	$\pi^+ J/\Psi$ $\pi^+ \Psi(2S)$
$Y(4260)$	$0^-(1^{--})$	55	$J/\Psi \pi\pi$ $J/\Psi KK$
$Y(4360)$	$0^-(1^{--})$	96	$\Psi(2S)\pi^+\pi^-$
$Y(4660)$	$0^-(1^{--})$	72	$\Psi(2S)\pi^+\pi^-$
$X(4020)/Z(4020)$	$1^+(?^{?-})$	13	$h_c(1P)\pi^\pm$ $(D^*\bar{D}^*)^\pm$
$Z_c(4200)$	$1^+(1^{+-})$	370	$J/\Psi \pi^+$
$Y(4230)$	$0^-(1^{--})$	59	$h_c\pi^+\pi^-$ $h_c\pi^+\pi^-$ $\omega\chi_{c_0}$
$Y(4390)$	$0^-(1^{--})$	140	$h_c\pi^+\pi^-$

Table 1.1.: Collection of exotic candidates in the charmonium mass region. The states above the line are listed in the PDG, the ones below are listed but "omitted from summary table".

branching ratio in $J/\Psi\pi^+\pi^-$ with possible intermediate ρ resonances is quite large compared to the known isospin violating decays in the charmonium region, see [22] and references in there. Possible explanations could be the $u - d$ quark mass difference, electromagnetic effects due to their different charges as well as strong ω-ρ mixing. The $X(3872)$ lies close to the $D\bar{D}^*$ threshold, probably below. That would indicate a positive binding energy, which is expected for a $D\bar{D}^*$ molecule. A detailed line shape analysis will be possible at PANDA at FAIR [23].

The $X(4140)$ was first discovered in $B^- \to J/\Psi\phi K^-$ in 2009 by the CDF collaboration [24] in $p\bar{p}$ collisions. We will later identify it with the strange partner of the $X(3872)$. Towards this end an analysis in $J/\Psi\phi$ and $D_s\bar{D}_s^*$ with Belle and BaBar data will hopefully shed more light on the nature of the $X(4140)$, as well as other hidden strangeness candidates [25].

The Z **states** carry $J^P = 1^+$. The authors of [22] distinguish between states of type I (that were found in B-meson decays and have a larger width) which would be the $Z(4430)$ and $Z(4200)$. A type II state (lies closely above threshold, has a small width) is for example the $Z(3900)$. This distinguishes them from the $X(3872)$ which is very narrow and probably below threshold and therefore a perfect candidate for a molecule, as we will discuss in subsection 1.1.2.

These isotriplet states are candidates for hidden-charm tetraquarks, since they come in isospin multiplets. A molecular interpretation is unlikely, since most Z states do not appear slightly below decay thresholds. We are interested especially in the ground state, which would be the $Z(3900)$. It was found in $Y(4260)$ decays in the $J/\Psi\pi$ subsystem and firstly discovered by BESIII [26] in $e^+e^- \to \pi^+\pi^- J/\Psi$ at 4.26 GeV, which is the production threshold of the $Y(4260)$. The mass was obtained from a fit to the $\pi^\pm J/\Psi$ invariant mass spectrum. Later it was confirmed by BELLE [27] with a different technique.

No experimental candidate for **open-charm tetraquarks** has been found yet, but we can adjust our theoretical setup and predict their masses. They have quark content $cc\bar{q}\bar{q}$ and therefore, as the name suggests, carry a charm quantum number which is not 0. They can be made out of:

- two heavy-light mesons $c\bar{q}$ and $c\bar{q}$. We also call this heavy-light meson meson (HLM),

- a heavy diquark cc and a light antidiquark $\bar{q}\bar{q}$. We also call this diquark-antidiquark (DI).

They should be detectable in meson-meson decays, not in meson antimeson as the hidden-charm tetraquarks. Also, a decay into charmonia is not possible. These states come in "unusual" diquark-like isospin multiplets (because the isospin is carried by a diquark), where for example the charges are $(0,+,++)$ for the isospin triplet. We will return to this point in section 1.4 when we construct explicit tetraquark amplitudes.

1.1.2. Interpretation of exotics as four-quark states

The interpretation of exotic states as tetraquarks is an active research area, for recent reviews see [4,22,28–31]. These tetraquarks are bound states of the strong

interaction and could therefore be one (or a mixture) of the following: hybrids, glueballs, two, four or even higher quark states. Four-quark components might be dominant for the states we have discussed so far, because their decays into charmonium plus light mesons, or two open-charm mesons. This would be a direct "falling apart" of the four-quark components. Also, some states are charged and suggest a $c\bar{c}$ and a light charged $q\bar{q}$ as building blogs.

An important question remains: What is the internal structure of these four-quark states? As already mentioned, there are three possible sub-clusters: hadro-charmonium (HC), heavy-light meson meson (HLM) and diquark-antidiquark (DI). Consequently, there mainly exist three classes of different approaches, that assume one of these structures is dominant within the four-quark state:

- **mesonic molecules** are narrow and they describe a loose binding of narrow, heavy-light constituents via short range interactions and light-meson exchange. The resulting molecule lies close to the respective two-particle threshold. A prominent candidate is the $X(3872)$, see [4] for details.

- **diquark-antidiquark** states are reviewed for example in [28]. This describes the binding of two colored objects.

- **hadro-quarkonium** [32]: Some exotic states in table 1.1 were so far only found in charmonium + light meson systems, which triggers this idea. The picture related to hadro-charmonium (HC) is a heavy-quark core surrounded by a cloud of light mesons.

Another approach that can distinguish between different sub-clusters is lattice QCD, where one can combine different operators that correspond to the scenarios mentioned above. Also, in our approach all components are potentially present and the system decides dynamically which ones dominate. All approaches have a different resulting spectrum and mass hierarchy and we will discuss them in more detail next.

Lattice QCD

We give a short introduction to lattice QCD hadron spectroscopy based on [33]. The object of interest when computing hadron properties in lattice QCD are Euclidean correlators of the form:

$$C_{ij} = \langle 0|O_i(t)O_j^\dagger(0)|0\rangle = \sum_n Z_i^n Z_j^{*n} e^{-E_n t}, \qquad (1.1)$$

where $Z_i^n = \langle 0|O|n\rangle$, O and $O^\dagger$ are creation and annihilation operators. From the eigenvalues $\lambda_n \propto e^{-E_n t}$ of the correlation matrix C one can extract all finite-volume energies with the quantum numbers of the operator, while the relations to the infinite-volume states are non-trivial. Given the energy levels E_i, several methods exists to extract the infinite volume scattering matrix. Lüscher's method [34, 35] is the most rigorous one. Another approach is to

1. Heavy-light tetraquarks

J^{PC}	state
1^{--}	$Y(4260)$, $Y(4360)$
1^{-+}	$\eta_c(4310)$
0^{-+}	$\eta_c(4140)$, $\eta_c(4320)$
2^{-+}	$\eta_{c_2}(4350)$

Table 1.2.: Predicted spectrum of the hadro-charmonium model in [43].

extract a potential and obtain the phase shift from solving a Schrödinger equation, as already mentioned in section 1.1. Lattice QCD can primarily determine finite-volume energies, but can also provide a qualitative understanding of the states nature by examining overlaps of certain states to certain operators.

When it comes to hadron spectroscopy current studies are plagued by a number of problems, some of which are: small volumes and the continuum limit, coarse lattices and a large pion mass. Furthermore, the rigorous Lüscher formalism is not yet known for all systems and also far from being applied in every study.

As for exotics, the first lattice study of the $X(3872)$ was done in 2013 [36], where a candidate for the $X(3872)$ was found in the $0(1^{++})$ channel. No state was found for $I = 1$, which was also confirmed in [37, 38]. The non-existence of the $Z(3900)$ is further supported by [38, 39]. This is confirmed by a later study [40], where a large base of operators including diquark-antidiquark operators was used. It was found that including a $c\bar{c}$ operator is crucial for the $X(3872)$ to be seen. A charmed partner for the $X(3872)$ (possibly the $X(4140)$) was not found, neither was a candidate for the $Z(3900)$. The non-existence of the $X(4140)$ in $J/\Psi\phi$ is also supported by [41]. A recent study [15] investigated the charmonium energy region including meson-meson and diquark-antidiquark operators, which were found to have a small impact on the resulting energy levels. The study does not support the overall existence of narrow or bound diquark-antidiquark states in the charmonium region at all. However, all of these studies are plagued with one or multiple of the problems mentioned above. Therefore, it is safe to say that none of the statements above are final and further studies have to be conducted.

Models of four-quark states assuming a dominating structure

In the following we give an overview of some models that are frequently discussed in the literature for describing the exotics discussed in the previous section. We base this discussion on [42].

Hadro-charmonium A number of states, for example the $Y(4260)$, $Z(4430)$, $Y(4360)$ and $Y(4660)$ were found in $J/\Psi\pi\pi$, $\Psi(2S)\pi$, $\Psi(2S)\pi\pi$, respectively, but not in decays to open-charm mesons. In the hadro-charmonium picture introduced in [44] these decays seem quite natural. The states are described

	$I(J^{PC})$	$M[MeV]$	$\Gamma[GeV]$
D	0^-	1865	0
D^*	1^-	2007	0.1
D_1	1^+	2420	30
D_2^*	2^+	2460	50

J^{PC}	lowest threshold
0^{-+}	D^*D_1
1^{--}	$D\bar{D}_1$
$0^{++}/1^{+\pm}/2^{++}$	$D\bar{D}^*$

Table 1.3.: Left: candidates for constituents of hadronic molecules. right: lowest lying threshold in each channel. The 0^{++} channel does not allow a $D\bar{D}$ molecule bound by one-π exchange due to parity.

as a heavy-quark core surrounded by a light-quark cloud. Heavy-quark spin symmetry (HQSS) [45] (which is exact in the limit of infinitely heavy quarks) should approximately be conserved in these type of processes. The consequence is that the spin of the heavy-quark system is conserved in its decays. This means that a four-quark state with given spin $S_{c\bar{c}}$ of the subsystem of the $c\bar{c}$ charmonium should decay only into a charmonium plus light meson pair with the same spin $S_{c\bar{c}}$ of the resulting charmonium. The $Y(4260)$ is found in $J/\Psi\pi\pi$ for example, which means its core should be a $\Psi \propto 1_{c\bar{c}}^{--} \otimes 0_{q\bar{q}}^{++}$. However, its appearance in the $h_c\pi^+\pi^-$ cross section alongside the Y(4360) calls for another component $\Psi' \propto 1_{c\bar{c}}^{+-} \otimes 0_{q\bar{q}}^{-+}$ [43] and a mixing between those two states. Via the spin partners of the states due to HQSS this picture leads to a number of predictions listed in table 1.2. $\eta_c(4140)$ and $\eta_c(4320)$ are also mixed states.

Molecule   The molecular interpretation assumes a binding between two color-neutral objects and is originally inspired by the proton-neutron binding inside the deuteron. Often, one-pion exchange potentials combined with some short range part are employed, where the latter allows for either isospin $I = 0$ or $I = 1$ for the resulting molecular state [42]. For such a bound state to be formed, the constituents themselves need to be narrow. Intuitively the state cannot be bound if the range of the interaction is short compared to the decay width of the constituents. That limits the available D mesons to the ones shown in table 1.3. That immediately explains some of the features of the states: The 1^{++} state as $D\bar{D}^*$ should be narrow and at the $D\bar{D}^*$ threshold just like the $X(3872)$. The $Y(4260)$ sits at the $D_1\bar{D}^*$ threshold and has much larger width, which could be due to replacing the D^* with a D_1 meson that itself has a larger width. It also explains the mass gap between the 1^+, the 1^- and the 0^{-+} channels (see figure 1.1), since the lowest lying possible molecule with the constituents listed in table 1.3 for each channel are: $D\bar{D}^*, D\bar{D}_1, D^*\bar{D}_1$. Further testable predictions for this scenario are the non-appearance of states in the 0^{-+} channel below D^*D_1 as well as a $J = 3$ state close to the $D_2\bar{D}^*$ threshold.

Tetraquark models   Some tetraquark models consider interactions between quarks and antiquarks in all combinations [46,47], whereas others assume diquark-

	$M_{0(1^+)}$ $[MeV]$	$M_{1(1^+)}$ $[MeV]$	$M_{1(0^+)}$ $[MeV]$
Karliner [52]	3882(12)		
Junnarkar [53]	3849(11)		-
Eichten [54]	3978	4167	4146

Table 1.4.: We compare open-charm states from references [52–54]. "-" means that an investigation was performed and no binding occured.

and anti-diquark constituents. As mentioned in the introduction, in the literature the word "tetraquark" often stands for this type of bound state. We use it as a synonym for "four-quark state". The idea of bound diquark and antidiquark has already been applied to the light scalar mesons in the 70's [2] and gained a revival with the discoveries of the exotics in the charmonium energy region. In [48] potentials between quarks and between diquarks are constructed and the resulting equations for diquarks and diquark-antidiquarks are solved.

A simple and often discussed model was introduced in [49] and introduces an effective hamiltonian with spin-spin interactions and couplings and yields a mass formula that consequently depends on spin and angular momentum of the diquarks as well as the coupling parameters. It was later extended [50] to include a quark-spin interaction within the diquarks. A feature of this model is a very rich spectrum. Every state in principle appears as an isosinglet and triplet with degenerate masses. The model predicts $4 \cdot 6 = 24$ s-wave states with $(2)0^{++}, 1^{++}, (2)1^{+-}, 2^{++}$ quantum numbers and $4 \cdot 14 = 56$ p waves with quantum numbers $(2)0^{-+}, 0^{--}, (4)1^{--}, (2)1^{-+}, (2)2^{--}, (2)2^{-+}, 3^{--}$. The numbers in parenthesis indicates how many states with this quantum number exist and it is only written down, if it is unequal to one. Recently the same model was reconsidered with a tensor force term added that changes the mass formula and seems to resolve the unexpected feature of decreasing tetraquark mass for increasing total spin [51]. With the right parameters some of the known states, such as $Z(3900)$, $Z(4020)$, $X(3872)$, as well as possibly four Y states and the $X(3915)$ and $X(3940)$ can be identified with the states predicted by the model. However, there are many more states predicted that have not been found so far.

The open-charm states

The open-charm and open-bottom states should predominantly be seen in decays to a heavy-light meson and another heavy-light meson in experiment, not to a heavy-light meson and a heavy-light antimeson pair, where one finds the hidden-charm and hidden-bottom states.

Especially the heavy-light bottom tetraquarks with quark content $bb\bar{q}\bar{q}$ received a lot of attention in recent years, since they are promising candidates for deeply bound and narrow states. See for example [55–58]. However, some studies about open-charm tetraquarks exist:

Open-charm tetraquarks should be stable in the heavy-quark limit as laid out

in [54]. In this reference the open-charm tetraquarks are related to the masses of QQq and Qqq baryons and $Q\bar{q}$ mesons, where Q and q stand for a heavy-and light quark, respectively. Model calculations are used for the masses of QQq, whereas the others are taken from experiment. A feature of this phenomenological approach is that the isospin $I = 1$ state is heavier then the $I = 0$ state in the axialvector channel; another is that the spin triplet of $0^+, 1^+, 2^+$ states are very close in mass.

Within a study using QCD sum rules [59] no current describing open-charm tetraquarks with quark content $cc\bar{q}\bar{q}$ with $J^P = 0^+$ or $J^P = 1^+$ lead to a bound state. In contrast, the authors find several $cc\bar{s}\bar{s}$ states.

Some lattice studies exist [60], where evidence for an attractive interaction in the $0(1^+)$ channel, but probably not in the $I = 1$ channel, is found. A recent work [53] suggests no binding for spin zero states, but energies below threshold for spin one states, which indicates binding. We compile some results in table 1.4 for an overview of these different approaches.

Tetraquarks in the DSE BSE approach

Throughout this chapter we work with the DSE-BSE framework in the rainbow-ladder (RL) truncation. The framework is fully relativistic, non-perturbative and can (together with a truncation scheme) be derived from QCD, as is shown in sections 1.2 and 1.3. We solve a genuine four-body BSE where quarks and antiquarks interact via the exchange of gluons [3]. So, a priori we have no information about HLM, HC or DI components. However, the tensor basis for the tetraquark amplitude carries that information. In the following we expand it with respect to meson-meson and diquark-antidiquark components and the equation will determine dynamically which components are important during the solution process. For the hidden-charm tetraquarks all three clusters: HLM, HC and DI are present in the tetraquark amplitude and we can successively switch on and off sub-clusters to investigate their impact on the resulting tetraquark mass. Furthermore, different terms within one sub-cluster can appear. The $0(0^{++})$ $cq\bar{q}\bar{c}$ state, for example, contains $D\bar{D}$ and $D^*\bar{D}^*$ terms in its amplitude and their impact can be investigated.

The possible terms in a tetraquark amplitude are determined by its quantum numbers $I(J^{P(C)})$ and symmetry constraints. The $cq\bar{q}\bar{c}$ tetraquarks obey charge-conjugation symmetry, whereas the $cc\bar{q}\bar{q}$ tetraquarks respect the Pauli principle, which will lead to different terms in their amplitude. We discuss this in detail in section B.1.1.

In the following we will start with the QCD lagrangian and build up the DSE-BSE framework step by step.

1.2. General concepts in QCD

QCD is the theory of the strong interaction, for a pedagogical introduction see for example [61]. Its basic fields carry a color charge and are the massive quarks and massless gluon fields that mediate the interaction. Although quarks carry a mass, it is quite small in comparison to their "constituent" mass in hadrons. This is a consequence of chiral symmetry breaking: Chiral symmetry appears in the limit of vanishing quark masses and is therefore broken explicitly by the quark masses but is broken spontaneously as well. This leads to dynamical mass generation of quarks within hadrons.

These hadrons are, in contrast to the fundamental fields, color neutral and quarks and gluons only appear confined into these colorless bound states. One possible implementation of confinement is a linear rising potential. In such a scenario one needs to add more and more energy to drag a quark-antiquark pair apart from each other, until eventually there is enough energy for the creation of another quark-antiquark pair out of the vacuum, which results in two colorless bound states instead of a spatially separated quark-antiquark pair.

QCD is a strongly coupled theory, which means the coupling is small only for large momenta which leads to the notion of asymptotic freedom. In contrast to QED, for example, a perturbative expansion in the coupling at small momenta can therefore not be meaningful and one needs other tools to extract hadron properties from QCD. One such tool are the DSEs. They are the exact equations of motions of a field theory and can be used for investigating fundamental phenomena as well as phenomenology. They are an infinite set of coupled integral equations that connect all n-point functions of the theory. Together with a truncation of the infinite tower of equations they can be used to self-consistently calculate fundamental propagators and vertices. These can afterwards serve as input into BSEs that themselves deliver a variety of information about the bound states and resonances of the theory at hand.

1.2.1. Generating functionals

Generating functionals are a useful tool and the DSEs can be derived from them. An introduction to the path integral formalism and generating functionals can be found in [62]. Given the action $S(\phi)$ for a set of fields ϕ of a field theory, we can define the generating functional Z:

$$Z[J] = \int \mathcal{D}\phi \; e^{-S + \int_x J(x)\phi(x)}, \qquad (1.2)$$

where $J(x)$ is the set of corresponding sources to those fields. We use Euclidean conventions analoguous to [63] (see equation 3.10 therein). The physics is encoded in the n-point functions of the theory, which are vacuum expectation values of time ordered products of fields. Those can be obtained from the generating functional by functional derivatives with respect to the sources $J(x)$ via

$$\langle f \rangle = \langle 0|Tf(\phi)|0 \rangle = f\left(\frac{\delta}{\delta J}\right)\bigg|_{J=0} \frac{Z[J]}{Z[0]}. \tag{1.3}$$

T stands for the time ordering and f is a general polynomial of the set of fields ϕ. $Z[J]$ as we have defined it so far creates the connected n-point functions. One can now define the effective action Γ via a Legendre transformation from the functional W:

$$W[J] = \ln(Z[J]), \qquad \Gamma[\tilde{\phi}] = \int_x J(x)\tilde{\phi} - W[J]. \tag{1.4}$$

By definition the "average field" $\tilde{\phi} = <\phi(x)>_J$ is the vacuum expectation value of ϕ in the presence of the source J. The derivatives of Γ produce one-particle irreducible (1PI) n-point functions. One can now calculate the vacuum expectation value in the presence of a source J:

$$\langle f(\phi) \rangle_J = f\left(\frac{\delta W[J]}{\delta J} + \frac{\delta}{\delta J}\right) = f\left(\tilde{\phi} + \int_y \Delta_{xy}[\tilde{\phi}]\frac{\delta}{\delta\tilde{\phi}(y)}\right). \tag{1.5}$$

This formula should be read in the following way: replace every occurrence of ϕ in f with the expression in parentheses[1]. We used the abbreviation:

$$\Delta_{xy}[\tilde{\phi}] = \left(\frac{\delta^2\Gamma[\tilde{\phi}]}{\delta\tilde{\phi}(x)\delta\tilde{\phi}(y)}\right)^{-1}.$$

1.2.2. QCD Lagrangian

The QCD lagrangian $\mathcal{L}$ is constructed via imposing local SU(3) color symmetry on the quark fields Ψ and $\bar{\Psi}$, which transform according to

$$\Psi' = U\Psi, \qquad \bar{\Psi}' = \bar{\Psi}U^\dagger. \tag{1.6}$$

U stands for a $SU(3)$ color transformation. Thereby the massless color octet gluon field, $A_\mu(x) = \sum_a A_a^\mu t_a$ with $t_a = \lambda_a/2$ and λ_a the Gell-Mann matrices, is introduced. It transforms according to:

$$A'_\mu = UA_\mu U^\dagger + \frac{i}{g}U\partial_\mu U^\dagger, \qquad F'_{\mu\nu} = UF_{\mu\nu}U^\dagger, \tag{1.7}$$

where we have defined the gluon field strength tensor $F_{\mu\nu} = \partial_\mu A_\nu - \partial_\nu A_\mu - ig[A_\mu, A_\nu]$, with the coupling g. It can be rewritten as

$$F_{\mu\nu} = F_{\mu\nu}^a t_a = (\partial_\mu A_\nu^a - \partial_\nu A_\mu^a + gf_{abc}A_\mu^b A_\nu^c)t_a,$$

---

[1]See [64] for a pedagogical derivation and further details.

where f_{abc} are the structure constants of $SU(3)$. With this definition, the QCD Lagrangian in Minkowski space is

$$\mathcal{L}_M = \bar{\Psi}(x)(i\slashed{D} - m)\Psi(x) - \frac{1}{4}F_{\mu\nu}^a F_a^{\mu\nu}. \tag{1.8}$$

We suppressed the color and Dirac indices of Ψ and a sum over different quark flavors is implied. $D_\mu = \partial_\mu - igA_\mu$ is the covariant derivative and m the quark mass.

In the QCD path integral we integrate over all field configurations ϕ, however, some configurations are related by gauge transformations and hence are physically equivalent. The Faddeev-Popov method [65] removes that redundancy. As a consequence unphysical ghost fields and a gauge parameter ζ are introduced. Physical observables have to be independent of the gauge parameter, but n-point functions are in general not independent. In our calculations we will work in Landau gauge, where $\zeta \to \infty$. Furthermore, we introduce renormalization constants for the quark, gluon and ghost fields, as well as mass and vertex renormalization:

$$\Psi = \sqrt{Z_2}\Psi_R, \qquad A = \sqrt{Z_3}A_R, \qquad c = \sqrt{Z_c}\,c_R,$$
$$m = Z_m m_R, \qquad g = Z_g g_R, \tag{1.9}$$

where the subscript R stands for renormalized quantities. After the transformation to Euclidean space we finally arrive at the Lagrangian:

$$\mathcal{L} = Z_2\bar{\Psi}(\slashed{\partial} + Z_m m)\Psi - iZ_g Z_2 \sqrt{Z_3}g\bar{\Psi}\slashed{A}\Psi + \frac{Z_3}{2}A_\mu^a(-\partial^2\delta^{\mu\nu} + \partial^\mu\partial^\nu)A_\nu^a +$$
$$Z_g Z_3^{3/2}gf_{abc}A_b^\mu A_c^\nu \partial^\mu A_a^\nu + Z_g^2 Z_3^2 \frac{g^2}{4}f^{abe}f^{cde}A_a^\mu A_b^\nu A_c^\mu A_d^\nu +$$
$$Z_c\bar{c}\partial^2 c^2 + Z_c Z_g \sqrt{Z_3}gf^{abc}\bar{c}^a\partial^\mu(A^{c,\mu}c^b), \tag{1.10}$$

where c is the ghost field and we have dropped the subscript R for convenience. From this form of the Lagrangian we can read off the tree level QCD propagators and vertices: The quark, gluon and ghost propagator together with the ghost, three and four-gluon vertices.

1.2.3. DSEs

The DSEs were introduced by Dyson and Schwinger already in 1950 [66, 67]. A pedagogical derivation for the quark, gluon and ghost DSEs can be found in [68], see also [69]. QCD applications are reviewed among others in [70–73] and in Minkowski space in [74]. One way to derive DSEs is via a master DSE that follows from the invariance of the path integral under a shift of the fields: $\langle\frac{\delta S[\phi]}{\delta\phi(x)}\rangle_J = J(x)$. In connection with (1.5) one obtains the master DSE:

$$\Gamma_x'[\tilde{\phi}] = \frac{\delta S}{\delta\phi}\left(\tilde{\phi} + \int_y \Delta_{xy}[\tilde{\phi}]\frac{\delta}{\delta\tilde{\phi}(y)}\right). \tag{1.11}$$
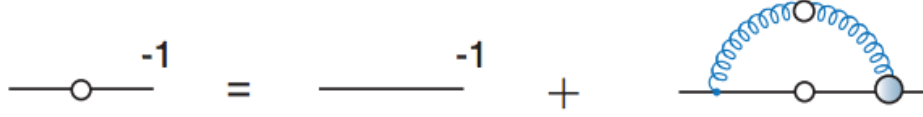
Figure 1.2.: The quark DSE is shown. The blue dot stands for the full quark-gluon vertex and the white dots for dressed quark and gluon propagators.

The notation again means replacing the field ϕ with the content of the parentheses. The quark propagator for example now is defined as $W''_{xy}[J]$. From the master-DSE (1.11) and

$$\int_y W''_{xy}[J]\Gamma''_{yz}[\tilde{\phi}] = \delta^4(x - z) \tag{1.12}$$

we can now derive the DSE for the inverse quark propagator via a second derivative. After a transformation to momentum space the result is schematically:

$$S^{-1}(p) = S_0^{-1}(p) + \Sigma(p),$$

or in more detail:

$$S^{-1}(p) = Z_2(-i\not{p} + Z_m m) + g^2 Z_{1f} C_f \int_q D^{\mu\nu}(p - q)\Gamma^\mu(q, p)S(q)\gamma^\nu, \tag{1.13}$$

where we defined $Z_{1f} = Z_g Z_2 Z_3^{1/2}$. We present the equation graphically in figure 1.2. The full inverse quark propagator is given by the bare inverse propagator plus a self-energy term. We drag an additional factor of $i \cdot g$ out of the dressed quark-gluon vertex so that we can later model a renormalization point independent quantity[2] and take the color trace resulting in $C_f = 4/3$. S stands for the dressed renormalized quark propagator, $D^{\mu\nu}$ for the dressed renormalized gluon propagator, and Γ^μ for the derivative of the effective action with respect to $\Psi, \bar{\Psi}$ and A_μ^a and the shorthand $\int_q$ is written out in the appendix, see A.1.

The quark propagator is an important ingredient for the bound state calculations in this thesis and we will come back to it in section 1.3, where we will later introduce a model for the unknown quantities Γ^μ and $D^{\mu\nu}$ to solve for S.

1.2.4. BSEs and T-matrices

In the following we will introduce the BSEs for n-particle bound states. Therefore, we introduce first $G^{(n)}$, which is the n-point function with n incoming and n outgoing quarks. It fulfills the Bethe-Salpeter equation [75]:

$$G^{(n)} = G_0^{(n)} + G_0^{(n)} K^{(n)} G^{(n)}. \tag{1.14}$$

---

[2]See equation 3.22 in [63].

1. Heavy-light tetraquarks

$K^{(n)}$ stands for the scattering kernel, $G_0^{(n)}$ is the direct product of n dressed quark propagators. $K^{(n)}G_0^{(n)}$ for example implies loop integrals and contraction of Dirac-and color indices. The amputated connected counterpart $T^{(n)}$ is defined as:

$$G^{(n)} \equiv G_0^{(n)} + G_0^{(n)}T^{(n)}G_0^{(n)} \tag{1.15}$$

and it obeys a scattering or Dyson equation:

$$T^{(n)} = K^{(n)} + K^{(n)}G_0^{(n)}T^{(n)}. \tag{1.16}$$

One can recursively plug the right hand side of the equation into itself to receive an infinite summation of the scattering kernel $K^{(n)}$ with propagators in between.

As mentioned before, the physics of the theory is encoded in these n-point functions: Poles of $G^{(n)}$ or $T^{(n)}$ in the squared total momentum variable P^2 correspond to bound states for $P^2 \in \mathcal{R}$ and resonances for $P^2 \in \mathcal{C}$. It is for that reason desirable to determine these pole locations, since they provide information about the mass and width of the physical states. For a given scattering kernel one could now go ahead and calculate the quantities G or T directly and this has been done, see [8] for a recent example. It is, however, more convenient to calculate only the properties at the poles and not the whole quantity in practice. If one evaluates equation (1.16) near the pole location

$$T^{(n)} \xrightarrow{P^2 \to -M^2} \frac{\Gamma^{(n)}\bar{\Gamma}^{(n)}}{P^2 + M^2},$$

one arrives at the homogeneous BSE [76]:

$$\Gamma^{(n)} = K^{(n)}G_0^{(n)}\Gamma^{(n)}. \tag{1.17}$$

$\Gamma^{(n)}$ stands for the residue of $T^{(n)}$ at the pole location. An extensive review including a derivation and early applications is [77].

We are in this thesis interested in solving two and four-body BSEs for mesons and tetraquarks, respectively. The solution technique for these type of equations is simply explained: We transform the equation into an eigenvalue problem, see appendix 1 for details, and find the point P_{phys}^2 where the eigenvalue $\lambda_i(P^2 = P_{phys}^2) = 1$, where P is the total momentum of the bound state. The mass and possibly the width can then be extracted from the real and imaginary part of P_{phys}^2. While the above condition is fulfilled for real P^2 for a bound state, a resonances has a pole in higher Riemann sheets and lies above some decay threshold. Therefore, one needs advanced methods including contour deformation and a suitable analytic continuation to access the eigenvalue curve on higher sheets. We will do this for the ρ and σ resonance in chapter 2.

An alternative way to obtain the pole location is to look directly for its position using an inhomogeneous BSE. It is easily constructed from equation

(1.14) after projecting with a Dirac-flavor tensor Γ_0 representing the desired quantum numbers [78]. If we define $\hat{\Gamma}^{(n)} = G^{(n)}\Gamma_0^{(n)}$ we can solve for the pole of $\hat{\Gamma}^{(n)}$ in the inhomogeneous BSE:

$$\hat{\Gamma}^{(n)} = \Gamma_0^{(n)} + K^{(n)}G_0^{(n)}\hat{\Gamma}^{(n)}. \tag{1.18}$$

$\hat{\Gamma}^{(n)}$ has a pole whenever KG_0 has unit eigenvalue, which can be seen in the symbolic solution:

$$\hat{\Gamma}^{(n)} = \frac{\Gamma_0^{(n)}}{1 - (KG_0)^{(n)}}, \tag{1.19}$$

which confirms what we already know from the homogeneous BSE.

Consistent kernel and self-energy   We know now what BSEs look like. However, it is still unclear how a suitable kernel can be constructed. A connection to the DSEs we discussed in the last section can be made via the nPI formalism. It goes back to [79] and is similar to introducing sources and derivatives we used in the path integral to derive vacuum-expectation values for n-point functions. However, one introduces bilocal and trilocal sources etc. and derivatives for terms with higher field order. The connection between 2PI and quark-antiquark BSEs is pedagogically explained in [78]: The kernel is the double derivative of the interacting part of the 2PI effective action and consequently the derivative of the self-energy, which we schematically write down as:

$$\frac{\delta\Sigma}{\delta S} = K^{(2)}, \tag{1.20}$$

where $K^{(2)}$ is the two-body kernel, S the quark propagator and Σ again the self-energy that appeared in equation (1.13). In the rainbow-ladder truncation we will introduce in section 1.3, the scattering kernel can be constructed in that way and it automatically fulfills the axial-vector Ward-Takahashi identity (AVWTI):

$$\left(\gamma^5\Sigma(p_-) + \Sigma(p_+)\gamma^5\right)_{\alpha\beta} = -\int_q K_{\alpha\gamma,\delta\beta}^{(2)}(p,q,P)\left(\gamma^5 S(q_-) + S(q_+)\gamma^5\right)_{\gamma\delta}. \tag{1.21}$$

Here $q_\pm = q \pm P/2$, where q and p are relative momenta and P is the total momentum. The AVWTI in its original form can be found for example in equation 4.27 in [80]. One can recast it into the form given here by use of the quark DSE and the inhomogeneous meson BSE (1.18) for the pseudoscalar and axialvector vertex.

This way, the correct properties in the chiral limit are ensured as we will see in the example of the pion in section 1.3. The full four-body kernel $K^{(4)}$ we will

use for the tetraquark equation consists of irreducible two, three and four-body interactions denoted by $K'^{(i)}\, i = 2, 3, 4$:

$$K^{(4)} = K'^{(4)} + K'^{(3)} + K'^{(2)}. \tag{1.22}$$

We will come back to its exact form in section 1.4.

Previous work   The method of using DSEs and BSEs for calculating bound state properties (see [81,82] for detailed reviews on the technique) is an old idea and has been applied to baryons and mesons, see [80] and references therein. (We will discuss mesons in particular in sections 1.3.3 and 2.1.2.) The framework has also been applied to glueballs [83], tetraquarks [3,84] and hybrids [85]. We will in the following discuss a common truncation scheme, the rainbow-ladder truncation (RL).

1.3. Rainbow-ladder truncation and Maris-Tandy model

1.3.1. Kernel and self-energy

Earlier in this section we have presented the quark DSE (1.13), which is up to this point an exact equation of QCD. However, the gluon propagator $D^{\mu\nu}$ and the quark-gluon vertex Γ^μ fulfill their own DSEs, which couple to higher derivatives of the effective action themselves. This leads to an infinite set of coupled equations. The RL framework we use in the following was introduced in [86] and models the combination of quark-gluon vertex and dressed-gluon propagator in Landau gauge to obtain a decoupled quark DSE that can be solved for the quark propagator. With the approximation $\Gamma^\mu(p,k) \to \gamma^\mu \Gamma(k^2)$, the gluon-dressing function Z, the coupling g and the renormalization constants Z_2 and Z_c from equation (1.9), the Maris-Tandy model reads:

$$\frac{g^2 Z(k^2)\Gamma(k^2)}{Z_c Z_2} \equiv G(k^2) = 4\pi^2 \left(x^2 \eta^7 e^{-\eta^2 x} + \frac{2\gamma_m \left(1 - e^{\frac{-k^2}{4m_t^2}} \right)}{\ln \left[\tau + \left(1 + \frac{k^2}{\Lambda_{QCD}^2} \right)^2 \right]} \right), \quad (1.23)$$

where $x = k^2/\Lambda^2$, $\gamma_m = (12/(11N_c - 2N_f))$, $N_c = 3$, $N_f = 4$, $m_t = 0.5$ GeV, $\tau = e^2 - 1$ and $\Lambda_{QCD} = 0.234$ GeV as well as the parameter η and scale parameter Λ. The first term on the right hand side of equation (1.23) determines the infrared behavior while the second term ensures the one-loop renormalization group structure of QCD [87].

The combination on the left hand side of the equation is renormalization point (μ) independent and therefore a good quantity to model and it absorbs all unknowns in the Quark DSE, as we can see after using the Landau gauge relation $1 = Z_g Z_c \sqrt{Z_3}$ and plugging the gluon propagator $D^{\mu\nu}(k) = T^{\mu\nu}(k)\frac{Z(k^2)}{k^2}$ into equation (1.13):

$$S^{-1}(p,\mu) = Z_2(\mu^2,\Lambda^2)(-i\not{p} + mZ_m(\Lambda^2)) + \qquad (1.24)$$

$$Z_2^2(\mu^2,\Lambda^2)C_f \int_q^\Lambda \frac{G(k^2)}{k^2} T_k^{\mu\nu} \gamma^\mu S(q,\mu)\gamma^\nu,$$

where

$$k = p - q, \qquad T_k^{\mu\nu} = \delta^{\mu\nu} - \frac{k^\mu k^\nu}{k^2}$$

and m is the renormalized quark mass. We explicitly showed the dependence of the renormalization constants on the scale μ and the cutoff Λ that is used for the q^2 integral above, see A.1.

The equation comes with two renormalization conditions $A(\mu) = 1$ and $B(\mu) = m_q$, where m_q is the quark mass. Therefore, the parameters in the model are η, Λ and the quark masses m_u, m_s and m_c, which are fixed from

experimental input. In our case we use $m_\pi, f_\pi, m_D + m_D^*$ and $m_{D_s} + m_{D_s^*}$ to reproduce the experimental values. C_f evaluates to $4/3$.

As discussed before we need a consistent scattering kernel with this approximation of the quark self-energy. The field independence of the vertex makes it easy to impose (1.20). Graphically one can cut the self-energy with respect to the quark line, since the vertex is quark propagator independent in our truncation. The result is the scattering kernel which is guaranteed to preserve the AVWTI (1.21). This procedure ensures chiral-symmetry breaking is present. The resulting kernel is a dressed one-gluon exchange:

$$K^{(2)}(k) = -Z_2^2 \frac{G(k^2)}{k^2} T_k^{\mu\nu} \left[\left(\frac{\lambda^i}{2} \gamma^\mu \right) \otimes \left(\frac{\lambda^i}{2} \gamma^\nu \right) \right], \qquad (1.25)$$

where λ stands for the Gell-Mann matrices. A pedagogical treatment of the connection of Σ and $K^{(2)}$ from the 2PI formalism can be found in [80] around Eq. (3.101). The scattering kernel $K^{(2)}$ is the two-body interaction of quarks within mesons and tetraquarks.

1.3.2. Quark propagator

The quark propagator is now the only unknown in the quark DSE of equation (1.24) that is shown graphically in figure 1.2. In general, the inverse dressed quark propagator has two dressing functions that depend on the squared momentum $\sigma_v(p^2)$, $\sigma_s(p^2)$ and can be defined in terms of these two dressing functions:

$$S^{-1}(p, \mu) = -i\not{p}\, \sigma_v(p^2, \mu^2) + \sigma_s(p^2, \mu^2). \qquad (1.26)$$

In terms of the widely used A, B dressing functions, they are given by:

$$\sigma_v(p^2, \mu^2) = \frac{A(p^2, \mu^2)}{A^2(p^2, \mu^2)p^2 + B^2(p^2, \mu^2)}, \ \sigma_s(p^2, \mu^2) = \frac{B(p^2, \mu^2)}{A^2(p^2, \mu^2)p^2 + B^2(p^2, \mu^2)}.$$

One can now solve (1.24) by iteration with the renormalization conditions mentioned above, to obtain $A(p^2), B(p^2), Z_2$ and Z_m at the renormalization point μ, which we choose as $\mu = 19$ GeV.

In the RL truncation, the quark propagator develops complex conjugated poles, as can be seen from the absolute value of σ_v, which is shown in the left panel of figure 1.3. The analytic structure within different models has been investigated in [88]. In the right panel one can see different solutions for the quark-mass function which is defined as $M(p^2) = B(p^2)/A(p^2)$. The results show a strong enhancement of the mass in the infrared, which is a consequence of dynamical chiral symmetry breaking. This effect is particularly strong for the chiral and light quarks, which have zero and a very small current-quark mass for large momenta, respectively.

1.3.3. Mesons and diquarks

$q\bar{q}$ states have been investiagated in the bottomonium [89–91], light [92–94], charmonium [89, 90] as well as the heavy-light sector [95–97] in the BSE-DSE
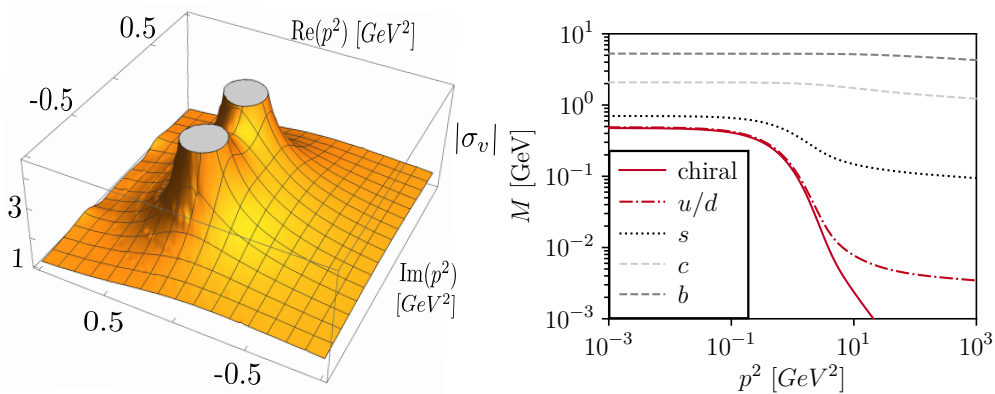
Figure 1.3.: Left: The quark propagator is shown for complex values of p^2. One can see complex conjugated poles. Right: The solution for the quark-mass function $M = B/A$ is shown as a function of p^2.

framework. While the spectra can be described quite well for bottomonium and reasonably for charmonium, the situation gets worse for the light-light sector. However, there seems to be a common pattern for all the systems above: The (isotriplet) pseudoscalar and vector mesons come out reasonably well, whereas especially the axialvector and scalar states do not. As we will see in detail in section 2.1, the pseudoscalar and vector states are the Quark-model s-wave states, whereas the scalar and axialvectors are p waves in the Quark model. The defficiency of the RL model in the latter channels is also seen in other studies [98] and is probably due to the oversimplification of the quark-gluon vertex, where other structures beyond the γ^μ component are neglected in the RL truncation.

Diquarks also appear as bound states in the RL truncation [99], which will later be crucial for our diquark-antidiquark components in the tetraquark, because we calculate the diquark masses consistently from the qq BSE without the need for additional model input.

Important for our purpose are mainly pseudoscalar and vector $c\bar{q}, q\bar{q}, c\bar{c}$ states as well as scalar and axialvector qq, cq, cc diquarks, since they are part of our tetraquark scalar and axialvector amplitudes in the form of intermediate meson-meson components. The calculation of heavy-light states containing c and q quarks is plagued by some technical difficulties, which we will explain after introducing the BSE.

BSE We have presented the homogeneous BSE in equation (1.17) and the RL kernel for quark-antiquark interactions in (1.25). The homogeneous BSE for $J = 0$ ($J = 1$) $q\bar{q}$ states consequently reads:

$$\Gamma^{(\mu)}_{\alpha\beta}(p, P) = \int_q K^{(2)}_{\alpha\alpha'\beta'\beta}(q - p) S_{\alpha'\alpha''}(q_+) \Gamma^{(\mu)}_{\alpha''\beta''}(q, P) S_{\beta''\beta'}(q_-), \qquad (1.27)$$

where S is the quark propagator, $K^{(2)}$ the two-body kernel, p, q are relative momenta and P is the total momentum. Also, we have suppressed all color
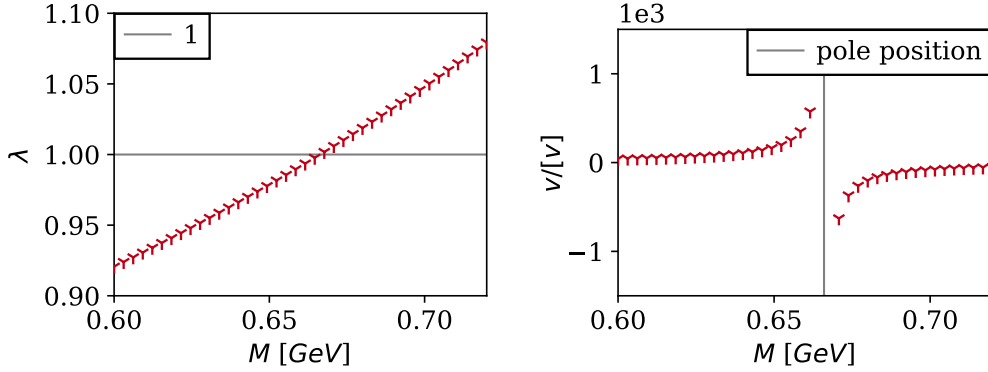
Figure 1.4.: The homogeneous (left) and inhomogeneous (right) solutions for the RL $0(0^{++})$ state are shown. The eigenvalue curve hits $\lambda(M = M_{q\bar{q}}) = 1$ and $v(P^2) = f_1(p^2 = 0, z = 0, P^2)$ has a pole at $M = M_{q\bar{q}}$, where $z = \hat{p} \cdot \hat{P}$ and p, P stand for the relative and total momentum, respectively. The hat denotes unit vectors.

indices. The other momenta are:

$$q_+ = q + \sigma P, \qquad q_- = q - (1-\sigma)P.$$

We introduced the momentum partitioning parameter σ. The amplitude $\Gamma^{(\mu)}$ can be written as:

$$\Gamma^{(\mu)}(p, P) = \sum_i f_i(\Omega)\tau_i^{(\mu)} \otimes \Gamma_C \otimes \Gamma_F. \tag{1.28}$$

The explicit structure of the flavor Γ_F and Dirac part $\tau_i^{(\mu)}$ depend on the quantum numbers of the state. For $q\bar{q}$ states a general construction is given in [100] and a pedagogical discussion can be found in [101]. With respect to color, quarks and antiquarks combine via $3 \otimes \bar{3} = \mathbb{1} \oplus \mathbb{8}$ and the color part Γ_C is proportional to $\mathbb{1}$ for physical $q\bar{q}$ states. Neutral equal-mass mesons carry definite charge conjugation property while diquarks obey the Pauli principle.

As a consequence of the flavor-blind RL kernel of equation (1.25), the flavor amplitude drops out after taking the flavor trace. For the ρ and σ meson we discuss in chapter 2, as well as for the tetraquark calculations we perform later in this chapter, we need a scalar, pseudoscalar and vector-Dirac basis and we collect them all in table 1.5.

The Dirac basis elements τ_i depend on two quark momenta or equivalently on a relative and total momentum q and P. The dressing functions depend on the set of Lorentz invariants $\Omega = \{q^2, q \cdot P, P^2\}$. We work in the rest frame and can accordingly choose the four-momenta as:

τ_1^μ	τ_2^μ	τ_3^μ	τ_4^μ	τ_5^μ	τ_6^μ	τ_7^μ	τ_8^μ
1^{--} G_3^μ	$\tau_1^\mu \hat{P}$	iG_1^μ	$-iz\tau_3^\mu\hat{P}$	$(3G_2^\mu - G_3^\mu)$	$z\tau_5^\mu\hat{P}$	$z(G_4^\mu - G_1^\mu)$	$\tau_7^\mu\hat{P}z^{-1}$

	τ_1	τ_2	τ_3	τ_4
0^{-+}	γ_5	$\gamma_5\hat{P}$	$z\hat{\slashed{p}}_\perp\gamma_5$	$i\hat{\slashed{p}}_\perp\hat{P}\gamma_5$
0^{++}	$\mathbb{1}$	$z\hat{P}$	$\hat{\slashed{p}}_\perp$	$i\hat{\slashed{p}}_\perp\hat{P}$

Table 1.5.: Dirac basis for mesons with quantum numbers $J^{PC} = 0^{-+}$ and 0^{++} with $\gamma_\perp^\mu = T_P^{\mu\nu}\gamma_\nu$, $\hat{\slashed{p}}_\perp = t_P^{\alpha\beta}\hat{p}^\alpha\gamma^\beta$ and Dirac basis for the 1^{--} vector meson. $G_1^\mu = (\hat{p}^\mu)_\perp$, $G_2^\mu = G_1^\mu\cdot\hat{\slashed{p}}_\perp$, $G_3^\mu = \gamma_\perp^\mu$, $G_4^\mu = \gamma_\perp^\mu\hat{\slashed{p}}_\perp$, $\slashed{t} = \hat{P}$ and $z = \hat{p}\cdot\hat{P}$.

$$p^\mu = \sqrt{p^2}\begin{pmatrix}0\\0\\\bar{z}\\z\end{pmatrix}, \qquad q^\mu = \sqrt{q^2}\begin{pmatrix}0\\\bar{z}_q\bar{y}_q\\\bar{z}_qy_q\\z_q\end{pmatrix}, \qquad P^\mu = \begin{pmatrix}0\\0\\0\\iM\end{pmatrix}. \qquad (1.29)$$

We introduced the angles $z, z_q, y_q \in [-1, 1]$, with $\bar{x} = \sqrt{1 - x^2}$. M is the mass of the bound state.

Quarks in the BSE The quark propagators dressing functions in (1.27) are sampled at $q_\pm^2 \in \mathbb{C}$, which is a parabola in the complex plane for fixed M. This parabola is limited by the poles in the quark propagators' dressing functions that we have seen earlier in figure 1.3. The situation is shown in figure 1.5: The apex is at $-M^2\sigma^2$ and the width of the parabola is proportional to σ. The optimal σ for equal mass quarks is $\frac{1}{2}$. σ can be varied for unequal quark masses to optimize for a maximal M that one can put into the BSE.

Solutions As already mentioned, we use the Nystrom method [102] to solve the integral equation (1.27) as an eigenvalue problem. Details can be found in the appendix A.2.2. We employ a Gauss-Legendre quadrature in all variables except the angle z_q, where a Gauss Tschebychev quadrature (see section A.2.1) is more suitable because of the factor $\sqrt{1 - z_q^2}$ from the spherical coordinates of equation (A.1). We can alternatively solve the inhomogeneous equation (1.18) for a pole in the amplitude, which we will also do in chapter 2. We use the biconjugate gradient stabilized algorithm (bicgstab) from [103], since it is more stable and shows better convergence properties then power iteration [81]. The comparison of the methods is shown for a σ calculation in figure 1.4. In the left panel we see that the eigenvalue curve crosses one at the same point M_σ, where a pole emerges in the amplitude $v(M) = f_1(p^2 = 0, z = 0, M)$ when we solve the inhomogeneous equation.
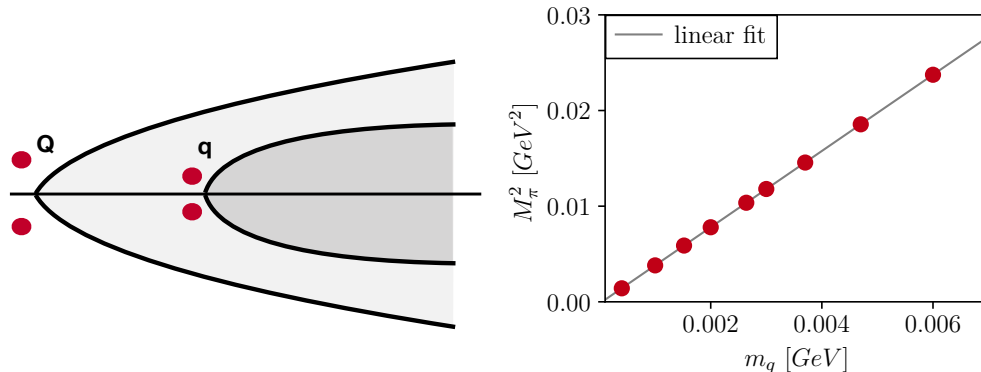
Figure 1.5.: Left: The quark propagator dressing functions A and B are sampled within a parabola (grey shaded area) during a bound state calculation. The dots are the quark-propagator poles shown in figure 1.3 for a heavy and light quark Q and q, respectively. A clever choice of the partitioning parameter σ can allow a bigger M_{max}. Two parabolas with different partitioning parameters are shown. Right: We show the squared pion mass as a function of the quark mass.

For any realistic truncation of QCD it is of great importance that chiral symmetry breaking is implemented. The Gell Mann-Oakes-Renner relation

$$f_\pi^2 m_\pi^2 = \frac{m_u + m_d}{2} \left\langle \bar{u}u + \bar{d}d \right\rangle$$

shows, how the pion mass and decay constant m_π and f_π relate to the quark masses m_u, m_d and the quark condensate $\langle \bar{q}q \rangle \propto \int_p \mathrm{Tr} S(p)$, where $S(p)$ is the quark propagator. One can see that the pion acquires mass by explicit chiral symmetry breaking, due to the non zero quark masses, in combination with dynamical chiral symmetry breaking, due to the non vanishing trace of the quark propagator. For vanishing quark masses m_u and m_d the pion should become massless, which it does in the RL truncation, see the right panel of figure 1.5.

Heavy-light mesons and diquarks

Heavy-light meson systems have been investigated in the RL framework and beyond within certain approximations [95–97]. The discriptions share two common problems:

Firstly, one can not directly access the physical D meson masses where the eigenvalue $\lambda(M = M_D) = 1$ in the RL truncated BSE of equation (1.27). Let us understand why: The BSE involves two quark propagators that are sampled in the complex plane during the solution process. For two quarks q and c the pole positions in the complex plane are different, as indicated in the left panel of figure 1.5. Due to those poles, there is a maximal M_u and M_c that the quark

parabolas can access, before hitting the quark poles:

$$q_\pm^2 = q^2 - \sigma_\pm^2 M_{u,c}^2 + 2i\sqrt{q^2}\sigma_\pm M_{u,c},$$

where $\sigma_+ = \sigma$ and $\sigma_- = 1 - \sigma$. Since the quark poles are calculated from the DSE in our case, M_q and M_c are an inherent property of the RL truncated system. These conditions translate into conditions for the maximal mass M_{max} of the meson whose BSE is solved:

$$M_{max} \leq \frac{M_u}{\sigma}, \qquad M_{max} \leq \frac{M_c}{(1-\sigma)},$$

where $M_c \gg M_u$ and the choice $\sigma = 1/2$ that was optimal for equal-mass mesons, produces a very small M_{max} in this case. We improve the situation by the following technique: We choose an optimal momentum partitioning parameter σ that maximizes M_{max}:

$$\sigma = \frac{M_q}{M_u + M_c}, \qquad 1 - \sigma = \frac{M_c}{M_u + M_c}, \tag{1.30}$$

which results in the condition $M_{max} \leq M_u + M_c$. Effectively, we assign a large fraction of the complex momentum P to the c quark and a small fraction to the q quark, which allows for an overall higher M_{max}. The situation is shown in the left panel of figure 1.5. Both parabolas are as close as possible to their respective poles, which means each one absorbs a maximum amount of the total momentum P.

Although M_{max} is now closer to the physical D meson mass, $\lambda(M) = 1$ can still not be reached for $M < M_{max}$. Therefore, we calculate a mass curve $M_{c\bar{q}}(m_q)$ with optimal partitioning for every point on the curve. For sufficiently large m_q we will find the point where the eigenvalue curve $\lambda^{(m_q)}(M) = 1$ for $M < M_{max}$. We perform a fit to those points and evaluate it at the point $M_{c\bar{q}}^{(fit)}(m_q = m_u)$ to obtain the heavy-light meson mass at the physical point $M_{c\bar{u}}$, which is not accessible directly.

A second obstacle lies in the simultaneous description of light and charm quantities, which involves physics at different scales and is not trivial without further adjustment of our model parameters Λ and η, which we would like to avoid. Therefore, we use the typical value $\Lambda = 0.72$ GeV for the scale parameter, matched to reproduce the experimental value of the pion decay constant f_π, and $\eta = 1.8$, throughout all the calculations (including the tetraquarks) in this chapter. It is then however not possible to describe the D, D^*, D_s and D_s^* mesons correctly individually and we compromise in the following way: The charm quark mass m_c is determined by the condition that the sum $m_D + m_{D^*}$ equals the sum of the experimental masses [1]. The strange quark mass m_s is determined analogously for $m_{D_s} + m_{D_s^*}$. The results for $c\bar{q}, c\bar{c}, q\bar{q}$ 0^{-+} and 1^{--} states, as well as the scalar and axialvector diquarks are collected in table 1.6. We work in the isospin symmetric limit, where $m_u = m_d$ and the RL kernel applied in equation (1.27) is flavor independent. That leads to the light meson and diquark masses being independent of the flavor structure (for example $m_\rho = m_\omega = m_V$), as well as $m_{D^+} = m_{D^-} = m_{D^0}$ and so on.

	$m_{\bar{q}}$	m_{PS}	m_V	m_S	m_A
$q\bar{q}$	3.7	138(3)	732(1)	802(77)	999(60)
$c\bar{q}$	3.7	1802(2)	2068(16)	2532(90)	2572(8)
$c\bar{s}$	91	1911(3)	2169(14)	2627(82)	2666(7)
$c\bar{c}$	795	2792(6)	2980(6)	3382(15)	3423(8)

Table 1.6.: RL results for $q\bar{q}$, $c\bar{q}$, $c\bar{s}$ and $c\bar{c}$ meson and diquark masses (in MeV). $m_{\bar{q}}$ is the input current-quark mass The column m_{PS} contains the masses of π, D, D_s and η_c, the column m_V those of ρ/ω, D^*, D_s^* and J/ψ, and the columns m_S and m_A list the corresponding diquark masses. The errors quoted are obtained by varying $\eta = 1.8 \pm 0.2$.
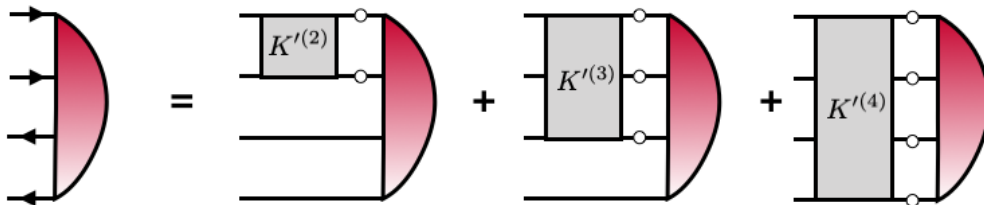

Figure 1.6.: The full four-body BSE is scatched. Half-circles and boxes represent the tetraquark amplitude and irreducible two, three and four-body interactions of the Bethe-Salpeter kernel, respectively. The white dots indicate dressed quark propagators.

1.4. Tetraquark BSE and amplitude

1.4.1. Tetraquark BSE

The full tetraquark kernel $K^{(4)}$ was defined in equation (1.22) and it contains irreducible two, three and four-body interactions as shown in figure 1.6. The equation we will solve in the following is obtained by keeping the two-body part $K'^{(2)}$ from (1.22) only, as previously done in [3]. This further approximation is made to reduce complexity. The non-inclusion of three-body forces is well justified in the baryon sector [80] and one could argue that the neglection of three and four-body forces in the tetraquark case is justified a posteriori considering the importance of the emerging two-body sub-clusters in [3].

In the following we will abbreviate the four-body Bethe-Salpeter amplitude $\Gamma = \Gamma^{(4)}$, the product of four dressed-quark propagators by $G_0 = G_0^{(4)}$ and $K' = K'^{(2)}$, where $K'^{(2)}$ was defined in equation (1.22) and stands for the irreducible two-body part of the full four-body kernel. The tetraquark BSE we work with is:
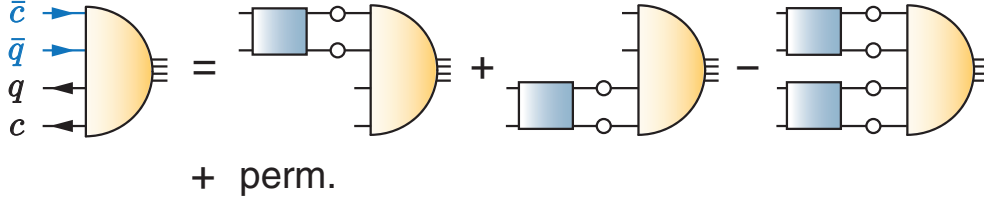
$$K'G_0\Gamma = \lambda\Gamma, \tag{1.31}$$

Figure 1.7.: Four-quark BSE for a $cq\bar{q}\bar{c}$ system in the $(12)(34)$ configuration; the remaining $(13)(24)$ and $(14)(23)$ permutations are not shown. The half-circles and boxes represent the tetraquark amplitude and Bethe-Salpeter kernel, respectively. White dots indicate dressed quark propagators. Figure published in [5].

where the eigenvalue of the $K'G_0$ operator appears after the application of the Nystrom method, see section A.2.2, analogous to the two-body BSE we discussed in the previous section. K' is given by:

$$K' = K'_{12,34} + K'_{13,24} + K'_{14,23} \tag{1.32}$$

$$K'_{a,a'} = K_a^{(2)}(G_0^{(2)})_{a'}^{-1} + K_{a'}^{(2)}(G_0^{(2)})_a^{-1} - K_a^{(2)}K_{a'}^{(2)}, \tag{1.33}$$

where a, a' denote qq, $\bar{q}\bar{q}$ or $q\bar{q}$ pairs. $K'^{(2)}_{13}$ for example stands for the rainbow-ladder (RL) truncated two-body kernel in equation (1.25) connecting quark one and antiquark three. The equation is given graphically in figure 1.7, where we show only $K'_{12,34}$. The equation can be rewritten as a Faddeev-Yakubovsky equation [104]. We use the explicit form of (1.32) to avoid overcounting and to ensure separability of the four-body correlation function obtained from one channel aa' only and thus the absence of residual color forces between widely separated clusters [84, 105, 106].

1.4.2. General tetraquark amplitude

Tetraquark amplitude and symmetries   Before solving the tetraquark BSE that we discussed in the last section, one needs to specify the quantum numbers and set up a basis for the tetraquark amplitude. The most general amplitude for a $J = 0$ ($J = 1$) tetraquarks is:

$$\Gamma^{(\mu)}(p,q,k,P) = \Gamma_D^{(\mu)}(p,q,k,P) \otimes \Gamma_C \otimes \Gamma_F, \tag{1.34}$$

where Γ_C, Γ_F and Γ_D stand for the color-, flavor-and Dirac parts, p, q, k and P for the relative-and the total momentum, respectively. The Dirac part

$$\Gamma_D^{(\mu)}(p,q,k,P) = \sum_{i=1}^{N} f_i(\Omega)\,\tau_i^{(\mu)}(p,q,k,P) \tag{1.35}$$

has dressing functions $f_i(\Omega)$ that depend on all Lorentz invariant combinations of the four-vectors p, q, k, P, which we abbreviate $\Omega = \{p^2, q^2, k^2, p \cdot q, p \cdot k, q \cdot k, p \cdot P, q \cdot P, k \cdot P\}$. N depends on the quantum numbers. $N = 768(48)$ for

1. Heavy-light tetraquarks

the axialvector and $N = 256(16)$ for the scalar tetraquark, where the number in parenthesis indicates the momentum-independent s-wave tensors. For more details on the partial-wave decomposition see the appendix B.1.3. $\tau_i^{(\mu)}$ are Dirac tensors and will be specified in the following.

A tetraquark amplitude has definite spin and parity, dictated by the underlying Poincare group structure. The relevant operator is the Pauli-Lubanski operator:

$$W^\mu = \frac{1}{2}\epsilon^{\mu\nu\alpha\beta}\hat{P}^\nu J^{\alpha\beta},$$

(1.36)

where the eigenvalue of W^2 is $j(j+1)$ and j is the total spin. Details for the similar case of the nucleon can be found in appendix 3 of [107]. The parity operators for the $J = 0$ and $J = 1$ tetraquarks are

$$\mathcal{P}(\tau_1 \otimes \tau_2)_{ab,cd} = (\gamma_4\tau_1 \otimes \gamma_4\tau_2)_{ab,cd}(\Lambda p_1, \Lambda p_2, \Lambda p_3, \Lambda p_4),$$
$$\mathcal{P}\,(\tau_1 \otimes \tau_2)^\mu_{ab,cd} = \Lambda^{\mu\nu}\,(\gamma_4\tau_1 \otimes \gamma_4\tau_2)^\nu_{ab,cd}\,(\Lambda p_1, \Lambda p_2, \Lambda p_3, \Lambda p_4),$$

(1.37)

respectively. $\Lambda = diag(-1,-1,-1,1)$, γ_4 is the Euclidean gamma matrix defined in section A.1, $(\tau_1 \otimes \tau_2)^{(\mu)}_{ab,cd}(p_1, p_2, p_3, p_4)$ is one of the tetraquark-basis elements $\tau_i^{(\mu)}(p, q, k, P)$ from equation (1.35) and $p_1...p_4$ are the momenta of quark 1...4. The relation between the quark momenta $p_1...p_4$ and the relative momenta p, q, k and the total momentum P will be given in equation (1.47).

Like for mesons and diquarks, there are two different symmetries for hidden and open-charm tetraquarks, respectively. Neutral hidden-charm tetraquarks have a definite charge conjugation quantum number. We abbreviate the charge-conjugation operator for hidden-charm tetraquarks with quark content $cu\bar{u}\bar{c}$, with $\mathcal{CC}$. Its action on a tetraquark amplitude Ψ, is

$$\mathcal{CC}\Psi^{abcd}_{\alpha\beta\gamma\delta}(p_1, p_2, p_3, p_4) = C_{\alpha\alpha\prime}C_{\beta\beta\prime}C_{\gamma\gamma\prime}C_{\delta\delta\prime}P_{14}P_{23}\,\Psi^{abcd}_{\alpha\prime\beta\prime\gamma\prime\delta\prime}(p_1, p_2, p_3, p_4)$$
$$= C_{\alpha\alpha\prime}C_{\beta\beta\prime}C_{\gamma\gamma\prime}C_{\delta\delta\prime}\Psi^{dcba}_{\delta\prime\gamma\prime\beta\prime\alpha\prime}(p_4, p_3, p_2, p_1),$$

(1.38)

where we denote Dirac indices with Greek letters and combine color-and flavor indices into the super indices a, b, c, d for better readability. P_{ij} stands for a permutation of all indices: color, Dirac, flavor and momentum. This is graphically a permutation of the quark legs. C is the charge conjugation matrix.

For open-charm tetraquarks with quark content $cc\bar{q}\bar{q}$, particles one and two are identical, as well as particles three and four. Therefore, Pauli symmetry has to be imposed on both identical-particle pairs:

$$P_{12}\Psi = P_{34}\Psi = -\Psi.$$

(1.39)

If one of the Pauli or charge-conjugation symmetries is present, all parts of the amplitude have a definite transformation property under this symmetry. The flavor quantum numbers depend on the symmetry group, which is SU(2) plus

	M_1	M_2	D
$(cq\bar{q}\bar{c})_{\alpha\beta\gamma\delta}$	$(c\bar{q})_{\alpha\gamma}(q\bar{c})_{\beta\delta}$	$(c\bar{c})_{\alpha\delta}(q\bar{q})_{\beta\delta}$	$(cq)_{\alpha\beta}(\bar{q}\bar{c})_{\gamma\delta}$
$(cc\bar{q}\bar{q})_{\alpha\beta\gamma\delta}$	$(c\bar{q})_{\alpha\gamma}(c\bar{q})_{\beta\delta}$	$(c\bar{q})_{\alpha\delta}(c\bar{q})_{\beta\delta}$	$(cc)_{\alpha\beta}(\bar{q}\bar{q})_{\gamma\delta}$

Table 1.7.: The different ways of pairing up the quarks to a tetraquark amplitude are shown. The indices $\alpha, \beta, \gamma, \delta$ in this case stand for Dirac, color and flavor space.

charm in our case. That introduces the isospin quantum number I. However, our tetraquark kernel is flavor blind. Therefore, the main purpose of the flavor part is to set the quark masses and dictate how the $\Gamma_D \otimes \Gamma_C$ part has to transform under Pauli and charge-conjugation symmetry. We will see that this will have important consequences for open-charm tetraquarks.

Dirac basis After we discussed the relevant symmetries we will now present explicit bases for the tetraquark amplitudes. For now we need a $J^P = 0^+$ and 1^+ Dirac basis. Throughout this work we restrict the Dirac part to s waves only, which requires a partial wave decomposition. We define:

$$\Lambda_\pm = \frac{\mathbb{1} \pm \not{n}_4}{2}, \qquad \Omega_\omega \otimes \Omega_{\omega'} \in \{\mathbb{1}, \epsilon\gamma_5\},$$

where n_4 is the normalized total momentum and $\epsilon \in \{-1, 1\}$ a contraction of transverse orthonormal four-vectors, defined in the references given in appendix B.1.3. Therewith the resulting basis for $J^P = 0^+$ can be cast into a compact form:

$$\tau_n(p, q, k, P) = \Gamma_j \, \Lambda_\lambda \, \Omega_\omega \, \gamma_5 C \otimes C^T \gamma_5 \, \Omega_{\omega'} \, \Lambda_{\lambda'} \, \Gamma_k. \tag{1.40}$$

It contains 256 elements from $\Gamma_j \in \{\mathbb{1}, \not{n}_2, \not{n}_3, \not{n}_4\}$, where $n_1...n_3$ are orthonormalized relative momenta, which are also defined in the references given in appendix B.1.3. In the following we restrict ourselves to s waves only. In that case, the remaining bases for $J^P = 0^+$ and $J^P = 1^+$ follow from the replacements:

$$0^+ : \ \Gamma_j \otimes \Gamma_k \in \{\mathbb{1} \otimes \mathbb{1}, \ \sqrt{1/3}\gamma_T^\mu \otimes \gamma_T^\mu\}, \tag{1.41}$$

$$1^+ : \ \Gamma_j \otimes \Gamma_k \in \{\gamma_\perp^\mu \otimes \mathbb{1}, \ \mathbb{1} \otimes \gamma_\perp^\mu, \ \epsilon\,\varepsilon^{\mu\alpha\beta\gamma}\,n_4^\gamma\,\gamma^\alpha \otimes \gamma^\beta\}, \tag{1.42}$$

where $\gamma_\perp^\mu = T_P^{\mu\nu}\gamma^\nu$ and $T_P^{\mu\nu}$ is the transverse-momentum projector with respect to the total momentum P of the tetraquark.

We are equipped with a basis for the tetraquark now, however, there are 3 possibilities of combining the two quarks and two antiquarks to a tetraquark tensors, that we call D, M_1 and M_2. We present them for the hidden and open-charm tetraquark in table 1.7.

Each way of combining quarks makes one of the three classes of diagrams of the kernel (1.32) look like a meson or diquark with two spectator quarks, which

1. Heavy-light tetraquarks

is desirable. We will call this the "home basis" of this class of diagrams and we choose the basis for $\tau^{(d)}_{\alpha\beta\gamma\delta}(p, q, k, P)$ in the decomposition $d \in \{D, M_1, M_2\}$ as follows:

$$
\begin{aligned}
D &: (\Gamma_j \, \Lambda_\lambda \, \Omega_\omega \, \gamma_5 C)_{\alpha\beta} (C^T \gamma_5 \, \Omega_{\omega'} \, \Lambda_{\lambda'} \, \Gamma_k)_{\gamma\delta}, \\
M_1 &: (\Gamma_j \, \Lambda_\lambda \, \Omega_\omega \, \gamma_5)_{\alpha\delta} (\gamma_5 \, \Omega_{\omega'} \, \Lambda_{\lambda'} \, \Gamma_k)_{\beta\delta}, \\
M_2 &: (\Gamma_j \, \Lambda_\lambda \, \Omega_\omega \, \gamma_5)_{\alpha\delta} \gamma_5 \, \Omega_{\omega'} \, \Lambda_{\lambda'} \, \Gamma_k)_{\beta\gamma},
\end{aligned}
\tag{1.43}
$$

with the replacements of (1.41) for the $J = 0$ tetraquark and the replacements of (1.42) for the $J = 1$ tetraquark. For the home bases of the "meson-like" diagrams we do not need the C matrices. We can transform between these bases via the Fierz transformations defined in the appendix B.1.4 and are free to use the basis that is most suitable for a given class of diagrams from equation (1.32).

With the home bases for D, M_1 and M_2 set up, our strategy for solving the tetraquark BSE will be the following: Calculate each of the 9 diagrams in (1.32) in its home basis, transform back to a common basis and add up the 9 diagrams in this common basis. We will come back to this in section 1.4.4.

Color basis   In terms of color we demand that the physical states form a color singlet, obtained from $\mathbf{3} \otimes \mathbf{3} \otimes \bar{\mathbf{3}} \otimes \bar{\mathbf{3}} = (\bar{\mathbf{3}} \oplus \mathbf{6}) \otimes (\mathbf{3} \oplus \bar{\mathbf{6}}) = \mathbf{1} \oplus \mathbf{1} \oplus \ldots$. In contrast to the meson case one gets two color singlets. They depend on the way of spanning the basis. In the diquark-antidiquark configuration one gets the singlets from $\bar{\mathbf{3}} \otimes \mathbf{3}$ and $\mathbf{6} \otimes \bar{\mathbf{6}}$, whereas in the meson-meson decompositions they follow from: $\mathbf{1} \otimes \mathbf{1}$ and $\mathbf{8} \otimes \mathbf{8}$. The color bases in M_1, M_2, D are given by $\{\mathcal{C}_{11}, \mathcal{C}_{88}\}$, $\{\mathcal{C}'_{11}, \mathcal{C}'_{88}\}$, $\{\mathcal{C}_{\bar{3}3}, \mathcal{C}_{6\bar{6}}\}$, where

$$
(\mathcal{C}_{11})_{ABCD} = \frac{1}{3} \, \delta_{AC} \, \delta_{BD}, \qquad (\mathcal{C}'_{11})_{ABCD} = \frac{1}{3} \, \delta_{AD} \, \delta_{BC}
\tag{1.44}
$$

and the other singlets are related to them by Fierz transformations:

$$
\mathcal{C}_{\bar{3}3} = -\frac{\sqrt{3}}{2} \, (\mathcal{C}_{11} - \mathcal{C}'_{11}), \qquad \mathcal{C}_{6\bar{6}} = \sqrt{\frac{3}{8}} \, (\mathcal{C}_{11} + \mathcal{C}'_{11}),
\tag{1.45}
$$

$$
\mathcal{C}_{88} = \frac{\mathcal{C}_{11} - 3\,\mathcal{C}'_{11}}{2\sqrt{2}}, \qquad \mathcal{C}'_{88} = \frac{\mathcal{C}'_{11} - 3\,\mathcal{C}_{11}}{2\sqrt{2}}.
\tag{1.46}
$$

The relevant color traces for our calculations are given in appendix B.1.2.

Momenta and partitioning   As we have seen, the tetraquark amplitude of equation (1.34) depends on four momenta $p_1...p_4$, one for each (anti-) quark. It is convenient to work with three relative momenta and the total momentum instead:

$$p = \frac{p_{23} - p_{14}}{2} + \left(\frac{1}{2} - \sigma_{14}\right) P, \quad k = \frac{p_{12} - p_{34}}{2} + \left(\frac{1}{2} - \sigma_{34}\right) P,$$

$$q = \frac{p_{13} - p_{24}}{2} + \left(\frac{1}{2} - \sigma_{24}\right) P, \quad P = \sum_i p_i. \tag{1.47}$$

Above we introduced the shorthand $x_{ij} = x_i + x_j$. We have introduced momentum partitioning parameters σ_i for each quark and antiquark momentum. If the full basis is included, the result should be independent of the choice of partitioning parameters. Note that they sum to unity: $\sum_i^4 \sigma_i = 1$. The parameters will be useful for heavy-light calculations since that shifts the probed parabolas that are sampled by the quarks in the complex plane and can therefore allow one to go to higher bound state masses, just as in the meson case we showed in figure 1.5. We will also use it to avoid the singularities introduced by intermediate meson-meson and diquark-antidiquark poles.

The shorthand notation p_{ij} makes the meaning of the relative momenta quite clear. For example q is the relative momentum between the two meson subclusters (13) and (24). P is the total momentum of the tetraquark amplitude. The inverse mapping reads:

$$p_1 = \frac{k + q - p}{2} + \sigma_1 P, \quad p_3 = \frac{-k + q + p}{2} + \sigma_3 P,$$

$$p_2 = \frac{k - q + p}{2} + \sigma_2 P, \quad p_4 = \frac{-k - q - p}{2} + \sigma_4 P \tag{1.48}$$

and we choose the four-vectors to be:

$$P = \sqrt{P^2} \begin{pmatrix} 0 \\ 0 \\ 0 \\ 1 \end{pmatrix}, \quad k = \sqrt{k^2} \begin{pmatrix} 0 \\ 0 \\ \bar{z}_k \\ z_k \end{pmatrix}, \quad q = \sqrt{q^2} \begin{pmatrix} \sin(\alpha)\bar{y}_q\bar{z}_q \\ \cos(\alpha)\bar{y}_q\bar{z}_q \\ \bar{z}_q y_q \\ z_q \end{pmatrix}, \quad p = \sqrt{p^2} \begin{pmatrix} 0 \\ \bar{y}_p\bar{z}_p \\ \bar{z}_p y_p \\ z_p \end{pmatrix},$$

$$\tag{1.49}$$

where we again used $\bar{a} = \sqrt{1 - a^2}$, $z_i, y_i \in [-1, 1], \alpha \in [0, 2\pi]$. P is chosen to be in the rest frame which is equivalent to having only a fourth component. We introduced six angles and four length variables, which correspond to the ten Lorentz invariants we need to describe the set Ω that the dressing functions depend on. For given P^2 the nine remaining ones are:

$$\Omega = \{p^2, q^2, k^2, p \cdot q, p \cdot k, q \cdot k, p \cdot P, q \cdot P, k \cdot P\} \tag{1.50}$$
$$= \{p^2, q^2, k^2, \omega_3, \omega_2, \omega_1, \eta_1, \eta_2, \eta_3\}.$$

Since one needs to setup a grid in all these variables, the solution of the full tetraquark amplitude is a numerically extremely demanding task. A strategy

to simplify the system without the loss of information is to introduce variables, which form multiplets of the permutation group S_4 [108]. One obtains a singlet, a doublet and two triplets:

$$S_0 \equiv \frac{p^2 + q^2 + k^2}{4}, \quad D_0 \equiv S_0 \begin{pmatrix} a \\ s \end{pmatrix}, \quad T_0 \equiv S_0 \begin{pmatrix} u \\ v \\ w \end{pmatrix} \quad T_1 \equiv \sqrt{S_0 P^2} \begin{pmatrix} u' \\ v' \\ w' \end{pmatrix},$$

$$\text{(1.51)}$$

where the entries of the multiplet vectors are:

$$a = \sqrt{3}\frac{q^2 - p^2}{4S_0}, \qquad s = \frac{p^2 + q^2 + k^2}{4S_0}, \qquad \text{(1.52)}$$

$$u = -\frac{\omega_1 + \omega_2 + \omega_3}{4S_0}, \qquad v = -\sqrt{2}\frac{\omega_1 + \omega_2 - 2\omega_3}{4S_0}, \qquad \omega = \sqrt{6}\frac{\omega_1 - \omega_2}{4S_0},$$

$$u' = -\frac{\eta_1 + \eta_2 + \eta_3}{\sqrt{12S_0 P^2}}, \qquad v' = -\frac{\eta_1 + \eta_2 - 2\eta_3}{\sqrt{24S_0 P^2}}, \qquad \omega' = \frac{\eta_1 - \eta_2}{\sqrt{8S_0 P^2}}.$$

An advantage of these variables is that a multiplet transforms only into itself under S_4 transformations, which also encodes the Pauli and charge-conjugation symmetry we discussed earlier. The amplitudes in (1.34) can then be written as $f_i(S_0, D, T_0, T_1)$, consequently one can switch off groups of variables without destroying these symmetries.

Using S_4 variables it was found in [3] that the scalar tetraquarks depend mainly on S_0 and D. When retaining S_0 only, the mass of the σ was found to be roughly 1500 MeV. When the doublet variables were allowed to dynamically contribute also, the four-quark BSE dynamically generates meson-meson and diquark-antidiquark poles in the $f_i(S_0, D)$ in all the D, M_1, M_2 topologies. Since one needs to integrate over the dressing functions this effectively introduces decay thresholds, which is a mechanism that ensures the tetraquark to be a resonance, which is naturally built into equation (1.31). These dynamically generated intermediate pion poles bring the mass down from 1500 to $400 - 500$ MeV.

Solution with the general tetraquark amplitude   In principle, one can go on and solve the tetraquark BSE from here. Details of the solution algorithm are described in [109]. However, the method introduces some obstacles:

- the number of grid points necessary for the nine-dimensional dressing functions $f_i(\Omega)$ is huge,

- complications arise due to the dynamically generated two-body poles in the f_i,

- poles appear in the integration domain as soon as $M > 2m_\pi$ or whatever the lowest-lying threshold is. Therefore, one can obtain the eigenvalue curve $\lambda(M)$ of equation (1.31) only for $M < 2m_\pi$ on the real axis.

In addition, we would like to identify physical components in the tetraquark amplitude to understand their contributions, as we laid out in the introduction.

1.4.3. Physical tetraquark amplitude

The idea of this section is now to anticipate the dynamically generated two-body poles and approximate the dressing functions by a residue that depends only on S_0 times a product of those two-body poles:

$$f(S_0, D, T_0, T_1) \rightarrow f(S_0)P_1P_2,$$

where the two-body poles P_1 and P_2 depend on S_0, D and the respective pole masses m_1 and m_2. This approximation will not allow other poles to be dynamically generated in the remaining residue $f(S_0)$, because a pole term would depend on the doublet variables a and s from equation (1.51) and the residue does not depend on them anymore. On the other hand, the findings of [3] provide confidence, that the equation would produce these poles dynamically anyway and that important physics should be governed by our ansatz.

The remaining question is which poles will appear in which tensor structures of the tetraquark amplitude. It can be answered by solving the relevant meson and diquark BSEs. For example, a pion will have poles in the $\gamma^5_{\alpha\beta} \otimes \mathbb{1}_{AB}$ component (and the three other components from table 1.5). Therefore, a $\pi \otimes \pi$ component in the tetraquark would have a pole in $(\gamma^5 \otimes \gamma^5)_{\alpha\gamma,\beta\delta} \otimes (\mathbb{1} \otimes \mathbb{1})_{AC,BD}$ component and the pole would be $P(m_\pi, m_\pi)_{13,24}$, with

$$P(m_1, m_2)_{ab,cd} = \frac{1}{(p_a + p_b)^2 + m_1^2} \frac{1}{(p_c + p_d)^2 + m_2^2} \qquad (1.53)$$

for a $q_{\alpha,A}q_{\beta,B}\bar{q}_{\gamma,C}\bar{q}_{\delta,D}$ tetraquark. Note also that the pole appears in the total momenta of the quark-antiquark pairs. Since we thereby assume that this pole-residue structure captures the relevant momentum dependences of the dressing functions, we have the freedom to choose the external grid in the variables on which the dressing functions do not depend on. To do so, we choose

$$\{k^\mu, p^\mu, q^\mu\} = \frac{2\S_0}{\sqrt{3}} \{e_1^\mu, e_2^\mu, e_3^\mu\}, \quad P^\mu = iM\,e_4^\mu, \qquad (e_i)^\mu = \delta_{i\mu}. \qquad (1.54)$$

This simplifies the system and reduces the computational effort while preserving the structure of the otherwise dynamically generated intermediate particle poles, which produce the decay channels and the resonance structure of the states we investigate. Once again, our goal here is to mimic the behavior of the full equation as good as we can by putting in only those terms that would arise dynamically based on the findings in [109].

There are now two types of tetraquarks we want to describe:

- The hidden-charm tetraquarks ($cq\bar{q}\bar{c}$) obey charge-conjugation symmetry. They contain heavy-light diquark and antidiquark, HLM and HC components.

1. Heavy-light tetraquarks

- The open-charm tetraquarks $cc\bar{q}\bar{q}$, by contrast, are Pauli-symmetric in both, the quark and the antiquark pair. They carry a different diquark-antidiquark component, that is made out of a heavy-heavy diquark and a light-light antidiquark. Furthermore, they contain HLM components. A separate HC component is not possible anymore, since there is no $\bar{c}$ and no q quark present.

Flavor basis for open and hidden-charm tetraquarks   The flavor structures for hidden-charm tetraquarks are constructed from pairing a light quark with a light antiquark $SU(2) \otimes SU(2) = 1 \oplus 3$ resulting in $\{u\bar{u} - d\bar{d}, u\bar{d}, d\bar{u}\}$ and $u\bar{u} + d\bar{d}$. These are the usual "mesonic" isospin multiplets.

Similarly for the open-charm tetraquarks and $SU(2) \otimes SU(2)$ provides $\{\bar{u}\bar{d} + \bar{d}\bar{u}\}, \bar{u}\bar{u}, \bar{d}\bar{d}$ and an isosinglet $\bar{u}\bar{d} - \bar{d}\bar{u}$. The charges for these open-charm tetraquarks are: $(+,0,++)$ for the $I = 1$ and $(+)$ for the $I = 0$ states, respectively. Although the $cc\bar{u}\bar{u}$ has charge zero it does not fulfill charge conjugation symmetry because of the charm quantum number. The flavor amplitudes for isospin $I = 0$ and $I = 1$ tetraquarks, are:

$$\mathcal{F}_0 = \frac{1}{\sqrt{2}}(u\bar{u} + d\bar{d})\bar{c}, \qquad \mathcal{F}_1 = \left\{ \begin{array}{c} u\bar{d} \\ \frac{1}{\sqrt{2}}c(u\bar{u} - d\bar{d})\bar{c} \\ d\bar{u} \end{array} \right\}, \qquad (1.55)$$

$$\tilde{\mathcal{F}}_0 = \frac{1}{\sqrt{2}}cc[\bar{u}, \bar{d}], \qquad \tilde{\mathcal{F}}_1 = \left\{ \begin{array}{c} \bar{d}\bar{d} \\ \frac{1}{\sqrt{2}}cc\{\bar{u}, \bar{d}\} \\ \bar{u}\bar{u} \end{array} \right\}, \qquad (1.56)$$

where the tilde marks the open-charm tetraquarks and $[.., ..], \{.., ..\}$ denote antisymmetrization and symmetrization, respectively.

Dirac and color basis expansion: meson-meson and diquark-antidiquark   In practice, we systematically write down all possible terms in an amplitude with quantum numbers J^{PC} given our pole residue structure. Furthermore, we only include the lightest intermediate meson and diquark terms from the RL spectrum with their leading tensor structure, because they will have the highest impact on the tetraquark mass. Those are the pseudoscalar and vector mesons (in both meson channels) and we will build up the tetraquark meson-meson parts from combinations of those. The lightest diquark-antidiquark components are scalar and axialvector diquarks. We discussed the calculation of heavy-light meson and diquark states in section 1.3.3 and their masses are given in table 1.6. Now we proceed in the following way:

1) Write down all possible combinations. The terms that arise when the leading components of pseudoscalar and vector mesons (scalar-and axialvector diquarks) are coupled are collected in table 1.8. Take for example the 0^+ tetraquark term built from pseudoscalar-pseudoscalar mesons. The leading pseudoscalar structure is γ^5. Consequently we get $\gamma^5 \otimes \gamma^5$ as the leading tetraquark structure.

J^P		meson-meson	diquark-antidiquark	
0^+	ps-ps	$\gamma^5 \otimes \gamma^5$	sc-sc	$\gamma^5 C \otimes C^T \gamma^5$
0^+	v-v	$\gamma_\perp^\mu \otimes \gamma_\perp^\mu$	ax-ax	$\gamma_\perp^\mu C \otimes C^T \gamma_\perp^\mu$
1^+	ps-v	$\gamma^5 \otimes \gamma_\perp^\mu$	sc-ax	$\gamma^5 C \otimes C^T \gamma_\perp^\mu$
1^+	v-v	$\gamma_\perp^\mu \otimes \gamma_\perp^\nu \hat{P}^\sigma \epsilon^{\mu\nu\rho\sigma}$	ax-ax	$\gamma_\perp^\mu C \otimes C^T \gamma_\perp^\nu \hat{P}^\sigma \epsilon^{\mu\nu\rho\sigma}$

Table 1.8.: Collection of possible elements in the tetraquark amplitude in each channel.

2) For a given $J^{P(C)}$ we take all meson-meson components in the M_1 and M_2 decomposition from the table and all diquark-antidiquark components that can combine to the given spin. If we for example describe a 0^{++} tetraquark we take the first two rows into account. We include the meson terms in both M_1 and M_2 which for the ps-ps would be: $\gamma_{\alpha\gamma}^5 \gamma_{\beta\delta}^5$ and $\gamma_{\alpha\delta}^5 \gamma_{\beta\gamma}^5$.

3) We symmetrize the Dirac part to have the correct symmetry under charge conjugation (or Pauli symmetry for the open-charm tetraquarks). Because the symmetry properties of the flavor-and color part, as well as those of the dressing functions are fixed, we know for a given state what symmetry we have to impose on the Dirac part. For our 0^{++} example the flavor structure $\mathcal{F}_0$ (isospin zero) has positive charge conjugation symmetry, as does the dressing function $f(S_0)$. That means the combination of Dirac-and color part needs positive charge conjugation. In the M_1 channel, for example, the color structure $\mathcal{C}_{11}$ has positive charge conjugation which requires positive charge conjugation for the Dirac part. We generally achieve this by symmetrising the tensor structure with the operator $\mathbb{1} + \mathcal{CC}$. It is not necessary in our example, but we can nevertheless apply the operator:

$$(\mathbb{1} + \mathcal{CC}) \, \gamma_{\alpha\delta}^5 \gamma_{\beta\gamma}^5 = 2\gamma_{\alpha\delta}^5 \gamma_{\beta\gamma}^5.$$

The charge conjugation operator above was defined in equation (1.38).

4) Now each structure comes with the product of two-body poles in this channel just as we discussed in the example. Thus, we multiply each tensor structure with the correct pole of equation (1.53) with the pole mass we calculated from the two-body equation (1.27). The relevant pole masses are collected in table 1.6. The parameters of the Maris-Tandy model we introduced in equation (1.23) are $\Lambda = 0.72$ GeV and $\eta = 1.8 \pm 0.2$. We work in the isospin symmetric limit. Therefore, for example $m_{D^+} = m_{D^-} = m_{D^0} = 1802$ MeV. The charm quark mass is fixed by $m_D + m_{D^*} = 3870$ MeV, which is the sum of their experimental masses [1]. The strange quark mass is likewise fixed from $m_{D_s} + m_{D_s^*} = 4080$ MeV.

In our example the pole would be: $P(m_{ps}, m_{ps})_{13,24}$. We end up with the pseudoscalar-pseudoscalar tensor structure in the M_1 decomposition:

$$2\gamma^5_{\alpha\delta}\gamma^5_{\beta\gamma}P(m_{ps}, m_{ps})_{13,24}\mathcal{C}_{11}\mathcal{F}_0 f(S_0).$$

We now go on and do this for all the other couplings within the M_1 decomposition and afterwards for all couplings in M_2 and D. It is not possible to symmetrize every structure for every quantum number. A $D^*\bar{D}^*$ component for example is possible in the 1^{+-} but not in the 1^{++} channel, because of the symmetry constraints. We thereby obtain an amplitude for every quantum number we are interested in, that we call Γ_{phys}. The resulting amplitudes are collected in "human-readable" form in table 1.9 and in full glory in the appendix B.2. A detailed derivation can be found in the appendix of [6].

Note that this is just a different way of spanning the basis compared to the general amplitude we used in equation (1.34). If one added enough components, the full basis would be retrieved. When we solve the tetraquark BSE, we project Γ_{phys} onto the s-wave basis we selected in the previous chapter in equations (1.41) and (1.42).

1.4.4. Solution technique of the four-body equation

Calculating eigenvalue curves from the BSE   We solve the four-body equation (1.31) in the RL truncation as an eigenvalue problem as described in section 1.3. As a result we obtain the eigenvalue curve $\lambda(M)$ as we have already demonstrated for the two-body case in figure 1.4.

Firstly, we fix the index ordering of all tensor structures of Γ_{phys} that is given for the different quantum numbers in table B.2, to a common one. That can be done by the Fierz transformations given in appendix B.1.4. Which ordering we pick ($\alpha\beta\gamma\delta$ for example) does not matter, the result will be independent of that choice. Afterwards we project Γ_{phys} onto the s-wave basis given in equation (1.41) and (1.42), project on the dressing functions and use Feyncalc [110] to precalculate the traces that are necessary to set up the kernel matrix. To solve the eigenvalue problem

$$K_{ij}(M)\Gamma_j = \lambda(M)\Gamma_j,$$

where i and j are super indices, we use an iterative Krylov Schur solver which is implemented in the SLEPc library [111][3] in a highly efficient and user friendly manner. It is necessary to use improved algorithms compared to the simple power iteration for instance, which will not converge in the tetraquark case. Now we can calculate the eigenvalue curve $\lambda(M)$ as a function of the tetraquark mass.

Unfortunately, just as in prior tetraquark calculations of [3, 84] the range of M is limited. M appears in all four-quark propagators as well as all intermediate meson-meson and diquark-antidiquark poles that are part of our physical

---

[3]One constructs the action of the kernel matrix on the amplitude $\Gamma^n_j \to \Gamma^{(n+1)}_j$. That means the matrix never has to be constructed explicitly. We use spline interpolation from alglib for the necessary interpolation in the S_0 variable [112].

	$I(J^{PC})$	HLM	HC	DI
$cq\bar{q}\bar{c}$	$0(0^{++})$	$DD,\ D^*D^*$	$J/\Psi\omega,\eta_c\eta$	$SS,\ AA$
	$1(0^{++})$	$D\bar{D},\ D^*\bar{D}^*$	$J/\Psi\rho,\eta_c\pi$	$SS,\ AA$
	$0(1^{++})$	$D\bar{D}^* - D^*\bar{D}$	$J/\Psi\omega$	$SA - AS$
	$1(1^{++})$	$D\bar{D}^* - D^*\bar{D}$	$J/\Psi\rho$	$SA - AS$
	$0(1^{+-})$	$D\bar{D}^* + D^*\bar{D},\ D^*\bar{D}^*$	$J/\Psi\eta,\eta_c\omega$	$SA + AS, AA$
	$1(1^{+-})$	$D\bar{D}^* + D^*\bar{D},\ D^*\bar{D}^*$	$J/\Psi\pi,\eta_c\rho$	$SA + AS, AA$

	$I(J^{P})$	HLM	DI
$cc\bar{q}\bar{q}$	$0(0^{+})$	-	-
	$1(0^{+})$	$DD,\ D^*D^*$	AA
	$0(1^{+})$	$DD^* - D^*D,\ D^*D^*$	AS
	$1(1^{+})$	$DD^* + D^*D$	AA

Table 1.9.: *$cq\bar{q}\bar{c}$* and *$cc\bar{q}\bar{q}$* amplitudes and their physical content, where for the *$cq\bar{q}\bar{c}$* states $D\bar{D} = D^0\bar{D}^0 \pm D^+D^-$ (and analogously for $D^*\bar{D}^*$ and $D\bar{D}^*$) with "+" for the $I = 0$ state and "−" for the $I = 1$ states. For the *$cc\bar{q}\bar{q}$* states $DD = D^0D^0 \pm D^+D^-$ (and analogously for D^*D^* and DD^*) with "−" for the $I = 0$ state and "+" for the $I = 1$ states. The difference between open and hidden-charm tetraquarks is due to their different flavor tensors, that were given in equation (1.55): $\mathcal{F}_{0,1}$ for the *$cq\bar{q}\bar{c}$* $I = 0, 1$ states, and $\tilde{\mathcal{F}}_{0,1}$ for the $I = 0, 1$ *$cc\bar{q}\bar{q}$* states, respectively. The full amplitudes in mathematical form are given in section B.1.1 in the appendix.

amplitude. That poses a set of conditions that depend on the intermediate states, M and the partitioning parameters. An example for a system with only one meson-meson threshold in the M_1 channel, is:

$$M < \frac{M_c}{2\sigma_1}, \qquad M < \frac{M_q}{2\sigma_2}, \qquad M < \frac{M_q}{2\sigma_3}, \qquad M < \frac{M_c}{2(1 - \sum_i^3 \sigma_i)},$$
$$M < \frac{m_{13}}{\sigma_{13}}, \qquad M < \frac{m_{24}}{\sigma_{24}}, \tag{1.57}$$

where we used $\sigma_{ij} = \sigma_i + \sigma_j$. M_q and M_c are the light and charm-quark masses that describe the apex of the parabola in figure 1.5.

For equal quark masses the optimal choice of the partitioning parameters is $\sigma_i = 1/4$. Since we do not have four equal quark masses in the system, we are looking for a new optimal partitioning. Given all the thresholds, one can formulate conditions for the quark poles and for the intermediate meson poles and optimize the set of equations with respect to $\sigma_1, \sigma_2, \sigma_3$ to obtain M_{max}.

Usually it is sufficient to introduce just one partitioning parameter $\zeta = \frac{1}{2} - \sigma_1 = \sigma_2 = \sigma_3$ to reach M_{max}. In that case we can interpret ζ as the fraction of the complex momentum P from equation (1.49) that goes through the light quarks, while $1 - \zeta$ is the fraction going through the charm quarks. In that case the solution might generally be non-unique. We use the resulting plateau of $M_{max}(\zeta)$ to estimate the error from the momentum partitioning in section 1.5.

Whenever the tetraquark mass $M_{tetra} < M_{max}$ we explicitly find the point where the eigenvalue curve crosses one: $\lambda(M_{tetra}) = 1$. If that is not the case we need to extrapolate the eigenvalue curve to the point where $\lambda(M) = 1$. For consistency we always use a quadratic fit wherever the eigenvalue curve cannot be obtained at the physical point, consult figure B.1 in the appendix for an example. The extrapolation range can potentially be large, depending on how low the lowest threshold is. We are aware that naive extrapolation over decay thresholds is dangerous [113] and we try to minimize the extrapolation dependence with the procedure described in the following.

Evaluating the eigenvalue curves If we find a bound state at the physical point, as for the hidden-charm scalar for example, we do not need any kind of fitting[4]. For all other cases we extrapolate down the quark mass curve $M_{tetra}(m_q)$. We start from the point $M_{c\bar{c}\bar{c}}$ where we usually find a bound state pole, and go down in m_q until the eigenvalue curve $\lambda^{(m_q)}(M)$ does not hit $\lambda^{(m_q)}(M) = 1$ for $M \leq M_{max}$ anymore. Then we apply a linear fit to these points[5] and evaluate the fit at the light-quark mass to obtain the physical result[6].

---

[4]Since the error when varying the partitioning parameter is large and we prefer a consistent approach to all channels, we still apply the method described here as well as the direct calculation

[5]If for a given m_q we need to extrapolate only a short distance we include these points as well.

[6] m_q can directly be related to m_π and thereby our procedure is very similar to the one sometimes applied for lattice calculations at unphysical pion masses.

For the whole mass curve we use the amplitudes given in table 1.9, which means we do not change the symmetry for the all-charm state for example. That is why $M_{cc\bar{c}\bar{c}}$ does not coincide with the mass of the physical all charm $cc\bar{c}\bar{c}$ tetraquark that would require a different symmetrization of the amplitude, namely charge conjugation in the $(13)(24)$ and $(14)(23)$ quark pairs, as well as Pauli symmetry in both the quark and antiquark pairs. The hidden-strange partner can, however, be read off from the curve if the underlying symmetry for the light and strange tetraquark is the same, which it is for the $I = 0$ hidden-charm tetraquarks. Naturally, this does not work for the $I = 1$ tetraquarks, since there are no light quarks in the $cs\bar{s}\bar{c}$ and $cc\bar{s}\bar{s}$ amplitude, respectively, and therefore the isospin has to be $I = 0$.

A peculiar thing happens for the open-charm open-strange tetraquarks: Due to the symmetry constraints we can read off the open strange $0(1^+)$ and $0(0^+)$ from the quark mass curves of the $1(1^+)$ and $1(0^+)$ states. One can easily verify this by looking at the flavor tensors in equation (1.55) and replacing the light quarks u, d with two strange qaurks. This leads to a mass gap, as we will discuss in the next section.

1.4.5. Influence on the spectrum

Since our interaction kernel of equation (1.32) is flavor blind, the flavor tensor traces out completely. The only purpose of the flavor part here is dictating the symmetry of the color times Dirac part of the tetraquark amplitude. As can be seen in table 1.9, for hidden-charm tetraquarks, we have exactly the same content for both isospins. The only difference lies in the M_2 channel, which is the HC channel in this case. For isospin one we need to replace $\omega \to \rho$ and $\eta \to \pi$. However, since the RL kernel does not know about the $U(1)$ anomaly, all pseudoscalar mesons are treated in the same manner and π and η have the same mass. The same is true for ρ and ω, see table 1.6. This means that the hidden-charm tetraquarks with isospin $I = 0$ and $I = 1$ are degenerate. Consequently every state in our hidden-charm spectrum appears with multiplicity four, which means we should find two neutral and two charged states with charges $+, -$. Again, this is a consequence of the applied RL truncation in combination with the approximated amplitude, and might not be a general feature. Furthermore, electromagnetic isospin effects will also lift the degeneracy [114], however, they are not considered here.

The situation is different in the open-charm sector: Comparing the $0(1^+)$ and $1(1^+)$ states, we see that there are different signs between the DD^* terms and there is also an additional D^*D^* component present in the $I = 0$ case. Furthermore, different diquarks need to be considered: In the former we have a light-scalar antidiquark and a light-axialvector antidiquark in the latter case. That is due to the different transformation properties of the flavor tensors $\tilde{\mathcal{F}}_{0,1}$ from equation (1.55) under Pauli transformations. While one is odd, the other is even in the light quarks and therefore needs a different diquark tensor structure. The situation is even more dramatic for the $0(0^+)$ state, where we cannot construct a single component starting with the tensors from table 1.8.

1.4.6. Further approximations

We have systematically constructed the physical amplitudes for the tetraquark in the previous section and arrived at the physical content listed in 1.9. We drop the $\eta_c\{\eta, \pi\}$ component in the $(0/1)0^{++}$ and the $\eta_c\{\rho, \omega\}$ components in the 1^{+-} channel for now. We do this for two reasons: Firstly the decay modes are not seen in experiment, even though they have been searched for [115] and secondly, the RL description of the η is unrealistic[7]. Furthermore, we neglect the AA component that should be present in the 1^{+-} state by construction. This is by far the highest threshold in the system and in all hidden-charm channels we found the diquarks to be subleading.

---

[7]Due to the missing $U(1)$ anomaly in our framework π and η have the same mass, which is not realistic. Therefore, we cannot provide a realistic η mass $M_\eta(m_q)$ from a two-body calculation which we would need for the tetraquark calculation.
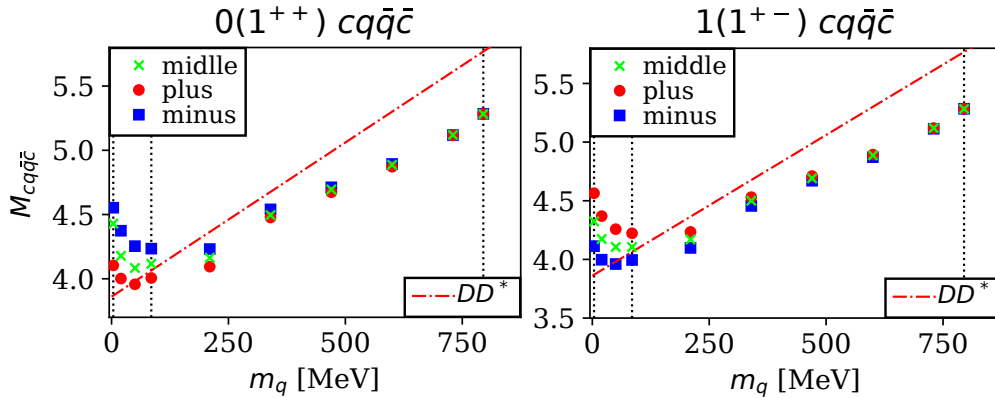
Figure 1.8.: left/right: $0(1^{++})/1(1^{+-})$ variation of the partitioning parameter away from its optimum in the symmetric limit.

m_q [MeV]	3.7	20	50	85	210	340	470	600	730	795
$\frac{\Delta M}{M}$ [%]	4.4	7.0	10.4	5.5	5.1	1.9	1.8	0.2	0.1	0.01
$\frac{\Delta M}{M}$ [%]	10.8	11.0	12.7	8.0	5.6	1.9	2.1	0.2	0.2	0.1

Table 1.10.: Error estimates from the momentum partitioning for one parameter ζ (row 1) and without restricting the σ_i (row 2). We show the results for the $0(1^{++})$ state, all other states can be found in section B.1.6 in the appendix.

1.5. Results

1.5.1. Error estimates

There is a systematic error that we cannot quantify when we introduce our truncation of the quark DSE and the BSE kernel. However, within this approximation of QCD we can try to quantify errors. Here we only look at the error introduced by the momentum partitioning and its effect on our results.

As discussed, we try to minimize the extrapolation error by choosing optimal partitioning parameters that were introduced in equation (1.48). We simplify the situation by choosing $1/2 - \sigma_1 = \sigma_3 = \sigma_2 = \zeta$, which means the light quark and antiquark get the same fraction of the momentum P and so do the heavy quark and antiquark. This leaves one parameter that quantifies the portion of P that is assigned to the light-light and the heavy-heavy quark-antiquark pair, respectively. We call this the symmetric limit. The optimal ζ is not unique in that case. Therefore, we vary it around its optimal value $\zeta_{opt} \pm 0.02$. We show an example for the $0(1^{++})$ and $1(1^{+-})$ HLM-only calculation in figure 1.8.

One can clearly see that the error gets much larger the bigger the mass difference of the light-quark mass compared to the charm-quark mass gets. From the variation around the optimal parameter we obtain an error estimate, which is shown for the $0(1^{++})$ case in the first row of table 1.10. The errors

$I(J^{P(C)})$	$cq\bar{q}\bar{c}$	exp. candidate	$cs\bar{s}\bar{c}$	candidate
$0/1(0^{++})$	3195(107) 3503(422)	$X(3915)$ / ?	3362(95) 3592(295)	?
$0/1(1^{++})$	3916(74)	$X(3872)$ / ?	4068(61)	$X(4140)$
$0/1(1^{+-})$	3741(91)	? / $Z(3900)$	3892(81)	?
	$cc\bar{q}\bar{q}$		$cc\bar{s}\bar{s}$	
$0(0^{+})$	-		3951(?)	
$1(0^{+})$	3795(?)		-	
$0(1^{+})$	3899(82)		4360(387)	
$1(1^{+})$	4216(440)		-	

Table 1.11.: Results of our calculations and experimental candidates are shown, "-" means we do not have a state in this channel. The two results for the hidden-charm scalar stem from the two different methods we used to calculate it: a fit of $M(m_q)$ and direct calculation via $\lambda(M) = 1$. The $cs\bar{s}\bar{c}$ states in the upper right corner of the table naturally carry isospin $I = 0$, since no light quarks are present.

from going away from the symmetric limit were obtained by comparison of the symmetric calculations and the difference to another set of optimal parameters obtained by optimizing for maximum P^2 without restricting the σ_i. The results are shown in the second row of the error table. In contrast to the symmetric case, the variation can be quite strong for the points for bigger m_q as well. However, we only use the "unrestricted" optimization if it is necessary because we cannot reach M_{max} in the symmetric limit.

For the results at the physical point we calculate a confidence band to the fit that we apply to $M_{tetra}(m_q)$ to extract $M_{tetra}(m_u)$ at the physical point. The errors that go into that fit are the ones in the second row of the error table. The error from this confidence band at m_q is given in table 1.11.

1.5.2. The spectrum

The situation is summarized in table 1.11. As discussed before we already know that we find four degenerate states coming from isosinglet and isotriplet in all hidden-charm channels, namely the $0^{++}, 1^{++}, 1^{+-}$ and for each channel one hidden-strange partner with a higher mass. For the open-charm channels this degeneracy is lifted because of the different relative signs and components of the $0(1^{+})$ and $1(1^{+})$ states, as shown in table 1.9. Again the $(0)1^{+}$ state comes with a hidden-strange partner. In the 0^{+} channel we find a ground state only for isospin one, since we cannot construct an appropriately symmetrized state

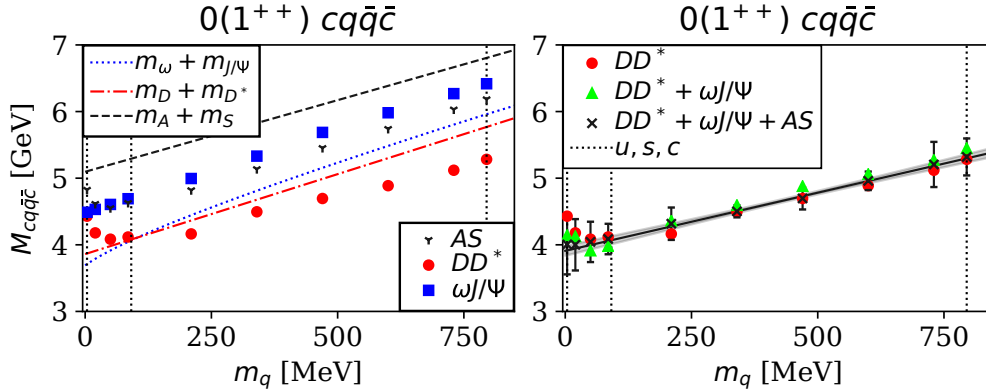Figure 1.9.: Mass of the $I(J^{PC}) = 0(1^{++})$ four-quark state as a function of the current-quark mass. Left: Solutions for the individual $D\bar{D}^*$, $J/\psi\,\omega$ and diquark-antidiquark components together with their respective thresholds. Right: results obtained from including one ($D\bar{D}^*$), two and all three channels. The error bars combine the extrapolation error with the error obtained by varying the momentum partitioning parameter ζ. The black line is a fit to the data points together with an error band. Figure published in [5].

for isospin zero[8]. This state also comes with an open-strange partner (with isospin 0) and strangeness of minus one. In table 1.11 we have also listed the experimental candidate for our calculated tetraquark state. We found for all calculations that the $D^*\bar{D}^*$ component is subleading whenever lighter D-meson combinations are considered. Therefore, we do not discuss them separately within each section. We will now go through the hidden-charm channels:

The $0(1^{++})$ channel In our setup the state includes a combination of $D\bar{D}^*$, $J/\Psi\omega$ and SA components, as listed in table 1.9. The results for the full calculation and selected subcomponents are shown in figure 1.9. We plot the $cq\bar{q}\bar{c}$ tetraquark mass as a function of the light-quark mass m_q. We obtain the points in this plot by calculating the eigenvalue curve for the input mass m_q, $\lambda^{(m_q)}(M)$ of equation (1.31) as a function of the tetraquark mass M up to the maximal value we determine as described in the last subsection. If the eigenvalue curve $\lambda(M) = 1$, we have found a bound state and consequently $M_{cq\bar{q}\bar{c}}$, which is shown in the plot. If $\lambda(M) \neq 1$ for $M \leq M_{max}$ we fit the data points and solve $\lambda_{fit}^{(m_q)}(M_{cq\bar{q}\bar{c}}) = 1$. The black line is a fit through the last 7 points on the curve and the shaded area is the confidence band of the fit given the black errorbars. The fit at $m_q = m_u = m_d$ is the result we get for our $X(3872)$ candidate. We obtain a mass of 3916(74) MeV, whose central value is slightly above the experimental value. For the hidden-strange partner we find

---

[8]Again, this is due to our construction principle and is in principle possible if we include more momentum dependence in the dressing functions f_i, which are currently only S_0 dependent, so that they have even Pauli and CC symmetry. However, higher components would stem from "excited" meson-meson components and are most likely suppressed.

a mass of $4068(61)\,$MeV and we identify it with the $X(4140)$.

The left panel of figure 1.9 shows the results if we consider only one single component. We see that the heavy-light diquark-antidiquark component alone produces a heavy state with a mass in the region of 4.5 GeV, similar to the hadro-charmonium-only calculation. The corresponding thresholds are also shown in the left panel. The diquark threshold lies roughly 1 GeV above the other two thresholds, which naturally explains the high mass, although the diquark-antidiquark component itself lies below the threshold.

In the right panel the mass curve for the different setups is shown. One can clearly see that the diquarks hardly contribute and that to a satisfactory degree one can reproduce the result of the full calculation including all three components with the HLM component only (red points).

The small HC component we find is in line with the experimental expectations for the $X(3872)$ as shown in table 1.1, since the branching fraction into hadro-charmonium like states is rather small compared to the decays into open-charm mesons. Our result lies slightly above threshold. Due to the error we obtain, one should however be careful with this statement and a proper treatment of the resonant system would give more insight. At this stage we can only with confidence say that the state is close to the threshold, which is also in line with experiment. The $X(4140)$ was only found in a hadro-charmonium-like decay mode so far. From our calculations we would expect a strong HLM mode into open charm and open-strange $D_s, \bar{D}_s^*$ mesons.

Theory comparison: Our result of a dominant HLM component is in line with the molecular picture[9] we discussed in section 1.1. The findings, however, contradict the diquark-antidiquark picture somewhat, since we find the diquark-antidiquark component to be subleading and producing a much heavier state if considered individually. Our identification of the $X(4140)$ with the strange partner of the $X(3872)$ is consistent with the Quark-model four-quark calculation of [117]. We predict (almost) degenerate isospin partners of the $X(3872)$ in the same channel, which is a prediction that also the tetraquark model in reference [50] makes.

The $0(0^{++})$ **channel**   This state has $D\bar{D}, D^*\bar{D}^*, J/\Psi\omega, SS$ as well as $\eta_c\eta$ and AA components, we neglect the last two. The results in this channel are shown in the left panel of figure 1.10 and follow a similar pattern as the 1^{++} channel: The HLM component is once again clearly dominant. The influence of the diquarks is almost negligible and the HC component is again well above the threshold. However, there seems to be some admixture of hadro-charmonium for the full calculation. A natural candidate in this channel would be the $X(3915)$. The quantum numbers of this state are not yet settled. They could be 0^{++} or 2^{++}. It is found in the $\omega J/\Psi$ system in experiment. However, our result of $3503(422)\,$MeV is relatively light compared to the $X(3915)$. Although the RL D mesons are lighter then the experimentally observed ones, which could explain some "missing" mass in the scalar channel in our approach, we

---

[9]It is also possible to construct a hidden strange molecule from D_s mesons, see [116]. Although π exchange is not possible, η exchange in principle is.
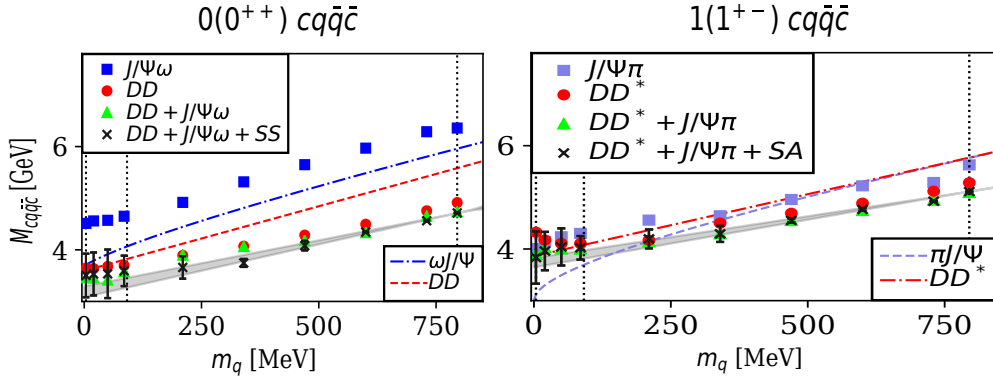
Figure 1.10.: Masses of the $I(J^{PC}) = 0(0^{++})$ and $1(1^{+-})$ four-quark states as a function of the current-quark mass. Left: $I(J^{PC}) = 0(0^{++})$ solutions for the individual $D\bar{D}$, $J/\psi\,\omega$, as well as $D\bar{D} + J/\psi\,\omega$ and the full calculation including diquark-antidiquark, together with the relevant thresholds are shown. Right: $I(J^{PC}) = 1(1^{+-})$ solutions for the individual $D\bar{D}^*$, $J/\psi\,\pi$, as well as $D\bar{D}^* + J/\psi\,\pi$ and the full calculation including diquark-antidiquark, together with the relevant thresholds are shown.

naively expect additive contributions of the order of only 100 MeV if we had used the correct experimental masses. Once again we also predict a strange part at 3592(295) MeV and another degenerate isospin triplet.

Theory comparison: The light scalar is also compatible with the diquark-antidiquark model [50]. The molecular picture does not find a low lying scalar because $D^0\bar{D}^0$ cannot exchange a pion, but it also does not exclude it.

The $1(1^{+-})$ channel This state is a combination of $D\bar{D}^*$,$D^*\bar{D}^*$,$J/\Psi\pi$,AS, as well as $\eta_c\rho$ and AA. We neglected the last two. The results for different individual setups are shown in the right panel of figure 1.10. The picture is different compared to the $0(1^{++})$ channel: While the diquarks again seem to be subleading, we find a non-negligible hadro-charmonium component, which is also lighter in mass compared to the 1^{++} as shown in the right panel. This seems natural due to the lower lying $\pi J/\Psi$ threshold compared to $\omega J/\Psi$.

We find a mass of 3741(91) MeV and 3892(81) MeV for the light and strange state, respectively. We identify the light state with the $Z(3900)$, which is seen in both hadro-charmonium and open-charm meson states in experiment, with a factor of six higher branching fraction into the latter one. There is no experimental candidate for the strange state. Again, we predict three degenerate isospin partners for the $Z(3900)$ as well as a zero isospin state that is also degenerate.

Theory comparison: Interestingly we confirm the prediction of the molecular picture that (including only HLM components) we find the same mass in the $1^{+\pm}$ channels, as shown in the left panel of figure 1.11. However, in addition we find the presence of a non-negligible HC component. Our identification with the $Z(3900)$ is consistent with [50], however, in that model there is another s-
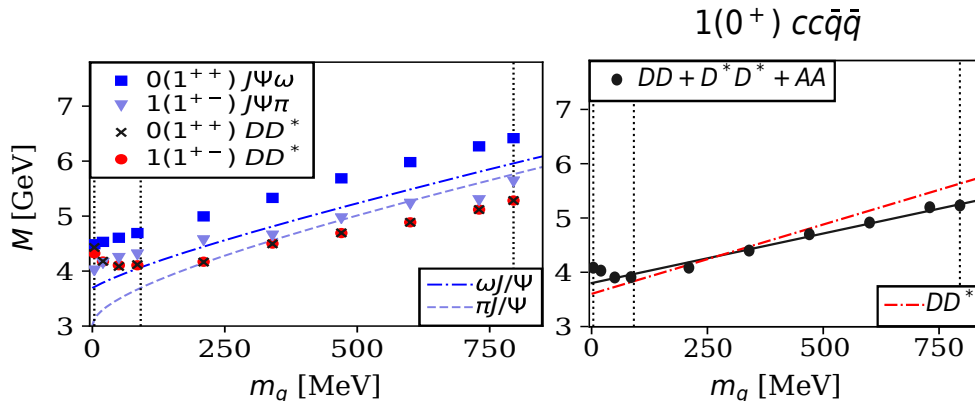
Figure 1.11.: Mass of the $I(J^{PC}) = 1(1^{+-})$, $0(1^{++})$ and $I(J^P) = 1(0^+)$ four-quark states as a function of the current-quark mass. Left: The calculations for the respective hadro-charmonium components of the $0(1^{++})$ and $1(1^{+-})$ state (blue) and the HLM components for both channels are compared. The latter have the same mass. Right: The full calculation for the $I(J^P) = 1(0^+)$ open-charm tetraquark is shown.

wave state in the channel that is identified with the $Z(4020)$. Since we calculate only ground states we cannot say anything about the excited states except that they must be higher in mass.

Open charm   Our results for the open-charm region are also summarized in table 1.11.

The results for the $1(0^+)$ state are shown in the right panel of figure 1.11. Similar to the hidden-charm tetraquarks, the scalar $1(0^+)$ state is also the lightest of the ones we consider. It contains DD, D^*D^* and AA components and we need both, the HLM and DI components, to obtain a smooth $M_{cc\bar{q}\bar{q}}(m_q)$ curve. It is not possible to construct a $0(0^+)$ state in our approach.

In the axialvector channel we find that the $1(1^+)$ state is heavier than the $0(1^+)$ state. There are two main differences: Firstly, the $0(1^+)$ state includes D^*D^* components, whereas the $1(1^+)$ state does not, see table 1.9. Since we found in our calculations that this component is subleading and can be neglected, the mass difference is due to the second difference, the diquarks: The $1(1^+)$ state contains a heavy-axialvector diquark and a light-axialvector antidiquark, while the $0(1^+)$ state contains a light scalar antidiquark. In the $1(1^+)$ case the diquarks seem to bring down the mass a little, see figure 1.12, whereas in the $0(1^+)$ case the diquarks seem to increase the mass. In contrast to the hidden-charm states we also find that the "meson-only" calculations do not yield identical results. Here the $0(1^+)$ meson component is even a little heavier than for the $1(1^+)$.

The open-charm open-strangeness tetraquarks show another particularly interesting feature. Our results for a $1(1^+)$ $cc\bar{q}\bar{q}$ tetraquark are shown in the right panel of figure 1.12. Its mass curve at the strange quark mass is precisely
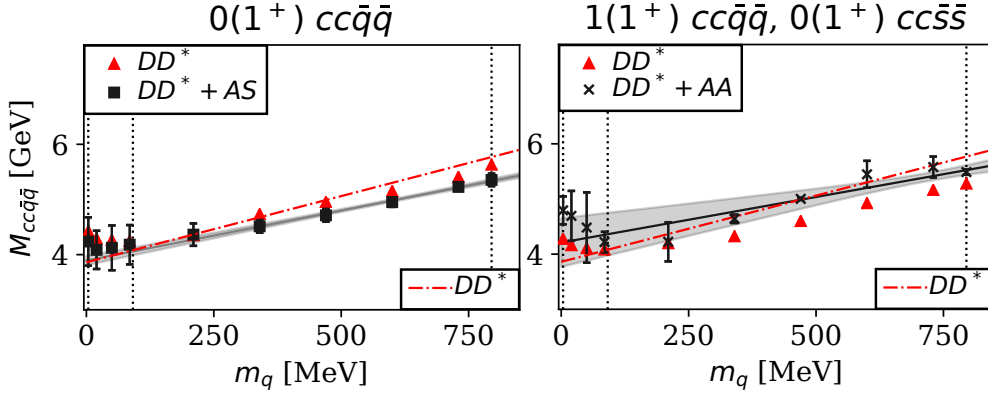
Figure 1.12.: Mass of the $I(J^P) = 0(1^+)$ (left) and $1(1^+)$ (right) four-quark
state as a function of the current-quark mass. Red points include
only DD^* components, black points include also diquarks. The
DD^* is the lowest lying threshold, since the diquarks are heavier.

describing a $0(1^+)$ $cc\bar{s}\bar{s}$ tetraquark. One can verify this by looking at the flavor
tensors in equation (1.55) and replacing the light quarks u, d with two strange
qaurks. Since our $I = 1$ axialvector mass curve lies above the $I = 0$ we obtain a
relatively large mass gap of almost 500 MeV between the $0(1^+)$ $cc\bar{q}\bar{q}$ and $0(1^+)$
$cc\bar{s}\bar{s}$ states.

Theory comparison: There are no experimental candidates yet but we
compare with other theory predictions that we collected earlier in table 1.4.
First of all our result for the $0(1^+)$ mass is in the ballpark of other theory
predictions. While it is roughly 200 MeV lower then the one calculated in [54],
we do confirm the mass ordering $M_{1(1^+)} > M_{0(1^+)}$ with a mass difference of
roughly 300 MeV compared to the 200 MeV that were found in [54] based on
heavy-quark spin symmetry. A further similarity is the the non-existence of a
$0(0^+)$ tetraquark state. The $1(0^+)$ tetraquark in [54] is part of a spin triplet
with $0^+, 1^+, 2^+$ states with almost equal masses of 4146 MeV, which is roughly
150 MeV heavier than the $0(1^+)$ state. This is different in our calculations,
where the scalar is lighter than both, the $I = 0$ and $I = 1$ axialvector state by
roughly 100 and 400 MeV, respectively.

Channel comparison We can now compare the channels in various ways. Let
us first look at the internal components at the physical point where $m_q = m_u =
m_d$. This is shown in figure 1.13.

It seems that we find a HLM dominated state both in the 0^{++} and 1^{++}
channels, which we conclude because the inclusion of HC and DI components
does not influence the results much. The HLM component is also important
in the 1^{+-} channel. However, in contrast to the former channels, the HC
component is also important and the $J/\Psi\pi$-only state is much lighter than
the $J/\Psi\omega$-only state. The inclusion of the $\eta_c\rho$ component could magnify the
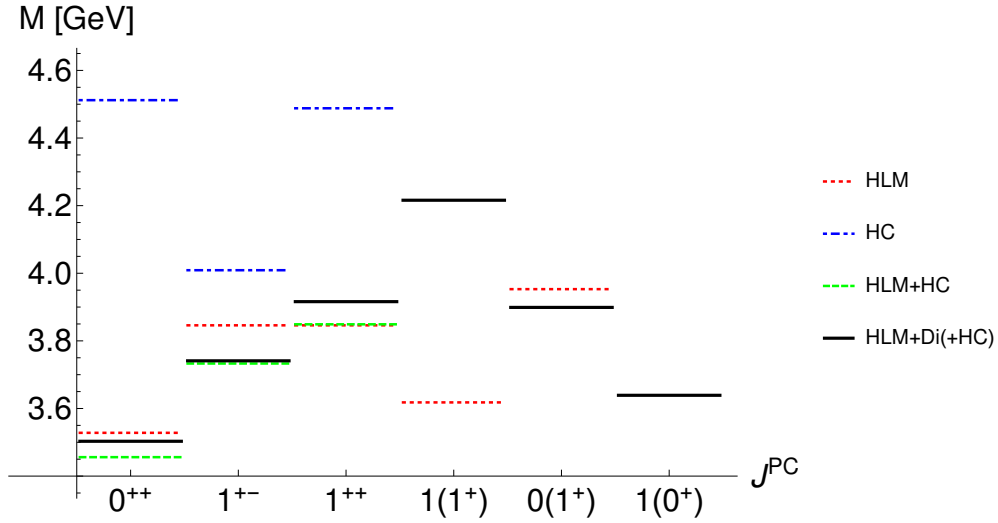importance of the HC component.

Figure 1.13.: The masses of the tetraquarks we calculated are shown for different channels and different components of the amplitude. They were extracted by evaluating a linear fit to the $M_{cc\bar{q}\bar{q}}(m_q)$ curve at $m_q = m_u$, or calculated directly if the $cc\bar{q}\bar{q}$ state is bound.

The effect of the diquarks is small in all hidden-charm channels, whereas it is non-negligible for the open-charm states. In this sector there is no separate HC component possible, but the diquark takes this part from the heavy-quark perspective: For hidden charm the HC component consists of a heavy $c\bar{c}$ and a light $q\bar{q}$ meson, whereas for open-charm the diquark-antidiquark component consists of a heavy cc diquark and a light $\bar{q}\bar{q}$ antidiquark. From this point of view the situation in the open-charm sector is comparable to the hidden-charm sector: The $(0)1^+$ state is again HLM-dominated like the 1^{++} state, the $(1)1^+$ has an important DI component like the important HC component of the 1^{+-}. It is interesting that the mass hierarchy in this identification is, however, inverted.

As we have discussed before, the high mass of the $1(1^+)$ state also causes the high mass of the $0(1^+)$ $cc\bar{s}\bar{s}$ state, as can be seen in figure 1.14, because they share the same symmetry.

Although the $0(1^+)$ state is in the same mass range as the $0(1^{++})$ its strange partner is therefore much heavier then the one of the $0(1^{++})$ that we identified with the $X(4140)$. That leads to a "mass gap" in that channel of roughly 460 MeV compared to roughly 150 MeV in the 1^{++} channel, which is almost the same as for the 1^{+-} state. It should be stressed again that these numbers come with large errors and our predictions should be seen as qualitative features.

We see that in both open-and hidden charm the scalars are lighter than the axialvector states. However, a lighter scalar candidate than the $X(3915)$ is currently not found. Interestingly, the lightest open-charm tetraquark has $I = 1$ and no $I = 0$ partner, except the one with open strangeness. In the axialvector channel we find the lightest state to be the $I = 0$ state, whereas the $I = 1$ state is much higher in mass, as is the open-strangeness state.
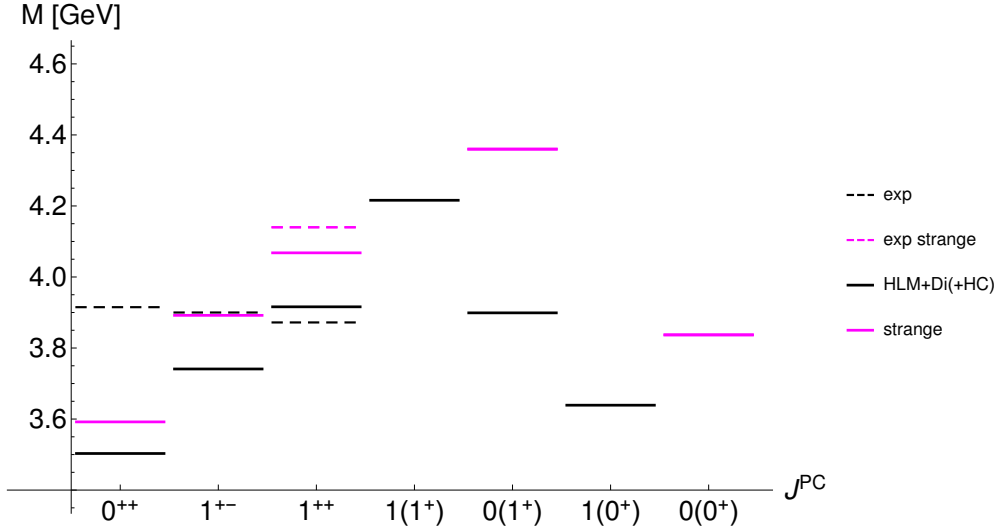
Figure 1.14.: The masses we calculated for the tetraquark are compared to experimental states.

1.6. Summary

We managed to answer the questions we posed about the internal structure of the states and their dominant subcomponents in various channels. The "physical construction" of the amplitude made this possible. By using the physical basis in connection with our pole residue structure we avoided dynamical pole generation and the complexity was reduced, which made a treatment of different states possible. Imposing symmetries on the tetraquark amplitudes allowed us to see the physical content before even starting the calculations, as shown in table 1.9 and during the calculations we found which parts of the amplitude were dominant in a given channel.

1.6.1. Physics

We have found that in our approach the importance of internal sub-clusters varies from channel to channel. For the hidden-charm tetraquarks we observed the general trend of negligible diquark but strong HLM components, eventually accompanied by hadro-charmonium. We find degenerate isospin triplet and singlet states for every quantum number. The $X(3872)$ and $Z(3900)$ can be identified with our $cu\bar{u}\bar{c}$ $0(1^{++})$ and $1(1^{+-})$ states, respectively, whereas our scalar state is lighter than the experimental candidate $X(3915)$. All channels come with an $I = 0$ $cs\bar{s}\bar{c}$ state in our approach and we identify the $0(1^{++})$ state, which carries a strong HLM compoenent, with the $X(4140)$. Future analyses of the $D_s D_s^{(*)}$ as well as $J/\Psi\phi$ data such as the one in [25] will be highly interesting to compare against our predictions for the hidden-charm hidden-strangeness states, especially since we predict a strong HLM component, but the $X(4140)$ for instance has only been found in $J/\Psi\phi$ so far.

In the open-charm sector we find that the diquark components are non-

negligible. We predict a light scalar state, an $I = 0$ axialvector in the mass range of the $X(3872)$ and a heavier $I = 1$ axialvector. Furthermore, we see a large "mass gap" between the $0(1^+)$ $cc\bar{q}\bar{q}$ and $cc\bar{s}\bar{s}$ states in the axialvector channel.

1.6.2. Remaining problems and connection to the next chapter

While we could calculate the real part of the mass of heavy-light tetraquarks by extrapolating the quark-mass curve down from $cc\bar{c}\bar{c}$ (where our states are bound), the question about the resonance properties of the tetraquark states we calculated could not yet be answered. In the introduction we stated three criteria for the proper description of a resonance in the BSE-DSE framework: The presence of a decay channel; the proper treatment of the singularity structures (by means of a path deformation) and analytic continuation to (or direct calculation in) the second Riemann sheet. Although decay channels in the form of intermediate two-body poles are present in the tetraquark BSE, we did not perform a path deformation and, consequently, could not perform an analytic continuation to look for resonance poles in the second Riemann sheet.

We want to lay the foundation for addressing these issues and investigate a method to extract resonance poles properly. This sets clear goals for the next chapter:

- construct a simpler, yet similar system with a built in decay channel and a similar singularity structure,

- take the singularity structure into account properly,

- find the resonance pole in the second Riemann sheet.

With these goals in mind, the $q\bar{q}$ sector beyond the RL truncation serves as the best learning example.

2. Beyond RL: ρ and σ as dynamical resonances

2.1. Motivation

The main motivation of this chapter is to explore a technique for treating resonances in the DSE-BSE framework, which can be applied to tetraquarks in the future. In terms of physics, we want to investigate the light scalar meson sector, especially the $0(0^{++})$ state. Although the lightest scalar $q\bar{q}$ states are p waves in the quark model, the mass of the σ as listed in the PDG is only between 400-550 MeV. This is just one of the reasons that make the light scalars interesting; we will discuss the physics in depth in the next section.

Technically, mesons are bound states in the rainbow-ladder (RL) truncation, which is due to missing decay terms in the meson BSE kernel. The gluon exchange alone does not provide a decay channel. However, almost all light meson states lie above strong decay thresholds and hence this description cannot be realistic. By contrast, in the tetraquark equation the gluon exchange is sufficient to produce decay thresholds due to resummation in the quark-quark and quark-antiquark pairs.

A method of extending the RL description of the ρ meson in a consistent way has recently been introduced [7]. A $\pi\pi$ decay term was introduced in the scattering kernel of the meson BSE and the resonance properties were extracted from the pole location in the second Riemann sheet in the complex P^2 plane, where P is the total momentum of the resonance. This "extended" ρ meson will serve as a playground to test and further improve the method as well as lay the foundation for a description of the similarly extended description of the $q\bar{q}$ scalar state. We develop an improved method that is necessary to describe the latter. Equipped with this method, the application to (light scalar) tetraquarks should be straightforward in future works.

2.1.1. Light mesons

Spectrum Although the light meson spectrum has been known for quite some years, it is still subject to intense debate. It is shown for selected quantum numbers in the left panel of figure 2.1. The grey boxes are the multiplets. The pseudoscalar states contain the light pions, the strange kaons and the η mesons, which are heavy due to the $U(1)$ anomaly. The vector states are relatively light, which is in line with their s-wave assignment in the non-relativistic quark model. For mesonic states the quantum numbers of a state J^{PC} are given by:

$$P = (-1)^{L+1}, \qquad C = (-1)^{L+S}, \qquad J = |L - S|, ..., L + S.$$

This implies that the positive parity scalar, axialvector and tensor ground states with $J^{PC} = 0^{++}, 1^{++}, 2^{++}$ have angular momentum $L = 1$, which puts their expected masses in the same area. This would be true experimentally if the

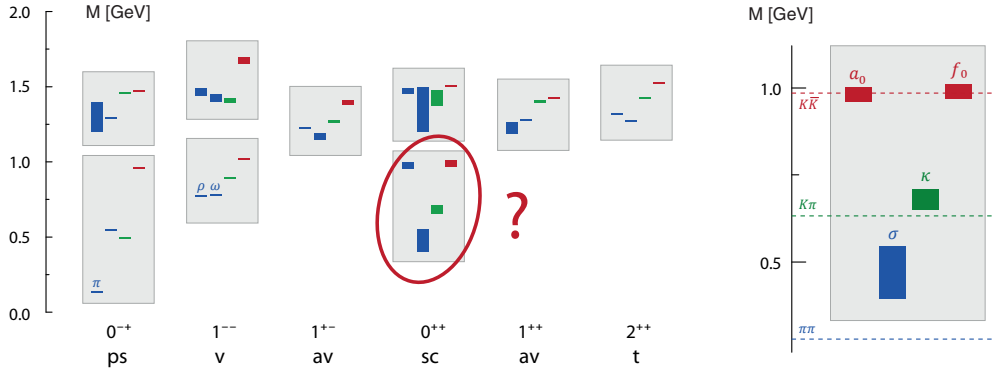## 2. Beyond RL: ρ and σ as dynamical resonances

Figure 2.1.: light meson spectrum from the PDG [118]; the bars show the experimental mass range. The light scalar mesons are magnified on the right. Figure published in [119].

lowest-lying scalar multiplet was in the mass range of the first excited multiplet. However, that makes it hard to explain the properties of the lowest lying multiplet in the $q\bar{q}$ picture. Instead, one is rather tempted to identify the first excited multiplet in the scalar channel with the $q\bar{q}$ ground states.

The σ or $f_0(500)$ Let us take a closer look at the most prominent member of the multiplet, the σ. Combining new data with dispersive approaches to $\pi\pi$ scattering using Roy equations[1] [121, 122], the σ is now again listed in the PDG with a pole position of $(400\ldots550) - i(200\ldots350)$ MeV [118]. An extensive review on the history of the σ can be found in [123]. As a $0(0^{++})$ state it can in principle be a mixture of $q\bar{q}$, glueball, $q\bar{q}q\bar{q}$ and even higher components. The composition is a priori unknown; however, some arguments exist:

Firstly, the scalar glueballs should be heavier, with masses of around 1.5-1.8 GeV, see [123] and references in there. Furthermore, a pure glueball does not provide a multiplet and therefore the strange multiplet members (κ) would not exist if the glueball component was the dominant one.

Secondly, large-N_c QCD predicts the behavior of $q\bar{q}$ states for increasing N_c. For $N_c \to \infty$, they should become stable. Their mass should become constant and their width should scale with $1/N_c$. The dynamically generated vector-meson poles in unitarized-chiral perturbation theory follow this behavior, but it is not seen for the σ and κ resonances whose width rather grows with N_c [124]. This could hint towards a $qq\bar{q}\bar{q}$ (or two-meson) state, which becomes a two-meson continuum with increasing N_c. It should be mentioned however, that a recent argument by Weinberg says that $qq\bar{q}\bar{q}$ states in the large N_c limit can be either narrow ($1/N_c$ scaling) just like normal $q\bar{q}$ states, or broad and scale with N_c [125][2].

---

[1]Roy equations [120] relate partial wave amplitudes in the physical region to the $\pi\pi$ s-wave scattering length.

[2]Weinberg suggested that one should actually look at the decay amplitude which consists of two parts, one proportional to N_c and the other proportional to $1/N_c$, where the former

	a_0	σ	κ	f_0
$q\bar{q}$	$\begin{Bmatrix} d\bar{u} \\ (u\bar{u} - d\bar{d}) \\ u\bar{d} \end{Bmatrix}$	$(u\bar{u} + d\bar{d})$	$\begin{Bmatrix} d\bar{s} \\ u\bar{s} \end{Bmatrix} \begin{Bmatrix} s\bar{u} \\ s\bar{d} \end{Bmatrix}$	$s\bar{s}$
$(qq)(\bar{q}\bar{q})$	$\begin{Bmatrix} ds\bar{s}\bar{u} \\ s(u\bar{u} - d\bar{d})\bar{s} \\ us\bar{s}\bar{d} \end{Bmatrix}$	$udd\bar{u}$	$\begin{Bmatrix} du\bar{s}\bar{u} \\ ud\bar{s}\bar{d} \end{Bmatrix}, \begin{Bmatrix} sd\bar{u}\bar{d} \\ su\bar{d}\bar{u} \end{Bmatrix}$	$s(u\bar{u} + d\bar{d})\bar{s}$

Table 2.1.: The quark content of a $q\bar{q}$ octett is compared to the quark content of a diquark antidiquark from [2]. We left out the normalization factor $\frac{1}{\sqrt{2}}$ in front of the a_0, σ in the first row and a_0, f_0 in the second row.

The non-$q\bar{q}$ nature of the σ is supported by many studies in different frameworks: unitarized ChPT [126], quark models [48], the extended linear sigma model [127] and QCD sum rules [128], just to name some.

Are the light scalars tetraquarks? The idea of considering the light scalar mesons as tetraquarks is quite old [2]. Lets review some of the arguments that support this hypothesis: As mentioned, the scalars are p waves and therefore their masses are expected to be in the range of axialvector and tensor states around $1 - 1.5$ GeV. There is indeed a multiplet in this mass range, where members could predominantly be $q\bar{q}$. However, the properties of the lowest-lying multiplet including the σ are different. Their masses are between $0.5 - 1$ GeV. Furthermore, their decays are peculiar. The σ decays into $\pi\pi$ and is very broad, while the κ which decays into $K\pi$ is also quite broad and carries strangeness. The isospin $I = 0$ $f_0(980)$ and $I = 1$ $a_0(980)$ lie at the $K\bar{K}$ threshold and are quite narrow.

As one can infer directly from comparing the mass ordering of the states within the various "mesonic" multiplets in figure 2.1 to each other, the mass ordering is also different for the light scalar states and especially the near degeneracy of a_0 and f_0 cannot be explained in a $q\bar{q}$ picture. The solution proposed by Jaffe [2] combines (color-and flavor antitriplet) scalar diquarks and antidiquarks. The resulting flavor wave functions are collected in row two of 2.1. This assignment would explain the mass ordering considering the strange quark content of the states: The σ has no strange quark, the κ has one, whereas the f_0 and a_0 contain two strange quarks, as listed in table 2.1. Also, the decays can be explained better: The a_0 can decay to $a_0 \to \pi\eta$ and couple to $K\bar{K}$ with its internal $s\bar{s}$ pair. The broad σ and κ can fall apart into $\pi\pi$ and $K\pi$, respectively, through the OZI-superallowed mechanism.

---

part is zero if the tetraquark decay into any pair of light mesons is forbidden by its quantum numbers.

2.1.2. Scalars in RL and beyond

As we have discussed already in the first chapter the binding mechanism of colored diquark degrees of freedom is quite different to the one in a BSE calculation, where quarks interact via the exchange of gluons. However, one can reformulate the four-body BSE to Fadeev-Yakubovsky equations and afterwards reduce them to coupled two-body equations [84] which are similar in spirit to the diquark-antidiquark model for baryons. These equations however, contain not only diquark-antidiquark components but also meson-meson components.

The four-quark interpretation of the light scalars has been investigated in the BSE-DSE approach in such approximated equations, as well as with the four-body equation itself in the rainbow ladder approximation [3, 84]. It turns out that both produced a light σ with a mass of about 350-400 MeV. The latter approach also reproduced the mass ordering within the scalar multiplet that is found experimentally. For the σ, the authors found a four-quark state with a strong $\pi\pi$ component. The system exhibits dynamically generated two-body thresholds and is in principle resonant, however, the width was not yet extracted.

The picture in the $q\bar{q}$ scalar-meson channel is different in the RL approximation. Here the σ has a mass of roughly 660 MeV, which is too heavy to interpret it as a member of the lowest multiplet and too light to assign it to the higher multiplet. However, recent beyond-rainbow ladder calculations push up the mass of the $q\bar{q}$ scalar to roughly 1.1 GeV [129]. The higher σ mass seems to be a general trend in other works as well [130, 131]. This behavior is somewhat in line with the quark model expectations that we discussed earlier and might indicate an identification of the first "excited" scalar multiplet with a $q\bar{q}$ dominated nonet that could itself mix with the lowest-lying scalar glueball [83].

Despite these findings it is still an open and interesting question what the width of these states would be. There is a way to extract a width even for the RL bound states in a static way. For vector mesons and scalar (and vector mesons) this has been done in [132, 133] and [134], respectively. We will compare against these results later. However, in the following we will describe the σ meson (and the ρ as a test case) in the spirit of [7] as a dynamically calculated $q\bar{q}$ state with RL gluon exchange and beyond rainbow-ladder pion-exchange corrections.
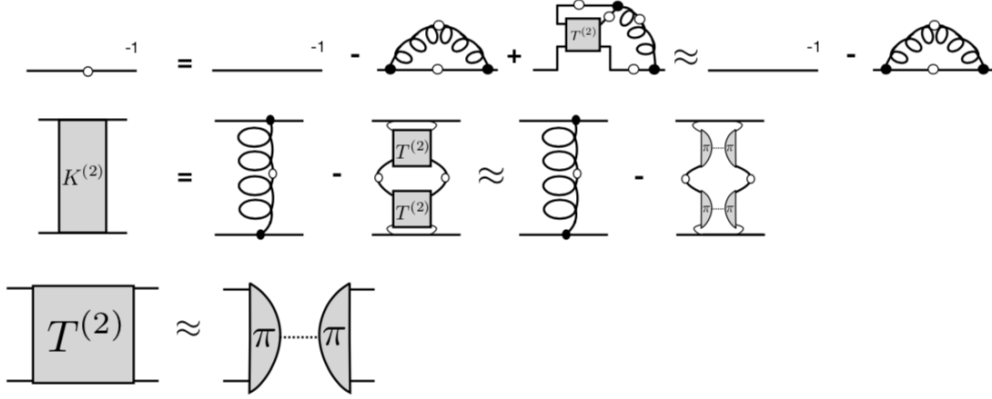
Figure 2.2.: The quark DSE and a consistent two-body kernel are shown in the first and second row respectively. Solid dots stand for bare quark-gluon vertices, white dots indicate dressed quantities. The approximation in the third row assumes that the relevant part of the T-matrix is given by one-pion exchange and leads to the approximated kernel in the second row. The approximated DSE in the first row further neglects the pion contribution to the self-energy.

2.2. $q\bar{q}$ resonances: going beyond RL

Resonances are poles in unphysical (higher) Riemann sheets of the scattering matrix [123, 135]. Light mesonic resonances have been studied in other frameworks, like the quark model [136, 137] and chiral-perturbation theory [138, 139]. In lattice QCD the ρ resonance has been studied in [140–143] and recently the light $I = 0$ scalars have been pioneered as well [144, 145].

Because in RL $q\bar{q}$ states are bound, a realistic description of the QCD spectrum calls for beyond-RL corrections. Recently a method was proposed to dynamically incorporate decays into the BSE-DSE formalism and gain access to the pole structure in the second Riemann sheet for the ρ meson in [7]. It is based on [146, 147] and the idea is diagrammatically shown in figure 2.2. The kernel and self-energy are still related via the AVWTI and therefore preserve chiral symmetry for the BSE and DSE in the first and second row. We make two further assumptions, namely that the T-matrix is dominated by π exchange (3rd row) and that the beyond RL term arising in the quark DSE can be neglected. This is mainly for convenience and methods exist to solve the DSE also with this term included. One can now graphically see that the resulting two-body RL kernel includes explicit $\pi\pi$ intermediate states and is similar to the tetraquark meson-meson kernel that was used in [84].

Finding the complex pole position of the ρ in [7] was accomplished by analytically continuing the dressing functions of the inhomogeneous vertex, which contains the resonance pole in the second Riemann sheet according to equation (1.18), with the Schlessinger point method. Recently, it was shown in [8] how to directly continue the T-matrix to the second sheet via analyticity relations in the BSE-DSE framework. In the following we will set up the equations for the
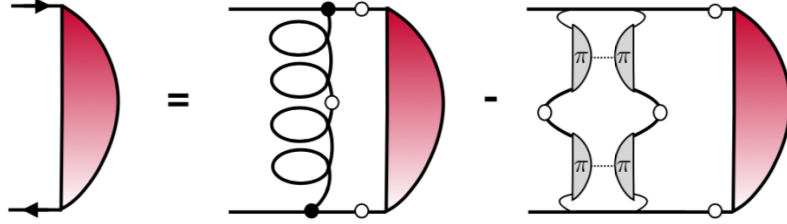
Figure 2.3.: The approximated beyond RL BSE is shown. In addition to the RL-gluon exchange kernel, a two-pion decay term arises.

	R.L	ρ	σ
$C_{\pi\pi}$	$\frac{4}{3}$	1	1
$F_{\pi\pi}$	1	4	6

Table 2.2.: Prefactors of the different diagrams.

ρ and σ mesons and explain the method we use for the analytic continuation of the inhomogeneous amplitude and the eigenvalue curve of the homogeneous BSE.

2.2.1. Kernel and self-energy

The BSE with pion exchange is shown diagrammatically in figure 2.3. We approximate the T-matrix as done in [87][3]. The leading amplitude of the Dirac part of the off-shell π amplitude is approximated by B/f_π, where B is the quark propagator's dressing function of a chiral quark and f_π the pion decay constant. This relation is exact in the chiral limit [87]. This off-shell description of the meson amplitudes is a crucial input to this approach. Details of the approximation are summarized in the appendix C.1. We present the resulting color and flavor factors in table 2.2. The approximation yields a flavor factor of 4 for the ρ and 6 for the σ. Therefore, already at this stage we can expect a larger width for the latter state. The resulting matrix element for the $\pi\pi$ kernel is:

$$f_i(p, P) = C_{\pi\pi} F_{\pi\pi} \int_l \text{Tr}\left[\hat{\tau}_i^{(\alpha)}(p, P)\Gamma_1 S(p - l)\Gamma_2\right] D(l_+)D(l_-) \qquad (2.1)$$

$$\cdot \int_k \text{Tr}\left[\bar{\Gamma}_1 \chi^{(\alpha)}(k, P)\bar{\Gamma}_2 S(k - l)\right]$$

$$= C_{\pi\pi} F_{\pi\pi} \int_l D(l_+)D(l_-) J_i^{(\alpha)}(p, l, P)T^{(\alpha)}(l, P) \qquad (2.2)$$

$$= C_{\pi\pi} F_{\pi\pi} \int_l D(l_+)D(l_-) I_i(p, l, P)T(l, P), \qquad (2.3)$$

where S stands for the quark propagator, D for the free pion propagator

---

[3]See equation 20 therein.

$$D(p) = \left(p^2 + m_\pi^2\right)^{-1},$$

$\chi^{(\alpha)}$ is the Bethe-Salpeter wave function of the state we describe (ρ or σ):

$$\chi^{(\alpha)}(k, P) = S(k_+)\Gamma^{(\alpha)}(k, P)S(k_-)$$

and the momenta $q_\pm$ were defined in (1.27). The projectors onto the Dirac basis are denoted with a hat and the f_i are the dressing functions for the ρ or σ amplitude. The π amplitudes are defined as:

$$\Gamma_1 = \Gamma(p - \frac{l_-}{2}, l_+), \qquad \Gamma_2 = \Gamma(p - \frac{l_+}{2}, -l_-),$$

$$\bar{\Gamma}_1 = \bar{\Gamma}(k - \frac{l_-}{2}, l_+), \qquad \bar{\Gamma}_2 = \bar{\Gamma}(k - \frac{l_+}{2}, -l_-).$$

We have defined two auxiliary quantities $J_i^{(\alpha)}$ and $T^{(\alpha)}$. The index α, that is present for the ρ case only, can be contracted, as we will see in section 2.2.3. Consequently, we can also work with the quantities I and T without the index α, that are used in the last line of equation (2.3). We define the four-vectors in the BSE to be:

$$P^\mu = \begin{pmatrix} 0 \\ 0 \\ 0 \\ iM + \frac{\Gamma}{2} \end{pmatrix}, \; p^\mu = p \begin{pmatrix} 0 \\ 0 \\ \bar{z}_p \\ z_p \end{pmatrix}, \; l^\mu = l \begin{pmatrix} 0 \\ \bar{y}_l \bar{z}_l \\ y_l \bar{z}_l \\ z_l \end{pmatrix}, \; k^\mu = k \begin{pmatrix} 0 \\ \bar{y}_k \bar{z}_k \\ y_k \bar{z}_k \\ z_k \end{pmatrix}, \qquad (2.4)$$

where we introduced the resonance mass M and width Γ in P^μ.

2.2.2. Singularity structure and path deformation

The decay term we have introduced in equation (2.3) depends on T and I as well as the two pion propagators $D(l_\pm)$. They are singular at $l_\pm^2 = m_\pi^2$, or

$$0 = \left[m_\pi^2 + \left(\frac{P}{2} + l\right)^2\right]\left[m_\pi^2 + \left(\frac{P}{2} - l\right)^2\right]$$

$$\Rightarrow l_{1,2}^2 = -\frac{M^2 z^2}{2} + \frac{M^2}{4} - m_\pi^2 \pm iMz\sqrt{(1 - z^2)\frac{M^2}{4} - m_\pi^2} \qquad (2.5)$$

and therefore the singularity moves into the integration domain in l^2 whenever $M > 2m_\pi$. The singularity structure in the complex l^2 plane is shown in figure 2.4 for fixed M and Γ.

One has to apply a suitable path deformation that avoids the singularity structure, as was done for similar problems in [88, 148–151]. We investigate the different parameterizations:
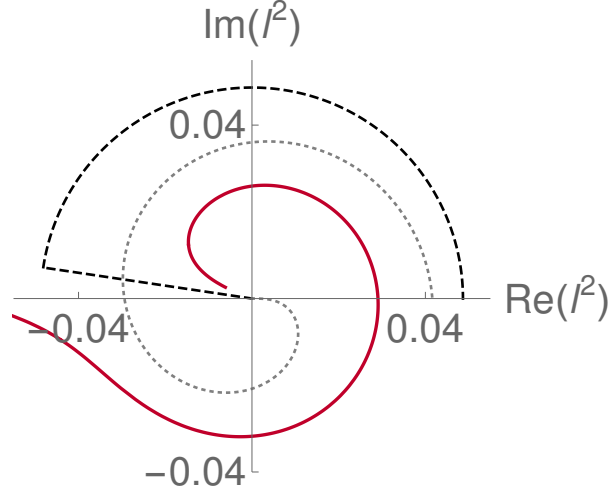
Figure 2.4.: We show the two-pion branch cut (solid line) and two possible paths avoiding the singularities in the complex l^2 plane for fixed $M = 0.44$ GeV and $\Gamma = 0.065$ GeV.

$$l^2(z) = e^{-i\pi(z+1)}\sqrt{1+z}|m_\pi^2 + t| \qquad z \in [-1, 1] \tag{2.6}$$

$$l^2(z) = \begin{cases} t(z+1) & z \in [-1, 0) \\ |t|e^{i\ arg(t)(1-z)} & z \in [0, 1] \end{cases}, \tag{2.7}$$

where we have used the shorthands

$$t = P^2/4, \qquad |x|e^{i\ arg(x)} = x.$$

The path is not unique and we compared the spiral and the straight line plus arc that was also used in [8]. The cut (solid line) and deformed paths are shown in figure 2.4.

2.2.3. Solving the system

As we have seen in section 1.3 there are two ways of obtaining the pole position from solving the homogeneous or inhomogeneous BSEs from equations (1.17) and (1.18) for a given scattering kernel. We adopt our solution algorithm for these cases:

1) For the homogeneous BSE we use an iterative solver. We use $T^{(\mu)}(l, P) = (l_T^\mu)T(l^2, z_l)$ for the k integral of equation (2.3) and define l_T^μ into $I = J^{(\mu)}(l_T^\mu)$. We obtain the eigenvalue of the homogeneous equation and solve for a pole in its inverse $\lambda' = \frac{1}{1-\lambda}$. One has to be careful at this point: for the σ, the eigenvalue with the biggest absolute value (as obtained by naive power iteration) is not a smooth surface. This is due to crossing eigenvalue surfaces as shown in figure 2.5. The plot shows the comparison of the results of the two biggest eigenvalues
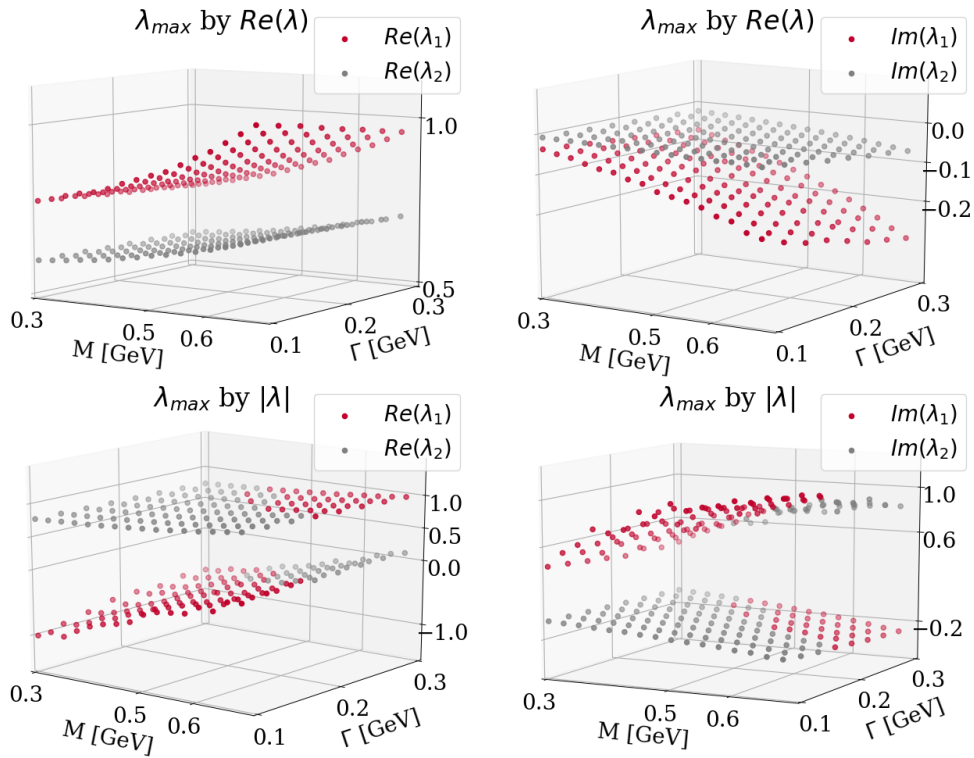
Figure 2.5.: The biggest eigenvalues $\lambda_1 > \lambda_2$ by real part and absolute value for the σ calculation are shown in the first and second row, respectively. Within each row the first plot shows the real parts of the two biggest eigenvalues, the second plot shows the imaginary parts.
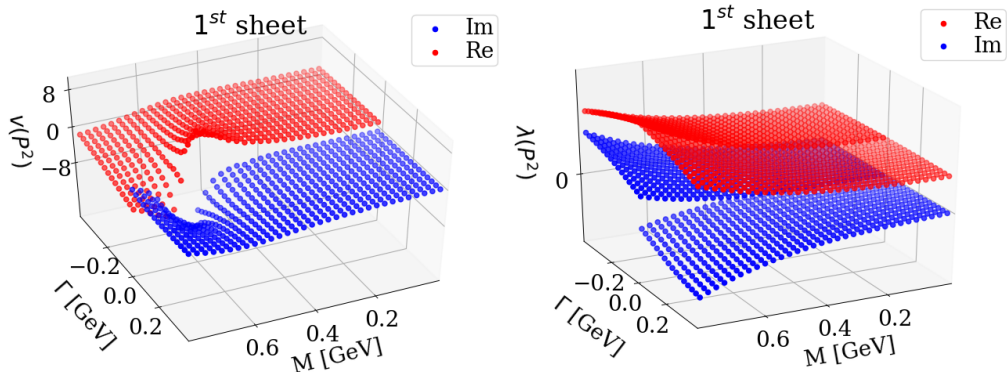
Figure 2.6.: The solutions of the ρ BSE in the first Riemann sheet are shown in the M-Γ plane with the real part in red and imaginary part in blue. The solutions are complex conjugated and it is therefore sufficient to show it in one half plane. Left: solution $v(P^2) = f(p^2 = 0, z = 0, P^2)$ of the inhomogeneous BSE. Right: Solution λ of the homogeneous BSE. We show the solution in both half planes to demonstrate the appearance of a branch cut.

sorted by their real part (first row) and the two biggest eigenvalues sorted by their absolute value (second row). One can see that two eigenvalue curves overlap when the second criterion is used and we consequently identify the biggest eigenvalue by real part with the σ ground state.

2) For the inhomogeneous BSE we precalculate the whole decay kernel once and use a matrix solver to obtain the eigenvalues. In this particular case we pick the bi-conjugate gradient stabilized algorithm, which proved most efficient in [78]. In the following we calculate the quantity $v(P^2) = f_1(p^2 = 0)$, which exhibits the pole structure directly.

We show the result for the eigenvalue $\lambda(M, \Gamma)$ and $v(M, \Gamma)$ in the first Riemann sheet for the ρ case in figure 2.6. One can see the branch cut opening in the imaginary part above the $\pi\pi$ threshold. The values left and right are related via complex conjugation and we need analytic continuation to access the second Riemann sheet and find the pole position. In the following we will discuss the method we use with the ρ meson as an example.

2.2.4. Analytic continuation of the solution

The method was introduced in the context of analytically continuing scattering amplitudes by Schlessinger in 1968 [152]. An efficient implementation of evaluating the resulting continued fraction is described in [153]. The idea is the following: Approximate a function by the fraction of two rational polynomials $R(x) = P(x)/Q(x)$ and use the resulting functional form for analytic continuation. Well written examples for different problems can be found in [154], a comparison to other methods of analytic continuation in [155], an application in hadron physics to problems with simple poles and branch cuts can be found in [156], as well as an enlightening application to scalar theory in [8].
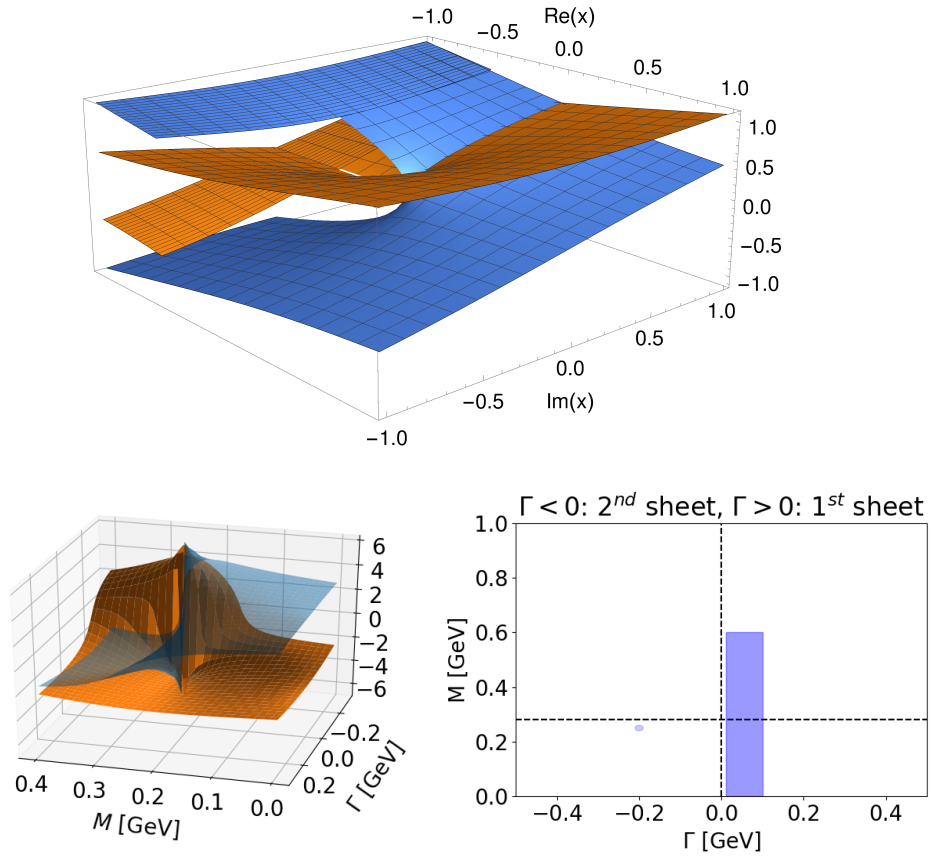
Figure 2.7.: Upper panel: real (orange) and imaginary part (blue) of the $\sqrt{x}$ function are shown. The points for $Im(x) \in [0.01, 0.1]$ and $Re(x) \in [-0.5, -1]$ are used as an input to analytically continue through the branch cut to the second sheet. The real part is exactly on top of the expected result. Lower panel, left: A free particle propagator's real (orange) and imaginary (blue) part with a pole in the complex plane are shown. right: The result on the right is obtained by fitting a Pade approximant to the shaded region for $\Gamma > 0$ and searching for a pole in the fit. The resulting radius is only chosen for visibility, the Pade fit perfectly finds the pole position.

We show two simple examples in figure 2.7. The first one is the sqrt function. It has a branch cut for $x < 0$, which can be seen as a discontinuity in the blue imaginary part. We analytically continue via the Schlessinger point method to the second sheet for $Im(x) < 0$, where the orange real part and blue imaginary part are smoothly connected to their partners on the first Riemann sheet for $Im(x) > 0$ through the branch cut. The second example is shown in the second row of the figure: The reconstruction of a free particle $1/(p^2 + m^2)$ pole with $m^2 = (M - i\Gamma/2)^2$ at $(M, \Gamma) = (0.25, -0.2)$ from data with $\Gamma > 0$. This example mimics the challenge we face when solving the BSE. One can obtain information in the first sheet in the whole plane by direct calculation, but the eigenvalue (or v in the inhomogeneous case) shows a discontinuity in the imaginary part above threshold, compare figure 2.6. So the strategy will be equivalent to this example: Calculate data on one half plane in the first sheet ($\Gamma > 0$ in the following) and analytically continue the results to the $\Gamma < 0$ half plane, which corresponds to the second Riemann sheet in our BSE calculation. The results for the free particle example are shown in the right column of the second row. On the right hand side we show the selected input points in a box and on the left hand side we show the resulting pole position from analytic continuation as a small circle.

Despite its advantages, the Schlessinger-point method is comparable to a fitting procedure and we would like to find out how stable the method is and ideally provide an error estimate. Furthermore, the method approximates the function with a rational approximant

$$f(x) \approx R(x) = \frac{P(x)}{Q(x)}$$

whose poles we would like to find. With increasing N, the degree of the polynmolials P and Q and therefore the number of their (not necessarily distinct) roots increases. It is now possible, that poles are created in the fitting procedure, that are not "true" poles of the function $f(x)$ but a sheer artifact of the rational approximation.

To do both, check the **stability** of the fit and get an **error estimate**, as well as to identify the **true poles** of $f(x)$ we modify the method to what we call the "statistical" approach in the following.

2.2.5. Stability: statistical approach

We fit the rational function $R(x)$ to the given data points for $\Gamma > 0$ for the ρ meson and afterwards extract the polynomial coefficients for $P(x)$ and $Q(x)$, which allows us to visualize the fit in a pole-zero plot, where the poles are given by the roots of R's denominator via $Q(x) = 0$ and the zeros by $P(x) = 0$. We will use the words "pole candidates" and "zeros" in the following for roots of Q and P, respectively. They should however not be confused with actual poles and zeros of the function f that we have approximated, nor necessarily with those of R, since "pole candidates" and "zeros" could still cancel each other in R.

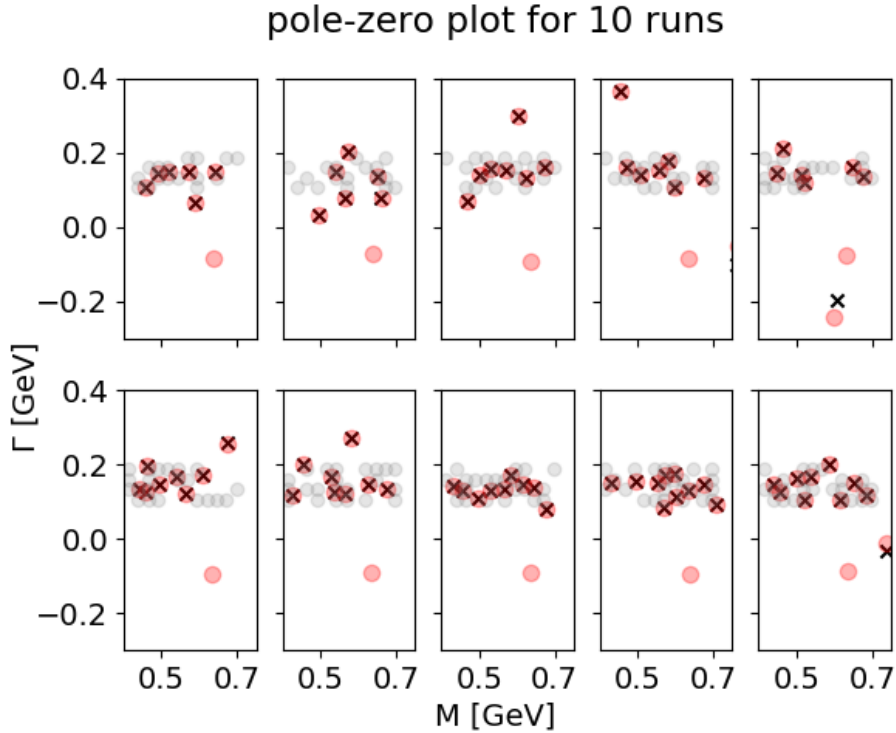Figure 2.8.: The ten panels show ten runs with different, randomly selected input points (grey dots) in the first Riemann sheet for $\Gamma > 0$, together with the resulting pole candidates given by $Q(x) = 0$ (red boxes) and zeros given by $P(x) = 0$ (black crosses) in the first ($\Gamma > 0$) and second ($\Gamma < 0$) Riemann sheet.

An example for a pole-zero plot for the ρ meson is shown in figure 2.8: 10 different fits are shown in the 10 panels of the figure, with increasing number of points from left to right ($N = 16$ to $N = 25$). Within each panel the small grey points are the fit's randomly selected input points for $\Gamma > 0$ on the first Riemann sheet. Red boxes denote zeros of the denominator (zeros), black crosses those of the numerator (pole candidates). Note, that the plot shows the first sheet for $\Gamma > 0$ and the second sheet for $\Gamma < 0$.

There seems to be one "true" pole that appears to be more or less independent of the input points in every of the 10 plots. While most of the other pole candidates have zeros very close by and therefore cancel out of R, we can see in the fifth and tenth panel that a "fake" pole is created on the second sheet. It seems that these "fake" poles appear in random positions, while the "true" pole always appears in more or less the same spot. Now three questions emerge:

- How can "fake" poles be identified?

- What is a suitable algorithm, that can somehow average only over the "true" poles of all the (10) runs?
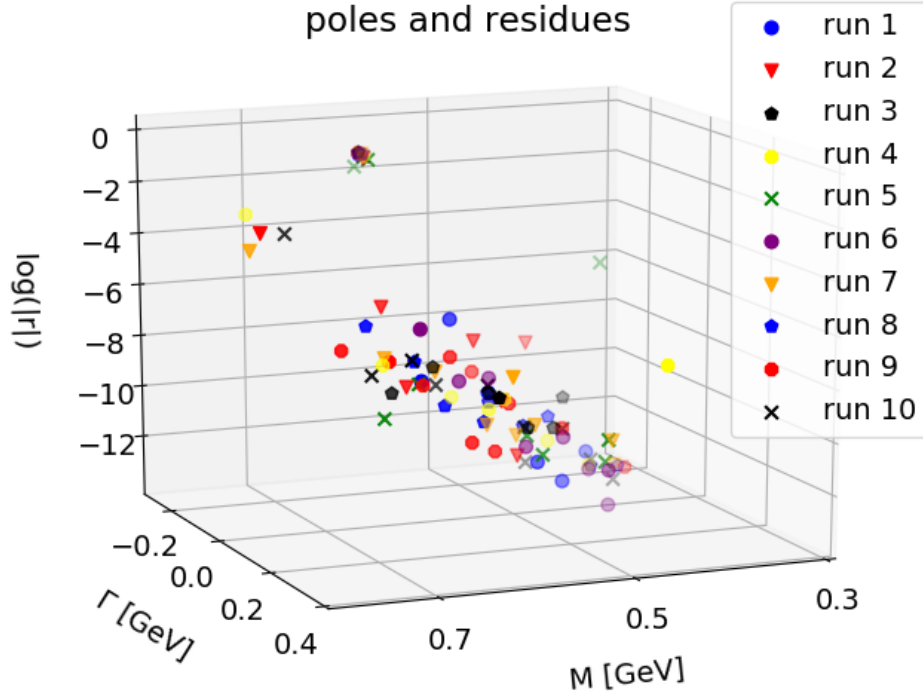
- How can we get an error estimate?

Figure 2.9.: The log of the absolute value of the residues is shown for all poles. Different symbols stand for the ten runs conducted in figure 2.8.

Let us look at figure 2.9 for that purpose. It shows the absolute value of the residue for the pole candidates. One can see, that the pole candidates' residues vary over several orders of magnitude in absolute value. To understand how that can be the case, we need to look at the residue of $R(x) = P(x)/Q(x)$. It is given by:

$$res(R)(x_0) = \frac{P(x_0)}{Q'(x_0)}.$$

Therefore, closeby zeros ($P(x_0) = 0$) create a small residue if $Q'(x_0)$ is not singular. Consequently, poles that should actually be canceled out by a "zero" but are nevertheless present (see again the "fake" pole in figure 2.8) are likely to have a very small residue. That is exactly what we see by comparing the plots from 2.8 to 2.9: There is a cluster with fairly big residues that contains all 10 different symbols (each symbol stands for one of the 10 runs in this example). The poles within this cluster are exactly the 10 red boxes (one in each panel of 2.8) that we assumed to be "true" poles, while almost all other pole residues are orders of magnitude smaller.

Analogously to this example we will define a "true" pole as a pole that has a sizeable residue (compared to the other residues) and appears in all runs, while all other poles are "fake" poles. By run we mean the $N = 10$ independent fits we performed in figure 2.8 in our example. Once this is established, our problem of finding the true pole can be reformulated as finding the cluster of $N = 10$

pole candidates with one pole candidate from each run (with sufficiently high residue) that has minimal radius[4]. This procedure makes it possible to find an algorithm for the determination of the pole position and also provides us with an error estimate, related to the radius of the cluster, and provides confidence that our fit finds an actual pole, which is what we wanted to achieve.

Algorithmically we do the following: Choose N runs with increasing number of points and randomly selected input from a predefined region. Then calculate poles and zeros for each run. The mass is then calculated as

$$M = \left[\frac{\sum_j^N C_j^{(i)}}{N} \right]_{\sigma(C^{(i)})=min}, \qquad (2.8)$$

where σ is the standard deviation

$$\sigma(C^{(i)}) = \sqrt{\frac{1}{N} \sum_{j=1}^{N} |\bar{C}^{(i)} - C_j^{(i)}|^2}.$$

We define $p^{(j)}$ to be the vector of pole candidates ($Q(x) = 0$) of the Pade approximant of run j, sorted by absolute value of the residue. From there we define the i-th cluster $C^{(i)}$ as a set of N pole candidates $p_j^{(i)}$, one from each run and the total set C as the collection of all 2^N clusters:

$$C = p_{j_1}^{(1)} \otimes p_{j_2}^{(2)} \otimes ... \otimes p_{j_N}^{(N)}, \qquad j_k \in \{1, 2\}.$$

Since $p^{(j)}$ is ordered after absolute value of the residue, only the the two poles with biggest residue of each run will be allowed as candidates for the true pole. We identify the true pole as the average of the cluster that has the lowest standard deviation σ as we already pointed out in equation (2.8)[5].

Graphically, this is the circle with smallest radius including one of each symbol in figure 2.10. The circles calculated in this manner are what we will plot as a result in the following section. Since we are looking for sufficiently big residues from each run we accepted only the two biggest residue poles[6]. Consequently the algorithm scales with 2^N, which is already quite slow and can certainly be improved in the future. There is a number of clustering algorithms implemented and ready to use for example in [157], however, our naive implementation proved to be best since we can directly implement the condition of accepting exactly one pole from each run in that way.

---

[4] Perfect data without errors as shown in our example in figure 2.7 might produce the exact same pole position independent of the randomly selected points. Our numerical data, however, are contaminated with errors and therefore we have to look for a cluster, not a single point.

[5] This naturally identifies one "true pole" only, could, however, be easily applied multiple times after throwing the poles of the dominant cluster out, to find all "true poles" if there were multiple, which is not the case here.

[6] Usually the biggest one is sufficient but as shown in the third panel of 2.8, sometimes a zero doesn't perfectly cancel out a fake pole, which leads to a sizeable residue.
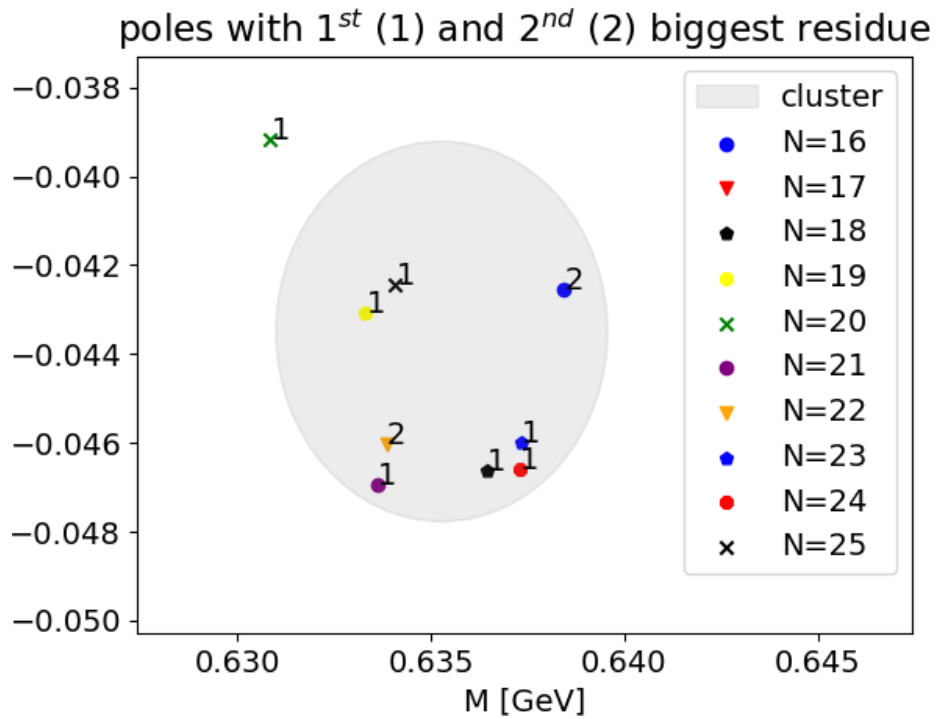
Figure 2.10.: Poles with sizeable residue of the runs 1...10, with the number of input points $N = 16...25$ are shown. The subscript 1 stands for the biggest residue, while 2 stands for the second biggest residue. The circle has its midpoint at the average value of the optimal cluster and the radius is the standard deviation of the cluster.

A typical example for the best cluster is shown in figure 2.10. We can see that all runs produced a pole in the region we show and that it was the one with either biggest or second biggest residue.
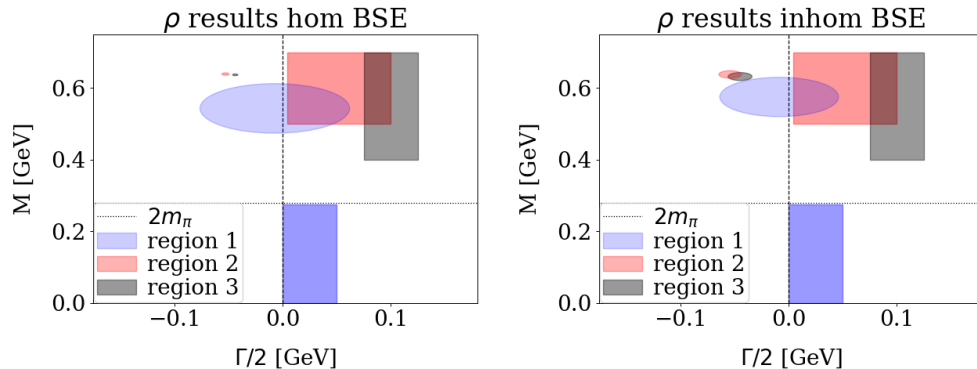
Figure 2.11.: ρ meson. Both plots show the $\Gamma < 0$ half plane of the second Riemann sheet on the left and the $\Gamma > 0$ half plane in the first Riemann sheet on the right. Boxes on the right of each plot stand for data calculated from the BSE on the first Riemann sheet for $\Gamma > 0$, circles on the left are the results obtained from analytic continuation to the second Riemann sheet for $\Gamma < 0$. Left: results from the homogeneous BSE and analytic continuation of the eigenvalue curve. Right: results from the inhomogeneous BSE.

2.3. Results

2.3.1. Result for the ρ test case

The resonance mass can be calculated from the homogeneous and inhomogeneous BSE, as we have already demonstrated for the σ in the RL truncation in figure 1.4 of section 1.3. We present the results for the ρ-meson calculation for both methods in figure 2.11. They are provided in the same manner as in the free particle case in the example of figure 2.7. In the right-hand sides of both panels in figure 2.11 we show the input region in the $\Gamma > 0$ plane of the first Riemann sheet and on the left the resulting pole position as a circle, where the radius is the standard deviation of the points in the circle. We obtain almost identical results from the homogeneous and inhomogeneous equation. Also, the choice of the input region has a small effect on the result as long as it is above threshold (grey and red boxes). Once we go below threshold, both methods can, at best, estimate the pole position and the error increases significantly. We can conclude that the information above threshold, which can only be accessed with the path deformation we performed, is crucial.

All in all we find a stable result for the ρ. To determine a final value for the calculation we perform 30 runs, each one with a fixed number of input points within the region $M \in [0.5, 0.68]$ GeV and $\Gamma \in [0, 0.1]$ GeV. We do this $N = 10$ times, each time with the method we have described in the last section, and obtain a ρ pole $m_i = M_i - i\Gamma_i/2$ and an error in form of a standard deviation σ_i for $i = 1...10$. We calculate the average m of the $N = 10$ resulting m_i. From m we determine the ρ mass M_ρ and width Γ_ρ from the relation $m = M_\rho - i\Gamma_\rho/2$. The error Δm is given by
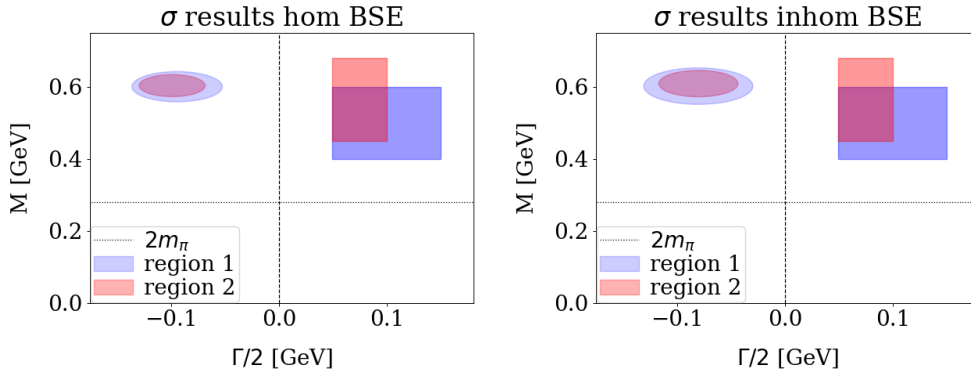
Figure 2.12.: σ meson. Both plots show the $\Gamma < 0$ half plane of the second Riemann sheet on the left and the $\Gamma > 0$ half plane in the first Riemann sheet on the right. Boxes on the right of each plot stand for data calculated from the BSE on the first Riemann sheet for $\Gamma > 0$, circles on the left are the results obtained from analytic continuation to the second Riemann sheet for $\Gamma < 0$. Left: results from the homogeneous BSE. Right: results from the inhomogeneous BSE.

$$\Delta m = \frac{\sqrt{\sum_{i=1}^{N} \sigma_i^2}}{N}, \tag{2.9}$$

where the σ_i stand for the standard deviations of the 10 runs. For the ρ mass and width we finally obtain:

$$M_\rho = 638(2) \text{ MeV}, \qquad \Gamma_\rho = 108(4) \text{ MeV}.$$

Since we calculate the error Δm for the pole position $m = M_\rho - i\Gamma_\rho/2$ the error for Γ_ρ is twice as big as the error for M_ρ.

Our result agrees quite well with the calculation done in [7]. Compared to the experimental values our mass is too small by roughly 130 MeV, the width by roughly 50 MeV, which is quite significant. For further discussions see [7].

2.3.2. Results for the $q\bar{q}$ scalar

The results for the scalar 0^{++} state are calculated with the same method as described in the last section. We explore the stability and the results from the two different methods in figure 2.12. The shaded region on the right shows the selected region where we calculate data from the BSE on the first Riemann sheet. Circles on the left stand for the results in the second sheet obtained from our analytic continuation procedure, where errors are proportional to the radius of the circle. The results are fairly stable considering that the pole is much further out in the complex plane compared to the ρ. Input regions below threshold do not work well though. The final result is again obtained by

2. Beyond RL: ρ and σ as dynamical resonances

			M [MeV]	Γ [MeV]
RL	ρ	[134]	741	104
		This work	736	-
	σ	[134]	670	172
		This work	666	-
BRL	ρ	[7]	640	100
		This work	638(2)	108(4)
	σ	This work	587(12)	186(24)
EXP	ρ	[1]	775	148
	σ		400-550	200-350

Table 2.3.: Results for the ρ and σ masses and width in this work in comparison to previous RL and beyond RL calculations [7, 134], as well as experiment [1].

performing 30 runs, each one with a fixed number of input points within the region $M \in [0.45, 0.68]$ GeV and $\Gamma \in [0.1, 0.2]$ GeV. We do this 10 times and obtain a σ mass and an error in form of a standard deviation each time. We take the average of the ten resulting σ masses and calculate the final error with the standard deviations of the 10 results as an input via equation (2.9). We obtain:

$$M_\sigma = 587(12) \text{ MeV}, \qquad \Gamma_\sigma = 186(24) \text{ MeV}.$$

For comparison, all results (including RL and experimental data) are gathered in table 2.3.

We see that the scalar naturally comes out broader than the vector state in our approach, which might be due to the larger flavor factor in front of the decay diagram in equation (2.3). Let us compare the RL and beyond RL calculations. We find a decrease of the RL mass if we include the ππ decay diagram in the order of $10 - 15\%$ for the ρ and σ states. In absolute terms, the RL masses decrease by roughly 120 and 130 MeV in the σ and ρ case, respectively. Also, a width that is about 15% of the RL mass in the ρ case and about 30% of the RL mass in the σ case, is acquired.

We compare our results against the calculations from ππ scattering in RL from [134] in table 2.3. As expected, the masses are (almost) identical to our RL results. Furthermore, a width was calculated in [134] in a "static" way, that we can compare to our beyond RL results. We could alternatively have compared to the RL calculations of [133], where the "static" widths were obtained from triangle diagrams. In the static case the widths are related to the residues of the ρ and σ pole, respectively. Although in our calculation it is obtained from

the pole location rather than the residue at the pole, we can see that the widths compare quite well. The differences of the RL and beyond RL widths are less then 10 MeV for ρ and σ. This might be an indication that the decay term we introduced in the scattering kernel does not influence the residue by much, but just shifts the pole position out into the complex plane and lowers the resulting resonance mass.

In comparison to experiment we find a σ mass at the upper limit and a width at the lower limit of the PDG value. The result for the mass seems to improve compared to the 666 MeV in RL if the decay term is included. However, the lowering of the mass also appears in the ρ case, which is definitely not an improvement, since the ρ mass is already too low in RL. Considering that the $q\bar{q}$ scalars obtain significantly higher masses from other beyond RL corrections and much hints towards an interpretation of the first excited scalar multiplet as the $q\bar{q}$ states, it seems that the $\pi\pi$ term we included might take a step into the wrong direction and will have to be combined with other beyond RL corrections to obtain a more realistic description of the masses of light mesons. In contrast, the width of both the $f_0(500)$ and its excited partner $f_0(1370)$ are both higher then the width we have calculated. Our width could however be increased by adding more decay channels in future calculations.

2.4. Summary and outlook

The main motivation of this chapter was to explore the method from [7], extend it to the scalar $q\bar{q}$ states and make a future treatment of similar tetraquark systems possible.

We reached the former and calculated the lowest lying scalar $q\bar{q}$ state for the first time in the BSE-DSE approach with a built in decay channel. Because of the decay channel, we made the state resonant and thereby overcame a major problem of the RL $q\bar{q}$ sector. To extract the pole position in the second Riemann sheet, we successfully implemented a path deformation and analytic continuation. For the latter, we made some necessary improvements to the Schlessinger point method. Therefore, despite the larger width of the σ compared to the ρ, we could determine its pole position in the compolex plane and found a relatively stable result with the improved method, also when comparing the two different methods of calculating the resonance mass: homogeneous and inhomogeneous BSE.

We finally confirmed previous results for the ρ and found the mass of the putative σ to be between the experimentally observed states in that channel. Its width, however, is in line with similar static calculations in the rainbow-ladder approximation. We showed how to included the two-pion decay channel into the BSE scattering kernel for ρ and σ in a consistent way. This could in the future be done for other mesons as well.

Also, an application to tetraquarks should be straightforward. In particular the tetraquark two-body approximation, that was solved in [84], but also to the four-body equation of chapter 1 are similar in structure to the equations we have solved in this chapter.

Summary & outlook

Summary

In this thesis we have addressed two main physics topics: The internal structure and properties of heavy-light tetraquarks and the properties of the $I(J^{PC}) = 0(0^{++})$ $q\bar{q}$ scalar with special focus on its description as a resonance.

Heavy-light tetraquarks Concerning heavy-light tetraquarks we calculated:

- the masses of the $I(J^{PC}) = 0(0^{++})$, $0(1^{++})$ and $1(1^{+-})$ $cq\bar{q}\bar{c}$ states and their $I = 0$ $cs\bar{s}\bar{c}$ partners. We identified the $0(1^{++})$ $cq\bar{q}\bar{c}$ and $cs\bar{s}\bar{c}$ states with the $X(3872)$ and the $X(4140)$, respectively. Furthermore, we identified the $1(1^{+-})$ $cq\bar{q}\bar{c}$ tetraquark with the $Z(3900)$.

- the masses of the $I(J^P) = 1(0^+)$, $0(1^+)$ and $1(1^+)$ $cc\bar{q}\bar{q}$ tetraquarks and their $I = 0$ $cc\bar{s}\bar{s}$ partners.

We achieved this by solving a genuine four-body Bethe-Salpeter equation (BSE). Due to a new expansion scheme for the tetraquark amplitude we could identify the impact of different four-quark components on the tetraquark mass. The possible components are:

- $(c\bar{c})(q\bar{q})$: charmonium coupled to a light meson. We will call this "hadro-charmonium" (HC).

- $(c\bar{q})(q\bar{c})$: a heavy-light meson coupled to a heavy-light antimeson. We will call this "heavy-light meson meson" (HLM).

- $(cq)(\bar{q}\bar{c})$. a heavy-light diquark coupled to a heavy-light antidiquark. We will call this "diquark-antidiquark" (DI).

For the $cc\bar{q}\bar{q}$ tetraquark, a HC component is not possible and the diquark-antidiquark component contains a heavy diquark and a light antidiquark: $(cc)(\bar{q}\bar{q})$.

We found that the impact of the different components on the tetraquark mass varied from channel to channel. For the hidden-charm tetraquarks we found a strong HLM and a negligible DI component in all channels. The results are:

- $0(0^{++})$: The scalar state is the lightest hidden-charm tetraquark of the ones we have investigated. It contains a dominant HLM component and is too light to be identified with the $X(3915)$.

- $0(1^{++})$: The putative $X(3872)$ (with quark content $cq\bar{q}\bar{c}$) and $X(4140)$ ($cs\bar{s}\bar{c}$) states have a dominant HLM component.

- $1(1^{+-})$: The putative $Z(3900)$ has a strong HLM and a non-negligible HC component.

For the open-charm tetraquarks we found non-negligible DI components. The results are:

- $1(0^+)$: The scalar is again the lightest state and we need both, HLM and DI components to calculate its mass.

- $0(1^+)$: The state has a strong HLM component and the inclusion of DI terms decreases its mass slightly.

- $1(1^+)$: The state has a strong HLM component and the inclusion of DI terms increases its mass. It is the heaviest $cc\bar{q}\bar{q}$ state of the three we have investigated.

Furthermore, we found a mass gap between the $0(1^+)$ $cc\bar{q}\bar{q}$ and $cc\bar{s}\bar{s}$ of roughly 500 MeV.

Light scalars   We investigated the lowest-lying $q\bar{q}$ state with quantum numbers $I(J^{PC}) = 0(0^{++})$ and calculated its resonance pole for the first time in a beyond rainbow-ladder calculation. We have demonstrated how to consistently introduce a decay channel and how to obtain the resonance pole by solving the resulting BSE. It involves path deformation and analytic continuation to the second Riemann sheet via an improved version of the Schlessinger point method. We call this the BSE-resonance method (**BRM**) in the following.

Outlook

Resonance properties of tetraquarks   We have made some technical progress and came up with a new method to calculate tetraquark properties. There are at present three variations for calculating tetraquarks in the BSE-DSE framework that could be combined with the BRM method, each with their own advantages:

- **4BE**: The most fundamental method is the direct solution of the tetraquark four-body equation (1.31). The drawbacks are the unknown pole positions of the intermediate two-body poles, that are dynamically generated during the solution process.

- **2BE**: The approximated two-body equation was solved in [84]. Advantages are the simpler equation, the known pole positions of the intermediate two-body states and the possibility to determine the importance of physical components, as we did in this thesis. A drawback is the necessity of off-shell meson amplitudes.

- **pole-assisted 4BE** The third method is the "physical" construction of the amplitude and solution of the four-body equation, which we have developed in this thesis. The known pole positions of the intermediate two-body states and the simpler tetraquark amplitudes while still solving the four-body equation are advantageous. Furthermore, one can identify physical components in the amplitude. A drawback is that the error of the further approximations we introduced in comparison to the 4BE method is not quantifiable.

- **kernel-free 4BE** There is also a fourth method, which has not been applied yet. The idea is to eliminate the scattering kernels in the four-body equation by introducing T-matrices, see appendix B.2 for details. This approach avoids the problem of dynamically generated poles if the T-matrices are expanded in two-body poles. The complexity of this coupled set of equations is its main disadvantage.

Extracting resonance properties with the BRM is possible right now for tetraquarks in combination with the 2BE method and first tests have been conducted.

Also, a clear path exists in combination with the pole-assisted 4BE method. The singularity structure of the tetraquark amplitude can be analysed and a suitable path deformation for unequal mass particles can be found in analogy to [8]. The equations however are slightly different in their structure compared to the $q\bar{q}$ equations we analyzed in chapter 2. As a consequence, one will need to solve for the tetraquark amplitude for complex relative momenta.

The BRM method in combination with beyond RL two-body BSEs, as well as the methods for tetraquarks we pointed out above, open up a path to further investigate interesting physics:

Light $q\bar{q}$ and $qq\bar{q}\bar{q}$ scalars In terms of the light $q\bar{q}$ scalar states a possibility is to combine other beyond-RL corrections with a built in decay channel and a solution via the BRM. As discussed we expect a larger scalar $q\bar{q}$ ground state mass, probably above 1 GeV with more elaborate beyond-RL corrections. We naively expect a similar mechanism that pushes the mass down a bit while acquiring a width if a two-pion decay and other beyond-RL corrections are combined. If again the width is in the order of 30% of the mass of the calculation without decay channel, we might end up with a width of roughly 300 MeV. In that case, much speaks for the proposed identification of the $q\bar{q}$ scalar with the first "excited" σ, the $f_0(1370)$, which is also a very broad state (200-500 MeV). This assignment would leave the lowest multiplet for the tetraquark states.

In this context one could look at other multiplet members and other quantum numbers. It would further be an interesting application to investigate the large-N_c behavior for the ρ and σ mesons in analogy to [124]. This would be a good crosscheck but could also be used as a guideline for improvements in the Maris-Tandy model if the large-N_c scaling was found to be different.

The lightest scalar multiplet could be reanalysed with the 2BE and pole-assisted 4BE methods in combination with the BRM. We would expect a similarly light $qq\bar{q}\bar{q}$ component around 400 MeV as was found in [3, 84] for the σ and one could make a statement about the width as well.

In an extension one could couple $q\bar{q}$ and $qq\bar{q}\bar{q}$ components and describe mixing dynamically. This has been attempted in various works for the σ, see [123] and references therein.

Heavy-light tetraquarks There are several interesting future directions in this area.

Summary & outlook

Firstly, the combination of the 2BE and pole-assisted (and possibly the kernel-free 4BE) method with the BRM allows us to investigate the widths' of the tetraquark states, which will be interesting for the $cq\bar{q}\bar{c}$ tetraquarks in particular. As we have discussed in section 1.1, the narrow width seems to be a defining characteristic of many exotic states, especially the $X(3872)$.

The open charm tetraquarks have very different decay channels and it is an open question whether their widths will be comparable to the hidden-charm tetraquarks or quite different. In this context an analysis of which decay channels will create which percentage of the width is of great interest. Especially since many open charm states seem to decay into hadro-charmonium components only it will be interesting whether there is a mechanism that suppresses HLM decays built into our equations, or if the HLM components dominate the decay width as they dominate the mass in many of our calculations.

Secondly, an extended analysis of other quantum numbers, especially in the vector channel would prove valuable. Despite the deficiencies of the $q\bar{q}$ RL axialvector, which would necessarily appear as an intermediate bound state pole, it will be interesting whether the Y states can be interpreted as four-quark states in our approach. This would make a direct comparison with the predictions of the HC model discussed in section 1.1 possible. From what we have learned so far, we would expect a strong HLM component in this channel as well, but there might also be a mechanism favoring HC.

Last but not least it would be important to check the validity of the pole-assisted 4BE method by comparing results also with the other methods: 4BE, 2BE and possibly the kernel-free 4BE as well. Since we constructed this approach as an approximation to the dynamically emerging tetraquark amplitudes of the 4BE method, only further investigations of those systems can provide confidence that the mechanisms we assumed indeed apply.

Other tetraquarks   It is straightforward to extend the pole-assisted 4BE method to similar systems, where the charm quarks are replaced by strange or light quarks. Although this will describe different physics, namely states in the light meson sector, it would be interesting to see whether one obtains light tetraquarks as well in other channels than the scalar one.

Another straightforward extension are the heavy-heavy tetraquarks, especially the $cc\bar{c}\bar{c}$ states. These states are characterized by Pauli and charge-conjugation symmetry. This distinguishes the structure of its wave function from the $cc\bar{q}\bar{q}$ and $cq\bar{q}\bar{c}$ tetraqurks, that only obey the Pauli principle and charge-conjugation, respectively and it would be interesting to see how the results compare.

In summary, we have extended the arsenal of describing tetraquarks in the BSE-DSE framework with the pole-assisted 4BE method and put forward the BRM that allows future studies to extract resonance properties of mesons and tetraquarks. In particular, the foundation has been laid for further studies in the light-light, heavy-heavy as well as the heavy-light tetraquark sectors.

Appendices

A. Utilities

In this appendix we collect a couple of useful definitions and further explanations in terms of numerics. Euclidean gamma matrices and integral definitions are provided in section A.1, details on quadrature and the method for solving homogeneous BSEs that we need in sections 1.3 and 1.4.4 but also throughout chapter 2, are described in section A.2.

A.1. Euclidean integrals and γ-matrices

Four integrals in spherical coordinates are given by:

$$\int_q = \frac{1}{(2\pi)^4} \int d^4q = \frac{1}{(2\pi)^4} \int_0^\infty dq^2 \frac{q^2}{2} \int_{-1}^1 dz\sqrt{1-z^2} \int_{-1}^1 dy \int_0^{2\pi} d\phi. \quad \text{(A.1)}$$

In the DSE and BSE a cutoff is applied to the integrals:

$$\int_q^\Lambda = \frac{1}{(2\pi)^4} \int_0^{\Lambda^2} dq^2 \frac{q^2}{2} \int_{-1}^1 dz\sqrt{1-z^2} \int_{-1}^1 dy \int_0^{2\pi} d\phi. \quad \text{(A.2)}$$

The Euclidean γ-matrices are:

$$\gamma^j = \begin{pmatrix} 0 & -i\sigma^k \\ i\sigma^k & 0 \end{pmatrix} \qquad \gamma^4 = \begin{pmatrix} \mathbb{1} & 0 \\ 0 & -\mathbb{1} \end{pmatrix}, \qquad \gamma^5 = \begin{pmatrix} 0 & \mathbb{1} \\ \mathbb{1} & 0 \end{pmatrix}, \quad \text{(A.3)}$$

where σ^k are the Pauli matrices. Further:

$$C = \gamma_4\gamma_2, \quad \text{(A.4)}$$

where C is the charge conjugation matrix.

A.2. Numerics

A.2.1. Gauss quadrature

The relation

$$\int_a^b dx W(x) f(x) = \sum_{j=0}^{N-1} w_j f(x_j) \quad \text{(A.5)}$$

is exact if $f(x)$ is a polynomial. The x_j are the roots of the orthogonal polynomial p_N:

$$p_N(x_j) = 0$$

and w_j the corresponding weights. The weights for the weight functions:

$$\int_{-1}^{1} dx \ (1-x)^{\alpha}(1+x)^{\beta} f(x) = \sum_{j=0}^{N-1} w_j f(x_j) \qquad (A.6)$$

are called Gauss Jacobi and include: Gauss Tschebychev ($\alpha = \beta = -1/2$) and Gauss Legendre ($\alpha = \beta = 0$). For the former abscissas and weights are given by:

$$x_j = \cos\left(\frac{\pi(j+1/2)}{N}\right), \qquad w_j = \frac{\pi}{N}.$$

A.2.2. Nystrom method

To transform an integral equation

$$f(x) = \int K(x,y)f(y)dy + \underbrace{g(x)}_{=0}$$

into an eigenvalue problem one can apply quadrature (first row) and evaluate the function on the same points y_i as the internal $f(y_i)$, namely the zeroes of the interpolating polynomial:

$$f(x) = \sum_i K(x, y_i)w_i f(y_i),$$

$$f(x_j) = \sum_i K(x_j, y_i)w_i f(y_i).$$

Then one can absorb the weights into the kernel and arrive at an eigenvalue equation with unit eigenvalue:

$$f_j \lambda = \sum_i K_{ji} f_i, \qquad \lambda = 1.$$

For details see [102].

B. Tetraquark

In this part of the appendix we provide further details on the tetraquark amplitude in the "physical" construction from section 1.4.3 in section B.1.1. Furthermore, we provide explicit color traces in section B.1.2 and useful relations for Firz transformations in section B.1.4. Both are important during the solution process of the four-body equation, which is described in section 1.4.4. Further references for details on the L-S decomposition for tetraquarks, which we have presented in section 1.4.2, are provided in section B.1.3. Section B.1.6 lists the errors from the momentum partitioning for all tetraquark states. In section B.2 we show a sketch of the "kernel-free" method for solving the four-body equation.

B.1. Tetraquark amplitude

B.1.1. Physical amplitudes

We provide in table B.2 the explicit expressions for the "physical" tetraquark amplitudes that we gathered in a more compact notation in table 1.9. The shorthands we used are listed in table B.1. We do not write the pole that hides in each tensor structure explicitly, but it can easily be recaptured. For example:

$$\phi_5 = \Phi_5 P_{12,34}(m_S^{cq}, m_S^{cq}),$$
$$\tilde{\phi}_5 = \Phi_5 P_{12,34}(m_S^{cc}, m_S^{qq}),$$

or:

$$\Psi_3 = \psi_3 P_{14,23}(m_v^{c\bar{c}}, m_v^{q\bar{q}}),$$
$$\tilde{\Psi}_3 = \psi_3 P_{14,23}(m_v^{c\bar{q}}, m_v^{q\bar{c}}).$$

The masses are given in table 1.6.

Color, flavor and Dirac tensors are given in equations (1.44), (1.55) and (B.1). We construct the state by writing down all possible components (in all channels) that were gathered in table 1.8 and preserve the relevant symmetries. For an example see section 1.4.3.

B.1.2. Color kernels

The relevant color kernels for this work are

$$K_D = \begin{pmatrix} -\frac{1}{6} & \frac{1}{2} \\ \frac{1}{2} & -\frac{1}{6} \end{pmatrix}, \qquad K_{M_1} = \begin{pmatrix} \frac{4}{3} & \frac{1}{2} \\ 0 & -\frac{1}{6} \end{pmatrix}, \qquad K_{M_2} = \begin{pmatrix} -\frac{1}{6} & 0 \\ \frac{1}{2} & \frac{4}{3} \end{pmatrix}.$$

(B.1)

Here K_D, K_{M_1}, K_{M_2} are the kernels in the diquark, meson one and meson two decomposition evaluated in the $(\mathcal{C}_{11}, \mathcal{C}'_{11})$ basis, for example $(K_D)_{12} =$

B. Tetraquark

	0^+			1^+
ps-ps	$\Phi_1 = \gamma^5_{\alpha\gamma}\gamma^5_{\beta\delta}$		ps - v	$\psi_1^{\pm} = \left(\gamma^5_{\alpha\gamma}\gamma^{\mu}_{\beta\delta} \pm \gamma^{\mu}_{\alpha\gamma}\gamma^5_{\beta\delta}\right)\mathcal{C}_{11}$
	$\Phi_2 = \gamma^5_{\alpha\delta}\gamma^5_{\beta\gamma}$			$\psi_2^{\pm} = \left(\gamma^5_{\alpha\delta}\gamma^{\mu}_{\beta\gamma} \pm \gamma^{\mu}_{\alpha\delta}\gamma^5_{\beta\gamma}\right)\mathcal{C}_{11'}$
v-v	$\Phi_3 = \gamma^{\mu}_{\alpha\gamma}\gamma^{\mu}_{\beta\delta}$		v - v	$\psi_3 = \left(\gamma^{\rho}_{\alpha\gamma}\gamma^{\sigma}_{\beta\delta}\hat{P}^{\nu}\epsilon^{\mu\nu\rho\sigma}\right)\mathcal{C}_{11}$
	$\Phi_4 = \gamma^{\mu}_{\alpha\delta}\gamma^{\mu}_{\beta\gamma}$			$\psi_4 = \left(\gamma^{\rho}_{\alpha\delta}\gamma^{\sigma}_{\beta\gamma}\hat{P}^{\nu}\epsilon^{\mu\nu\rho\sigma}\right)\mathcal{C}_{11'}$
SS	$\Phi_5 = (\gamma^5 C)_{\alpha\beta}(C^T\gamma^5)_{\gamma\delta}\mathcal{C}_{\bar{3}\bar{3}}$		SA	$\psi_5 = (\gamma^5 C)_{\alpha\beta}(C^T\gamma^{\mu})_{\gamma\delta}\mathcal{C}_{\bar{3}\bar{3}}$
AA	$\Phi_6 = (\gamma^{\mu} C)_{\alpha\beta}(C^T\gamma^{\mu})_{\gamma\delta}\mathcal{C}_{\bar{3}\bar{3}}$		AS	$\psi_6 = (\gamma^{\mu} C)_{\alpha\beta}(C^T\gamma^5)_{\gamma\delta}\mathcal{C}_{\bar{3}\bar{3}}$
			AA	$\psi_7 = (\gamma^{\rho})_{\alpha\beta}(C^T\gamma^{\sigma})_{\gamma\delta}\hat{P}^{\nu}\epsilon^{\mu\nu\rho\sigma}\mathcal{C}_{\bar{3}\bar{3}}$

Table B.1.: Tetraquark tensor structures for scalar and axialvector by coupling of mesons and diquarks.

J^{PC}	$\Gamma^{(\mu)}$
$0/1(0^{++})$	$\left[\sum_i \phi_i f_i\right]\mathcal{F}_{0/1}$
$0/1(1^{++})$	$\left[\Psi_1^- f_1 + \Psi_4 f_2 + (\Psi_5 - \Psi_6)f_3\right]\mathcal{F}_{0/1}$
$0/1(1^{+-})$	$\left[\begin{array}{c}\Psi_1^+ f_1 + (\Psi_2^+ + \Psi_2^-)f_2 + (\Psi_2^+ - \Psi_2^-)f_3 + \\ \Psi_3 f_4 + (\Psi_5 + \Psi_6)f_5 + \Psi_7 f_6\end{array}\right]\mathcal{F}_{0/1}$
$0(1^{+})$	$\left[(\tilde{\Psi}_1^- + \tilde{\Psi}_2^-)f_1 + (\tilde{\Psi}_3 + \tilde{\Psi}_4)f_2 + \tilde{\Psi}_6 f_3\right]\tilde{\mathcal{F}}_0$
$1(1^{+})$	$\left[(\tilde{\Psi}_1^+ - \tilde{\Psi}_2^+)f_1 + \tilde{\Psi}_7 f_2\right]\tilde{\mathcal{F}}_1$
$1(0^{+})$	$\left[(\tilde{\phi}_1 - \tilde{\phi}_2)f_1 + (\tilde{\phi}_3 - \tilde{\phi}_4)f_2 + \tilde{\phi}_6 f_3\right]\tilde{\mathcal{F}}_1$

Table B.2.: Explicit physical tetraquark amplitudes. Shorthands are explained in table B.1.

$\mathrm{Tr}(\mathcal{C}_{11}K_{12}\mathcal{C}'_{11}) = \mathrm{Tr}(\mathcal{C}_{11}K_{34}\mathcal{C}'_{11})$. The K_{ij} stand for the color part of the kernels of equation (1.33). In combination with the Fierz relations of (1.44) every color trace can be written as a combination of the ones stated above.

B.1.3. Dirac basis and L-S decomposition

The $L - S$ decompositions for the scalar tetraquarks are provided in great detail in [109] and in more compact notation in [3]. The axialvector $L - S$ decomposition is given in the appendix of [5].

B.1.4. Fierz transformations

In this work we use Fierz transformations mainly to simplify matrix elements. The following lines, however, are kept general, as long as the basis τ has orthonormal projectors P with respect to the scalar product: $\langle|\rangle$. We suppress the range of the indices, in the scalar case with s waves the range is 1...16, whereas it is 1...48 for the axialvector case. A basis element τ_i^d in the basis d can be expressed in another basis $\tau_j^{d\prime}$ as:

$$\tau_i^d = \sum_j T_{dd\prime,ij}\tau_j^{d\prime}, \quad T_{dd\prime,ij} = \langle P_j^{d\prime}|\tau_i^d\rangle$$

$$P_i^d = \sum_j \hat{T}_{dd\prime,ij}P_j^{d\prime}, \quad \hat{T}_{dd\prime,ij} = \langle P_i^d|\tau_j^{d\prime}\rangle = T_{d\prime d,ji}. \tag{B.2}$$

We are interested in the transformation of amplitudes of the form:

$$\Psi^d = \sum_i f_i^d \tau_i^d = \sum_j \sum_i f_i^d T_{dd\prime,ij}\tau_j^{d\prime} = \sum_j f_j^{d\prime}\tau_j^{d\prime}$$

$$f_j^{d\prime} = \sum_i T_{dd\prime,ij} f_i^d$$

and transformations of matrix elements of the form:

$$\langle P_i^d|K|\tau_j^d\rangle f_j^d = \sum_{i\prime,j\prime} \hat{T}_{dd\prime,ii\prime}\langle P_{i\prime}^{d\prime}|K|\tau_{j\prime}^{d\prime}\rangle \sum_j T_{dd\prime,jj\prime} f_j^d$$

$$= \sum_{i\prime} \hat{T}_{dd\prime,ii\prime} \sum_{j\prime}\langle P_{i\prime}^{d\prime}|K|\tau_{j\prime}^{d\prime}\rangle f_{j\prime}^{d\prime}$$

$$= \sum_{i\prime} T_{d\prime d,i\prime i} f_{i\prime}^{K,d\prime}$$

$$= f_i^{K,d},$$

where K is a generic kernel. The last lines are useful: We can calculate the kernel in its home basis $d\prime$ and transform back to d with T. In our case the T's are momentum independent and therefore one can always calculate the complicated loop integrals in the most suitable basis and transform back after the integration is done.
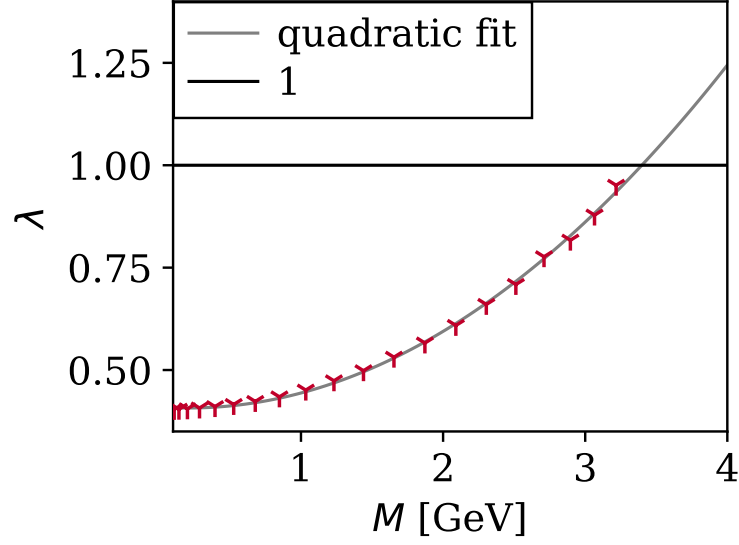
Figure B.1.: Example eigenvalue curve from the $0(0^{++})$ tetraquark calculation.

B.1.5. Fitting the eigenvalue curves

We perform a quadratic fit in $\lambda(M)$ for all results presented in this thesis from chapter 1, if the eigenvalue one is unaccessible. An example is shown in figure B.1.

B.1.6. Error tables

The results for the errors of all tetraquark calculations are shown in table B.3.

m_q [MeV]	3.7	20	50	85	210	340	470	600	730	795
$\frac{\Delta M}{M}$ [%]	5.6	4.7	3.7	2.9	1.7	0.1	0.4	0.3	0.01	0.02
$\frac{\Delta M}{M}$ [%]	11.7	8.9	8.8	5.5	4.4	3.5	0.9	0.5	0.1	0.08
m_q [MeV]	3.7	20	50	85	210	340	470	600	730	795
$\frac{\Delta M}{M}$ [%]	3.8	4.5	2.8	2.2	1.4	0.9	0.4	2.6	0.2	0.1
$\frac{\Delta M}{M}$ [%]	5.3	9.6	14.2	4.4	8.4	1.6	0.4	4.5	3.4	0.8
m_q [MeV]	3.7	20	50	85	210	340	470	600	730	795
$\frac{\Delta M}{M}$ [%]	4.2	4.1	3.1	3.1	2.6	1.6	2.1	2.8	1.0	0.4
$\frac{\Delta M}{M}$ [%]	8.2	8.1	6.8	7.2	4.0	2.9	2.2	2.5	1.0	0.6

Table B.3.: Error estimates from the momentum partitioning for one parameter ζ (row 1) and without restricting the σ_i (row 2). We show the results for the 0^{++}, 1^{+-}, $1(1^+)$ from top to bottom. The results for the 1^{++} state, can be found in table 1.10 in the main text.

B.2. The "kernel-free" four-body BSE

There is another method for tackling the four-body BSE. The idea is to eliminate the scattering kernels in the four-body equation with the exact relation 1.16. This comes at the cost of introducing the two-body T-matrix connecting a quark and an (anti) quark T_{ij}:

$$\bar{\Psi}_{12} = T_{12}(\bar{\Psi}_{13} + \bar{\Psi}_{24} + \bar{\Psi}_{1324} + \bar{\Psi}_{14} + \bar{\Psi}_{23} + \bar{\Psi}_{1423}),$$
$$\bar{\Psi}_{34} = T_{34}(\bar{\Psi}_{13} + \bar{\Psi}_{24} + \bar{\Psi}_{1324} + \bar{\Psi}_{14} + \bar{\Psi}_{23} + \bar{\Psi}_{1423}),$$
$$\bar{\Psi}_{1234} = T_{34}T_{12}(\bar{\Psi}_{13} + \bar{\Psi}_{24} + \bar{\Psi}_{1324} + \bar{\Psi}_{14} + \bar{\Psi}_{23} + \bar{\Psi}_{1423}),$$

$$\bar{\Psi}_{13} = T_{13}(\bar{\Psi}_{12} + \bar{\Psi}_{34} + \bar{\Psi}_{1234} + \bar{\Psi}_{14} + \bar{\Psi}_{23} + \bar{\Psi}_{1423}),$$
$$...,$$

where we have used the shorthands

$$\bar{\Psi}_{12} = (K_{12} - K_{12}K_{34})\Psi, \qquad \bar{\Psi}_{1234} = K_{12}K_{34}\Psi.$$

K_{ij} stand for the two-body kernels in equation (1.25), Ψ for the tetraquark amplitude.

C. Beyond RL ρ and σ

C.1. T-matrix and π-amplitude

The amplitude for the relevant $q\bar{q}$ mesons are given by:

$$\Gamma^\rho = \tau_i^\mu(q,P)f_i(q^2,z) \otimes \mathbb{1} \otimes \sigma = \Gamma_i^\mu f_i(q^2,z),$$
$$\Gamma^\sigma = \tau_i(q,P)f_i(q^2,z) \otimes \mathbb{1} \otimes \mathbb{1} = \Gamma_i f_i(q^2,z),$$

where σ are the Pauli matrices. We construct projectors $P_i^{(\mu)}(q,P) = \hat{\bar{\Gamma}}_i(q,P)$ where the hat denotes normalization such that

$$\text{Tr}(P_i^{(\mu)}(p,P)\Gamma_j^{(\mu)}(p,P)) = \delta_{ij}$$

and the charge conjugation is defined as:

$$\overline{\Gamma}_j(p,P) = (C\tau_i^\mu(-q,P)C^T)^T \otimes \delta^{AB} \otimes (\sigma)^\dagger. \tag{C.1}$$

The equation for the decay diagram includes the T-matrix which is given by:

$$T(q,k,P) = \frac{\overline{\Gamma}_l^\pi(q,-P) \otimes \Gamma_l^\pi(k,P)}{P^2 + m_\pi^2} + R,$$

with $\Gamma_l^\pi = \tau_i(q,P)f_i(q^2,z) \otimes \delta^{AB} \otimes \sigma_l$. With the approximation for the off-shell pion amplitude:

$$\Gamma^\pi = \delta_{AB} \otimes (iE\gamma_5 + ...) \otimes \sigma_j \approx \delta_{AB} \otimes i\frac{B}{f_\pi}\gamma_5 \otimes \sigma_j,$$

where $f_\pi = 92.4$ MeV. Projecting now onto the dressing functions with $\langle P_i|\Gamma\rangle = f_i$, we can evaluate the flavor and color factors for the decay diagram:

$$RL: \ Tr[\mathbb{1}\lambda^a\mathbb{1}\lambda^a]\frac{1}{12} = \frac{4}{3},$$
$$\rho: \ Tr[\sigma_3\sigma_3]\frac{1}{2} = 1,$$
$$\sigma: \ Tr[\mathbb{1}\mathbb{1}]\frac{1}{2} = 1$$

and

$$RL: \ Tr[\mathbb{1}]\frac{1}{3}Tr[\mathbb{1}] = 3,$$
$$\rho: \sum_{s,l} Tr[\frac{\sigma_3}{2}\sigma_l\sigma_s]Tr[\sigma_3\sigma_s\sigma_l] = 4,$$
$$\sigma: \sum_{s,l} Tr[\frac{\mathbb{1}}{2}\sigma_l\sigma_s]Tr[\mathbb{1}\sigma_s\sigma_l] = 6.$$

They are collected in 2.2.

Bibliography

[1] M. Tanabashi, et al. *Phys. Rev.*, **D98**(3):030001 (2018)

[2] R. L. Jaffe. *Phys. Rev.*, **D15**:267 (1977)

[3] G. Eichmann, C. S. Fischer, W. Heupel. *Phys. Lett.*, **B753**:282–287 (2016)

[4] F.-K. Guo, C. Hanhart, U.-G. Meißner, Q. Wang, Q. Zhao, B.-S. Zou. *Rev. Mod. Phys.*, **90**(1) (2018)

[5] P. C. Wallbott, G. Eichmann, C. S. Fischer. *Phys. Rev.*, **D100**(1):014033 (2019)

[6] P. C. Wallbott, G. Eichmann, C. S. Fischer. In preparation

[7] R. Williams. *Phys. Lett.*, **B798**:134943 (2019)

[8] G. Eichmann, P. Duarte, M. T. Peña, A. Stadler (2019)

[9] E. Eichten, K. Gottfried, T. Kinoshita, K. D. Lane, T.-M. Yan. *Phys. Rev.*, **D17**:3090 (1978)

[10] E. Eichten, K. Gottfried, T. Kinoshita, K. D. Lane, T.-M. Yan. *Phys. Rev.*, **D21**:203 (1980)

[11] T. Barnes, S. Godfrey, E. S. Swanson. *Phys. Rev.*, **D72**:054026 (2005)

[12] Y. Koma, M. Koma. *Nucl. Phys.*, **B769**:79–107 (2007)

[13] Y. Koma, M. Koma, H. Wittig. *Phys. Rev. Lett.*, **97**:122003 (2006)

[14] J. Dudek, et al. *Eur. Phys. J.*, **A48**:187 (2012)

[15] G. K. C. Cheung, C. E. Thomas, J. J. Dudek, R. G. Edwards. *JHEP*, **11**:033 (2017)

[16] S. K. Choi, et al. *Phys. Rev. Lett.*, **91**:262001 (2003)

[17] D. Acosta, et al. *Phys. Rev. Lett.*, **93**:072001 (2004)

[18] V. M. Abazov, et al. *Phys. Rev. Lett.*, **93**:162002 (2004)

[19] B. Aubert, et al. *Phys. Rev.*, **D71**:071103 (2005)

[20] R. Aaij, et al. *Eur. Phys. J.*, **C72**:1972 (2012)

[21] R. Aaij, et al. *Phys. Rev. Lett.*, **110**:222001 (2013)

[22] A. Ali, J. S. Lange, S. Stone. *Prog. Part. Nucl. Phys.*, **97** (2017)

[23] G. Barucca, et al. *Eur. Phys. J.*, **A55**(3):42 (2019)

[24] T. Aaltonen, et al. *Phys. Rev. Lett.*, **102**:242002 (2009)

Bibliography

[25] E. Prencipe. dfg project 389090153 (2018)

[26] M. Ablikim, et al. *Phys. Rev. Lett.*, **115**(11):112003 (2015)

[27] Z. Q. Liu, et al. *Phys. Rev. Lett.*, **110**:252002 (2013)

[28] A. Esposito, A. Pilloni, A. D. Polosa. *Phys. Rept.*, **668**:1–97 (2016)

[29] R. F. Lebed, R. E. Mitchell, E. S. Swanson. *Prog. Part. Nucl. Phys.*, **93**:143–194 (2017)

[30] H.-X. Chen, W. Chen, X. Liu, S.-L. Zhu. *Phys. Rep.*, **639** (2016)

[31] S. L. Olsen, T. Skwarnicki, D. Zieminska. *Rev. Mod. Phys.*, **90**(1):015003 (2018)

[32] M. B. Voloshin. *Prog. Part. Nucl. Phys.*, **61**:455–511 (2008)

[33] S. Prelovsek. *PoS*, **LATTICE2014**:015 (2014)

[34] M. Luscher. *Commun. Math. Phys.*, **104**:177 (1986)

[35] M. Luscher. *Commun. Math. Phys.*, **105**:153–188 (1986)

[36] S. Prelovsek, L. Leskovec. *Phys. Rev. Lett.*, **111**:192001 (2013)

[37] S. Prelovsek, C. B. Lang, L. Leskovec, D. Mohler. *Phys. Rev.*, **D91**(1):014504 (2015)

[38] S.-h. Lee, C. DeTar, H. Na, D. Mohler (2014)

[39] Y. Ikeda. *J. Phys.*, **G45**(2):024002 (2018)

[40] M. Padmanath, C. B. Lang, S. Prelovsek. *Phys. Rev.*, **D92**(3):034501 (2015)

[41] S. Ozaki, S. Sasaki. *Phys. Rev.*, **D87**(1):014506 (2013)

[42] M. Cleven, F.-K. Guo, C. Hanhart, Q. Wang, Q. Zhao. *Phys. Rev.*, **D92**(1):014005 (2015)

[43] X. Li, M. B. Voloshin. *Mod. Phys. Lett.*, **A29**(12):1450060 (2014)

[44] S. Dubynskiy, M. Voloshin. *Phys. Lett. B*, **666**(4) (2008)

[45] M. Neubert. *Phys. Rept.*, **245**:259–396 (1994)

[46] F. Stancu. *ArXivhep-Ph0607077* (2006)

[47] F. Buccella, H. Høgaasen, J.-M. Richard, P. Sorba. *Eur. Phys. J. C*, **49**(3) (2007)

[48] D. Ebert, R. N. Faustov, V. O. Galkin. *Phys. Lett.*, **B634**:214–219 (2006)

[49] L. Maiani, F. Piccinini, A. D. Polosa, V. Riquer. *Phys. Rev.*, **D71**:014028 (2005)

[50] L. Maiani, F. Piccinini, A. D. Polosa, V. Riquer. *Phys. Rev. D*, **89**(11) (2014)

[51] A. Ali, L. Maiani, A. V. Borisov, I. Ahmed, M. Jamil Aslam, A. Ya. Parkhomenko, A. D. Polosa, A. Rehman. *Eur. Phys. J.*, **C78**(1):29 (2018)

[52] M. Karliner, J. L. Rosner. *Phys. Rev. Lett.*, **119**(20):202001 (2017)

[53] P. Junnarkar, N. Mathur, M. Padmanath. *Phys. Rev.*, **D99**(3):034507 (2019)

[54] E. J. Eichten, C. Quigg. *Phys. Rev. Lett.*, **119**(20):202002 (2017)

[55] A. Francis, R. J. Hudspith, R. Lewis, K. Maltman. *Phys. Rev. Lett.*, **118**(14):142001 (2017)

[56] A. Francis, R. J. Hudspith, R. Lewis, K. Maltman. *Phys. Rev.*, **D99**(5):054505 (2019)

[57] L. Leskovec, S. Meinel, M. Pflaumer, M. Wagner. *Phys. Rev.*, **D100**(1):014503 (2019)

[58] P. Bicudo, M. Cardoso, A. Peters, M. Pflaumer, M. Wagner. *Phys. Rev.*, **D96**(5):054510 (2017)

[59] M.-L. Du, W. Chen, X.-L. Chen, S.-L. Zhu. *Phys. Rev.*, **D87**(1):014003 (2013)

[60] Y. Ikeda, B. Charron, S. Aoki, T. Doi, T. Hatsuda, T. Inoue, N. Ishii, K. Murano, H. Nemura, K. Sasaki. *Phys. Lett.*, **B729**:85–90 (2014)

[61] M. E. Peskin. *An introduction to quantum field theory.* CRC Press (2018)

[62] M. Srednicki. *Quantum field theory.* Cambridge University Press (2007)

[63] T. Göcke. Ph.D. thesis, Giessen U. (2012)

[64] G. Eichmann. Hadron physics lecture (2014). Http://cftp.ist.utl.pt/ gernot.eichmann/2014-hadron-physics/

[65] L. D. Faddeev, V. N. Popov. *Phys. Lett.*, **25B**:29–30 (1967)

[66] J. S. Schwinger. *Proc. Nat. Acad. Sci.*, **37**:452–455 (1951)

[67] F. J. Dyson. *Phys. Rev.*, **75**:1736–1755 (1949)

[68] R. Alkofer, L. von Smekal. *Phys. Rept.*, **353**:281 (2001)

[69] R. Alkofer, M. Q. Huber, K. Schwenzer. *Comput. Phys. Commun.*, **180**:965–976 (2009)

[70] A. Bashir, L. Chang, I. C. Cloet, B. El-Bennich, Y.-X. Liu, C. D. Roberts, P. C. Tandy. *Commun. Theor. Phys.*, **58**:79–134 (2012)

[71] C. S. Fischer. *J. Phys.*, **G32**:R253–R291 (2006)

[72] P. Maris, C. D. Roberts. *Int. J. Mod. Phys.*, **E12**:297–365 (2003)

[73] C. D. Roberts, A. G. Williams. *Prog. Part. Nucl. Phys.*, **33**:477–575 (1994)

[74] J. Carbonell, V. A. Karmanov. *Phys. Rev.*, **D90**(5):056002 (2014)

[75] E. E. Salpeter, H. A. Bethe. *Phys. Rev.*, **84**:1232–1242 (1951)

[76] C. H. Llewellyn-Smith. *Annals Phys.*, **53**:521–558 (1969)

[77] N. Nakanishi. *Prog. Theor. Phys. Suppl.*, **43**:1–81 (1969)

[78] M. Blank. Ph.D. thesis, Graz U. (2011)

[79] J. M. Cornwall, R. Jackiw, E. Tomboulis. *Phys. Rev.*, **D10**:2428–2445 (1974)

[80] G. Eichmann, H. Sanchis-Alepuz, R. Williams, R. Alkofer, C. S. Fischer. *Prog. Part. Nucl. Phys.*, **91** (2016)

[81] M. Blank, A. Krassnigg. *Comput. Phys. Commun.*, **182**:1391–1401 (2011)

[82] H. Sanchis-Alepuz, R. Williams. *Comput. Phys. Commun.*, **232**:1–21 (2018)

[83] H. Sanchis-Alepuz, C. S. Fischer, C. Kellermann, L. von Smekal. *Phys. Rev. D*, **92**(3) (2015)

[84] W. Heupel, G. Eichmann, C. S. Fischer. *Phys. Lett.*, **B718**:545–549 (2012)

[85] S.-S. Xu, Z.-F. Cui, L. Chang, J. Papavassiliou, C. D. Roberts, H.-S. Zong. *Eur. Phys. J.*, **A55**(7):113 (2019)

[86] P. Maris, P. C. Tandy. *Phys. Rev.*, **C60**:055214 (1999)

[87] P. Maris, C. D. Roberts, P. C. Tandy. *Phys. Lett.*, **B420**:267–273 (1998)

[88] R. Alkofer, W. Detmold, C. S. Fischer, P. Maris. *Phys. Rev.*, **D70**:014014 (2004)

[89] M. Blank, A. Krassnigg. *Phys. Rev.*, **D84**:096014 (2011)

[90] C. S. Fischer, S. Kubrak, R. Williams. *Eur. Phys. J.*, **A51**:10 (2015)

[91] T. Hilger, C. Popovici, M. Gomez-Rocha, A. Krassnigg. *Phys. Rev.*, **D91**(3):034013 (2015)

[92] C. S. Fischer, S. Kubrak, R. Williams. *Eur. Phys. J.*, **A50**:126 (2014)

[93] A. Krassnigg. *Phys. Rev.*, **D80**:114010 (2009)

[94] R. Alkofer, P. Watson, H. Weigel. *Phys. Rev.*, **D65**:094026 (2002)

[95] E. Rojas, B. El-Bennich, J. P. B. C. de Melo. *Phys. Rev.*, **D90**:074025 (2014)

[96] T. Nguyen, N. A. Souchlas, P. C. Tandy. *AIP Conf. Proc.*, **1361**(1):142–151 (2011)

[97] M. Gómez-Rocha, T. Hilger, A. Krassnigg. *Few Body Syst.*, **56**(6-9):475–480 (2015)

[98] S.-x. Qin, L. Chang, Y.-x. Liu, C. D. Roberts, D. J. Wilson. *Phys. Rev.*, **C85**:035202 (2012)

[99] P. Maris. *Few-Body Syst.*, **32**(1-2) (2002)

[100] S. Weinberg. *Phys. Rev.*, **133**:B1318–B1332 (1964)

[101] A. Krassnigg, M. Blank. *Phys. Rev.*, **D83**:096006 (2011)

[102] W. Press, S. Teukolsky, W. Vetterling, B. Flannery. *Numerical Recipes 3rd Edition: The Art of Scientific Computing.* Cambridge University Press (2007)

[103] G. Guennebaud, B. Jacob, et al. Eigen v3. http://eigen.tuxfamily.org (2010)

[104] O. A. Yakubovsky. *Sov. J. Nucl. Phys.*, **5**:937 (1967)

[105] K. Huang, H. A. Weldon. *Phys. Rev.*, **D11**:257 (1975)

[106] A. M. Khvedelidze, A. N. Kvinikhidze. *Theor. Math. Phys.*, **90**:62–74 (1992)

[107] G. Eichmann. *Phys. Rev.*, **D84**:014014 (2011)

[108] G. Eichmann, C. S. Fischer, W. Heupel. *Phys. Rev.*, **D92**(5):056006 (2015)

[109] W. Heupel. Ph.D. thesis, Giessen U. (2015)

[110] V. Shtabovenko, R. Mertig, F. Orellana. *Comput. Phys. Commun.*, **207**:432–444 (2016)

[111] V. Hernandez, J. E. Roman, V. Vidal. *ACM Trans. Math. Software*, **31**(3):351–362 (2005)

[112] S. Bochkanov. Alglib (www.alglib.net)

[113] C. Hanhart, J. R. Pelaez, G. Rios. *Phys. Lett.*, **B739**:375–382 (2014)

[114] J. Bonnet. Ph.D. thesis, Giessen U. (2018)

[115] A. Vinokurova, et al. *JHEP*, **06**:132 (2015)

[116] M. Karliner, J. L. Rosner. *Nucl. Phys.*, **A954**:365–370 (2016)

Bibliography

[117] F. Stancu. *J. Phys.*, **G37**:075017 (2010)

[118] C. Patrignani, et al. *Chin. Phys.*, **C40**(10):100001 (2016)

[119] P. C. Wallbott, G. Eichmann, C. S. Fischer. *J. Phys. Conf. Ser.*, **1024**(1):012035 (2018)

[120] S. M. Roy. *Phys. Lett.*, **36B**:353–356 (1971)

[121] I. Caprini, G. Colangelo, H. Leutwyler. *Phys. Rev. Lett.*, **96**:132001 (2006)

[122] R. Garcia-Martin, R. Kaminski, J. R. Pelaez, J. Ruiz de Elvira. *Phys. Rev. Lett.*, **107**:072001 (2011)

[123] J. R. Pelaez. *Phys. Rept.*, **658**:1 (2016)

[124] J. R. Pelaez. *Mod. Phys. Lett.*, **A19**:2879–2894 (2004)

[125] S. Weinberg. *Phys. Rev. Lett.*, **110**:261601 (2013)

[126] J. Ruiz de Elvira, J. R. Pelaez, M. R. Pennington, D. J. Wilson. *Phys. Rev.*, **D84**:096006 (2011)

[127] D. Parganlija, F. Giacosa, D. H. Rischke. *Phys. Rev.*, **D82**:054024 (2010)

[128] H.-X. Chen, A. Hosaka, S.-L. Zhu. *Phys. Rev.*, **D76**:094025 (2007)

[129] R. Williams, C. S. Fischer, W. Heupel. *Phys. Rev.*, **D93**(3):034026 (2016)

[130] L. Chang, C. D. Roberts. *Phys. Rev. Lett.*, **103**:081601 (2009)

[131] L. Chang, C. D. Roberts. *Phys. Rev.*, **C85**:052201 (2012)

[132] D. Jarecke, P. Maris, P. C. Tandy. *Phys. Rev.*, **C67**:035202 (2003)

[133] V. Mader, G. Eichmann, M. Blank, A. Krassnigg. *Phys. Rev.*, **D84**:034012 (2011)

[134] S. R. Cotanch, P. Maris. *Phys. Rev.*, **D66**:116010 (2002)

[135] R. Oehme. *Physical Review*, **121**(6):1840 (1961)

[136] S. Godfrey, N. Isgur. *Phys. Rev. D*, **32**(1) (1985)

[137] R. Ricken, M. Koll, D. Merten, B. C. Metsch. *Eur. Phys. J.*, **A18**:667–689 (2003)

[138] C. Hanhart, J. R. Pelaez, G. Rios. *Phys. Rev. Lett.*, **100**:152001 (2008)

[139] J. Nebreda, J. R. Pelaez. *Phys. Rev.*, **D81**:054035 (2010)

[140] L. Leskovec, C. Alexandrou, S. Meinel, J. W. Negele, S. Paul, M. Petschlies, A. Pochinsky, G. Rendon, S. Syritsyn. *13th Conference on the Intersections of Particle and Nuclear Physics (CIPANP 2018) Palm Springs, California, USA, May 29-June 3, 2018* (2018)

[141] X. Feng, K. Jansen, D. B. Renner. *Phys. Rev.*, **D83**:094505 (2011)

[142] S. Aoki, et al. *Phys. Rev.*, **D76**:094506 (2007)

[143] M. Gockeler, R. Horsley, Y. Nakamura, D. Pleiter, P. E. L. Rakow, G. Schierholz, J. Zanotti. *PoS*, **LATTICE2008**:136 (2008)

[144] R. A. Briceno, J. J. Dudek, R. G. Edwards, D. J. Wilson. *Phys. Rev. Lett.*, **118**(2):022002 (2017)

[145] R. A. Briceno, J. J. Dudek, R. G. Edwards, D. J. Wilson. *Phys. Rev.*, **D97**(5):054513 (2018)

[146] P. Watson, W. Cassing. *Few Body Syst.*, **35**:99–115 (2004)

[147] C. S. Fischer, D. Nickel, J. Wambach. *Phys. Rev.*, **D76**:094009 (2007)

[148] P. Maris. *Phys. Rev.*, **D52**:6087–6097 (1995)

[149] S. Strauss, C. S. Fischer, C. Kellermann. *Phys. Rev. Lett.*, **109**:252001 (2012)

[150] A. Windisch, M. Q. Huber, R. Alkofer. *Phys. Rev.*, **D87**(6):065005 (2013)

[151] E. Weil, G. Eichmann, C. S. Fischer, R. Williams. *Phys. Rev.*, **D96**(1):014021 (2017)

[152] L. Schlessinger. *Physical Review*, **167**(5):1411 (1968)

[153] H. Vidberg, J. Serene. *Journal of Low Temperature Physics*, **29**(3-4):179–192 (1977)

[154] H. S. Yamada, K. S. Ikeda. *International Journal of Computational Mathematics*, **2014** (2014)

[155] R.-A. Tripolt, P. Gubler, M. Ulybyshev, L. Von Smekal. *Comput. Phys. Commun.*, **237**:129–142 (2019)

[156] R.-A. Tripolt, I. Haritan, J. Wambach, N. Moiseyev. *Phys. Lett.*, **B774**:411–416 (2017)

[157] F. Pedregosa, G. Varoquaux, A. Gramfort, V. Michel, B. Thirion, O. Grisel, M. Blondel, P. Prettenhofer, R. Weiss, V. Dubourg, J. Vanderplas, A. Passos, D. Cournapeau, M. Brucher, M. Perrot, E. Duchesnay. *Journal of Machine Learning Research*, **12**:2825–2830 (2011)

Danksagung

Selbstständigkeitserklärung

Ich erkläre: Ich habe die vorgelegte Dissertation selbstständig und ohne unerlaubte fremde Hilfe und nur mit den Hilfen angefertigt, die ich in der Dissertation angegeben habe. Alle Textstellen, die wörtlich oder sinngemäß aus veröffentlichten Schriften entnommen sind, und alle Angaben, die auf mündlichen Auskünften beruhen, sind als solche kenntlich gemacht. Ich stimme einer evtl. Überprüfung meiner Dissertation durch eine Antiplagiat-Software zu. Bei den von mir durchgeführten und in der Dissertation erwähnten Untersuchungen habe ich die Grundsätze guter wissenschaftlicher Praxis, wie sie in der „Satzung der Justus-Liebig-Universität Gießen zur Sicherung guter wissenschaftlicher Praxis" niedergelegt sind, eingehalten.

_____   _____
Ort, Datum   Unterschrift